2009

Atom-Based Computer Simulation Studies of Gas-to-Liquid Nucleation in Atmospherically Relevant Systems: Clarifying Discrepancies and Elucidating Mechanisms

Ricky Bendanillo Nellas
Louisiana State University and Agricultural and Mechanical College, r_nellas@yahoo.com

ATOM-BASED COMPUTER SIMULATION STUDIES OF GAS-TO-LIQUID NUCLEATION IN ATMOSPHERICALLY RELEVANT SYSTEMS: CLARIFYING DISCREPANCIES AND ELUCIDATING MECHANISMS

A Dissertation

Submitted to the Graduate Faculty of the
Louisiana State University and
Agricultural and Mechanical College
in partial fulfillment of the
requirements for the degree of
Doctor of Philosophy
in
The Department of Chemistry

by
Ricky Bendanillo Nellas
B.S., University of the Philippines – Los Baños, 1999
May 2010

Acknowledgments

I have no clue why I chose computational chemistry for my graduate studies. But I have no regrets, thanks to my boss, Professor Bin Chen. Not only did he pour computational knowledge into my empty head, he let me explore nucleation beyond Earthly conditions. I will always be grateful for his continuous support and inspiration. To Prof. J. Ilja Siepmann, thanks for a great collaboration. I am also indebted to the members of my advisory committee: Prof. Robert Cook, Prof. Barry Dellinger, Prof. Randall Hall, Prof. James Henry, Prof. Julia Chan, and Prof. Manuel Tiglio. Your comments and suggestions mean a lot. I am also grateful to Mr. Imtiaz Hossain, Ms. Shalini Venkataraman, Prof. Daniel Katz, Dr. Brygg Ullmer, Dr. Werner Benger, Prof. Les Butler, and Dr. Heath Barnett for extending their expertise in visualizing my data. I also would like to thank Prof. Barbara Hale for sharing her expertise on nucleation scaling laws during the International Conference on Nucleation and Atmospheric Aerosols (ICNAA) held in Galway, Ireland. Many thanks to my smart group mates: Dr. Matthew McKenzie, Samuel Keasler, and Hyunmi Kim; for being there when I need help.

I am forever beholden to my family: Lolo QN, Papa Modesto, Mama Luming, Auntie Abeth, Uncle Gordon, Nong Freddie, Jen, Inday Marisa, Nong Dante and Remar; for being my source of never ending pride, encouragement, and inspiration. To Ate Ruby and Kuya Marcus Ynalvez, a special thanks for the great friendship. To Ms. Luisa Catan, Ms. Brenda Consing, Dr. Nieva T. Librojo-Basilio, Dr. Eugenia Castillo, Dr. Norriel Nipales and to all my teachers, thanks a lot! To all my colleagues in Holy Cross High School (HCHS) and University of the Philippines – Los Baños (UPLB), it was great to have you in this incredible professional and academic journey. To my Knights of Columbus family, thank you for the great friendship. To all my friends in Baton Rouge, thanks for adding more spice to my already spicy graduate school life.

I will forever be thankful to LSU for giving me the opportunity to do great research and enjoy the purple and gold's way of life. Thanks to the LSU Center for Computation and Technology, the Office of Computing Services at LSU, and the Louisiana Optical Network Initiative for the generous computer resources. Financial support from LSU start-up fund, the National Science Foundation (CHE/MCB-0448918), the Petroleum Research Fund, administered by the American Chemical Society (Grant 41933-G9), Louisiana Board of Regents Support Fund (LEQSF(2005-08)-RD-A-02), and a Council on Research Summer Stipend Award from LSU Office of Research and Graduate Studies is gratefully acknowledged. I am also thankful to the Department of Chemistry, the Graduate School, and the National Science Foundation (NSF) for awarding me the 2007 James G. Traynham Award for Distinguished Graduate Student, two NSF Travel Awards, the Charles E. Coates Travel Award, and 2 Graduate School Travel Awards.

Table of Contents

Acknowledgments ii

List of Tables vii

List of Figures viii

List of Abbreviations and Symbols xii

Abstract xvi

Chapter 1. Introduction 1
1.1 Nucleation and Computer Simulation 1
1.2 The Classical Nucleation Theory and Beyond 5

Chapter 2. The AVUS – HR Approach 10
2.1 Introduction 10
2.2 Nucleation in the Grand Canonical Ensemble 10
2.2.1 Cluster Definition 10
2.2.2 Free Energy of Formation 11
2.2.3 Cluster in the Grand Canonical Ensemble 12
2.3 Metropolis Monte Carlo 13
2.4 Aggregation-Volume-Bias Monte Carlo (AVBMC) 17
2.5 Umbrella Sampling (US) 20
2.6 Histogram Reweighting (HR) 22

Chapter 3. Exploring the Discrepancies between Experiment, Theory, and Simulation for the Homogeneous Gas-to-Liquid Nucleation of 1-Pentanol 24
3.1 Introduction 24
3.2 Simulation Details 25
3.3 Results and Discussions 25
3.4 Concluding Remarks 40

Chapter 4. Probing the Nucleation Mechanism for the Binary *n*-Nonane/1-Alcohol Series with Atomistic Simulations 41
4.1 Introduction 41
4.2 Simulation Details 42
4.2.1 Molecular Models 42
4.2.2 Nucleation Free Energy (NFE) Calculations 42
4.2.3 Determination of Onset Activities 44
4.3 Results and Discussions 45
4.3.1 Nucleation Free Energy (NFE) Contour Maps 45
4.3.2 Plots of the Onset Activities 50

4.3.3 Molecular Content of Nuclei 51
4.3.4 Microscopic Structure of Clusters 54
4.3.5 Further Discussions.....57
4.4 Concluding Remarks.....58

Chapter 5. Ternary Nucleation.....60
5.1 Dumbbells and Onions in Ternary Nucleation 60
5.2 Towards Understanding the Nucleation Mechanism for Multicomponent Systems: An Atomistic Simulation of the Ternary Nucleation of Water/*n*-Nonane/1-Butanol.....65
5.2.1 Introduction.....65
5.2.2 Simulation Details.....66
5.2.3 Results and Discussions.....68
5.2.3.1 The Entire Onset Activity Surface for This Mixture 68
5.2.3.2 Binary Water/1-Butanol-Like Non-Ideal Behavior at Low a_2' 69
5.2.3.3 Binary *n*-Nonane/1-Butanol-Like Behavior Mixed Slightly with Binary Water/1-Butanol-Like Behavior at High a_2'.....72
5.2.3.4 Binary *n*-Nonane/1-Butanol-Like Behavior Mixed Substantially with Binary Water/1-Butanol-Like Behavior at Intermediate a_2'.....77
5.2.3.5 Implications from the Nanophase Diagrams on Tailor – Made Nanoparticles 81
5.2.4 Concluding Remarks.....81
5.3 Molecular Content and Structure of Aqueous Organic Nanodroplets from Vapor-Liquid Nucleation Study of the Water/*n*-Nonane/1-Alcohol Series.....82
5.3.1 Introduction.....82
5.3.2 Simulation Details.....84
5.3.3 Results and Discussions.....85
5.3.3.1 Plots of the Onset Activities 85
5.3.3.2 Core-Shell Structures Formed by the Water/1-Alcohol Clusters and Comparison to the Experimental Data for These Binary Series.....87
5.3.3.3 Enhanced Miscibility between Water and *n*-Nonane Due to the Presence of Alcohols via the Core-Shell Motif.....92
5.3.3.4 Implications of the Core-Shell Structure on Atmospheric Organic Aerosols and Beyond 102
5.3.4 Concluding Remarks.....103

Chapter 6. Where Are the Water Molecules on Mars?.....105

References.....108

Appendix
A. Permission Request / Correspondence to the American Chemical Society.....119

B. License Agreement from the Journal of Physical Chemistry A 124

C. License Agreement from the Journal of Physical Chemistry B.....128

D. Permission Request / Correspondence to the Royal Society of Chemistry 132

E. Permission Letter from the Royal Society of Chemistry 137

Vita 138

List of Tables

3.1 Average hydrogen bond number of 1-pentanol at a specific temperature (235, 280, and 340 K) and cluster size (14, 28, and 46-molecule cluster). Data obtained from additional *NpT* (bulk phase simulation using 500 1-pentanol molecules at various temperatures are also included 37

List of Figures

3.1 $\delta\Delta G(n)$ plotted against the function $n^{2/3} - (n\text{-}1)^{2/3}$ for 29 different temperatures 27

3.2 Magnification of the portion of Figure 5.16 where the linear fits are performed ($15 \leq n \leq 50$) 27

3.3 Natural logarithm of the nucleation rate ratio as a function of inverse temperature obtained at various conditions where the simulation predicted barrier height is 20, 25, 30, 35, and 75 $k_B T$.....29

3.4 Natural logarithm of the nucleation rate ratio between experiment (or simulation) and CNT as a function of inverse temperature 30

3.5 ΔG^* difference between CNT and simulation as a function of temperature.....32

3.6 Comparison between experiment and simulation results for the temperature dependence of the (a) density, (b) surface tension, and (c) $A_1\gamma$ contribution 34

3.7 Log – log plot of *n*-pentanol cluster size versus the reduced radius of gyration at 235 K, 280 K, and 340 K.....36

3.8 Snapshots of clusters containing 14 1-pentanol molecules taken at 235 K, 280 K, and 340 K.....36

3.9 Fraction of molecules in a hydrogen bonded *n*-aggregate at 235 K, 280 K, and 340 K for 14-molecule cluster, 28-molecule cluster, and 46-molecule cluster.....39

4.1 Contour of the two-dimensional NFEs (in units of $k_B T$) as a function of the number of molecules for the two components involved in each binary mixture calculated from the simulation at (a) $n_v^{\text{nonane}} = 1.71 \times 10^{-7}$ Å^{-3} and $n_v^{\text{water}} = 4.36 \times 10^{-8}$ Å^{-3}; and (b) $n_v^{\text{nonane}} = 1.34 \times 10^{-7}$ Å^{-3} and $n_v^{\text{methanol}} = 8.11 \times 10^{-8}$ Å^{-3} 47

4.2 Contour of the two-dimensional NFEs (in units of $k_B T$) as a function of the number of molecules for the two components involved in each binary mixture calculated from the simulation at (a) $n_v^{\text{nonane}} = 1.45 \times 10^{-7}$ Å^{-3} and $n_v^{\text{ethanol}} = 3.83 \times 10^{-8}$ Å^{-3}; (b) $n_v^{\text{nonane}} = 1.58 \times 10^{-7}$ Å^{-3} and $n_v^{\text{1-propanol}} = 1.41 \times 10^{-8}$ Å^{-3}; and (c) $n_v^{\text{nonane}} = 1.45 \times 10^{-7}$ Å^{-3} and $n_v^{\text{1-butanol}} = 5.71 \times 10^{-9}$ Å^{-3}.....47

4.3 Contour of the two-dimensional NFEs (in units of k_BT) as a function of the number of molecules for the two components involved in each binary mixture calculated from the simulation at (a) $n_v^{\text{nonane}} = 1.26 \times 10^{-7}$ Å^{-3} and $n_v^{\text{1-hexanol}} = 6.87 \times 10^{-10}$ Å^{-3}; (b) $n_v^{\text{nonane}} = 1.11 \times 10^{-7}$ Å^{-3} and $n_v^{\text{1-decanol}} = 2.34 \times 10^{-11}$ Å^{-3}; and (h) $n_v^{\text{ethanol}} = 1.61 \times 10^{-8}$ Å^{-3} and $n_v^{\text{water}} = 1.71 \times 10^{-8}$ Å^{-3} 48

4.4 Plots of reduced onset activities 50

4.5 Average mole fraction of *n*-nonane in the critical nuclei as a function of the normalized activity fraction of *n*-nonane 52

4.6 Probability density (expressed as an absolute concentration) of the critical cluster nuclei as a function of $\delta = n_{\text{nonane}} - n_{\text{alcohol}}$ for the nucleation of *n*-nonane/methanol, *n*-nonane/ethanol, *n*-nonane/1-decanol, and *n*-nonane/water at a normalized *n*-nonane activity fraction of 0.5 with a combined nucleation barrier height of 50.64 k_BT 54

4.7 Probability density of the critical cluster and the precritical clusters containing 5, 10, and 15 molecules as a function of $\delta = n_{\text{nonane}} - n_{\text{1-hexanol}}$ for nucleation of the binary *n*-nonane/1-hexanol system at a normalized *n*-nonane activity fraction of 0.5 with a combined nucleation barrier height of 50.64 k_BT 55

4.8 Representative snapshots of clusters (consisting of 20 *n*-nonane and 20 alcohol or water molecules) obtained at T = 230 K for (a) *n*-nonane/water, (b) *n*-nonane/methanol, (c) *n*-nonane/ethanol, (d) *n*-nonane/1-propanol, (e) *n*-nonane/1-butanol, and (f) *n*-nonane/1-hexanol 56

4.9 Radial density profiles for the *n*-nonane/methanol and *n*-nonane/1-hexanol systems averaged over clusters containing a roughly equal number (20 ± 2) of *n*-nonane and 1-alcohol molecules 57

4.10 Distributions of 1-alcohol hydrogen-bonded aggregates with aggregation number *n* for *n*-nonane/methanol and *n*-nonane/1-hexanol found in those clusters near the saddle-point region shown in Figure 4.1 and Figure 4.3, i.e., with an NFE value between 58 and 62 k_BT for *n*-nonane/methanol or between 50 and 54 k_BT for *n*-nonane/1-hexanol 58

5.1 Plot of the reduced onset activities at a_2'= 0.6 62

5.2 The average mole fraction of water, *n*-nonane, and 1-butanol found in the critical nuclei at a_2' = 0.6 as a function of the normalized activity fraction a_3' 63

5.3 Probability density (absolute concentration in units of droplets Å^{-3}) of critical clusters as a function of cluster composition at a_2' = 0.6 and a_3' = 0.14, a condition when all three components contribute significantly to the critical clusters 63

5.4 (A) Snapshot of a "dumbbell" critical cluster consisting of 13 water, 13 oil, and 4 surfactant molecules; (B) Snapshot of an "onion" critical cluster consisting of 10 water, 10 oil, and 10 surfactant molecules 64

5.5 (a) The entire onset activity surface obtained from the simulation at any vapor-phase composition ratios; (b) Comparison of onset activities between the simulation at 230 K and the experiment at 240 K at constant a_2' from 0 to 1 at 0.2 interval by varying the 1-butanol content.....69

5.6 (a) Onset activities and (b) the average mole fraction of water, *n*-nonane, and 1-butanol in the critical nuclei as function of the vapor-phase composition obtained at a_2' values of 0, 0.2, and 0.4.....71

5.7 NFEs (in units of kBT) as function of cluster composition at a_1 = 0.428, a_2' = 0.4, and a_3' = 0.35: (a) a front view of this NFE landscape to illustrate the major nucleation channel along the water / 1-butanol surface; (b) the NFE contour obtained at the saddle point surface or for clusters with the critical cluster size; and (c) a perspective view of the major nucleation channel on the NFE landscape to show how it passes through the saddle point surface.....73

5.8 Representative snapshots of clusters (consisting of 5, 10, 20 and 40 molecules of each component) obtained from the binary nucleation simulation of water/1-butanol.....73

5.9 The average mole fraction of water, *n*-nonane, and 1-butanol in the critical cluster as function of the vapor-phase composition obtained at (a) a_2' = 1.0 and (b) a_2' = 0.8 74

5.10 NFEs (in units of kBT) as function of cluster composition at a_1 = 0.212, a_2' = 0.8, and a_3' = 0.35: (a) A front view of this NFE landscape to illustrate the multi-pathway feature along the *n*-nonane / 1-butanol surface; and (b) the NFE contour obtained at the saddle point surface or for clusters with the critical cluster size.....76

5.11 (a) Onset activities and (b) the average mole fraction of water, *n*-nonane, and 1-butanol of the critical nuclei as function of the vapor-phase composition obtained at a_2' value of 0.5, 0.6, and 0.7.....78

5.12 NFEs (in units of k_BT) of the critical clusters (left; at a size of 36 molecules) and the post-critical clusters (right; at a size of 57 molecules) as function of the cluster composition at a_1 = 0.608, a_2' = 0.6 and a_3' = 0.14 79

5.13 Representative snapshots of clusters (consisting of 5, 10, 15, and 20 molecules of each component) obtained from the ternary nucleation simulations.....80

5.14 Entire onset activity surface obtained for the water/*n*-nonane/1-hexanol system from the simulation at a constant combined barrier height of 50.64 k_BT.....86

5.15 Onset activity curves obtained at a discretized set of a_2' varying from 0 to 1 at intervals of 0.2 for water/*n*-nonane/ethanol, water/*n*-nonane/1-butanol, water/*n*-nonane/1-hexanol, and water/*n*-nonane/1-octanol.....86

5.16 Average mole fraction of 1-alcohol in the critical nuclei as a function of its activity fraction obtained for binary (a) water/ethanol, (b) water/1-butanol, (c) water/1-hexanol, and (d) water/1-octanol 89

5.17 Plots of the reduced onset activities for the binary water/1-alcohol and *n*-nonane/1-alcohol series 90

5.18 Contour plot of the two-dimensional NFE as a function of the number of water and 1-hexanol molecules calculated from the simulation at $a_1 = 0.68$ and $a_3 = 0.40$ 90

5.19 Representative snapshots of binary water/1-alcohol clusters (consisting of 20 molecules of each component) obtained from the four systems using alcohols of different chain lengths 92

5.20 Representative snapshots for mixed clusters consisting of (a) 20 water and 20 *n*-nonane; (b) 20 water, 20 *n*-nonane, and 20 ethanol; (c) 20 water, 20 *n*-nonane, and 20 1-butanol; (d) 40 water, 40 *n*-nonane, and 40 1-butanol; (e) 20 water, 20 *n*-nonane, and 5 1-hexanol; (f) 20 water, 20 *n*-nonane, and 20 1-hexanol; (g) 5 water, 5 *n*-nonane, and 5 1-octanol; and (h) 12 water, 12 *n*-nonane, and 12 1-octanol 93

5.21 Average mole fraction of water, *n*-nonane, and 1-alcohol as a function of the normalized activity of 1-alcohol obtained at an a_2' value of 0, 0.2, 0.4, and others as specified at the top of each column 95

5.22 NFEs (in units of k_BT) as a function of cluster composition 98

5.23 NFEs (in units of k_BT) as function of cluster composition obtained for the water/*n*-nonane/1-octanol system at $a_1 = 0.88$, $a_2 = 0.88$, and $a_3 = 0.26$ for precritical clusters consisting of 15 molecules (left) or post critical clusters of 39 molecules (right) 100

5.24 Probability density profiles along the *z*-axis obtained for water oxygen, 1-octanol oxygen, 1-octanol carbon, and *n*-nonane carbon 101

6.1 Representative configurations of various clusters 106

6.2 Radial density profiles of various clusters 107

List of Abbreviations / Symbols

Λ	thermal de Broglie wavelength
β	$1 / k_B T$
δ	difference in number of molecules
ρ	probability
Γ	states
γ	surface tension
π	transition matrix
α	underlying matrix of the Markov chain
ΔE	change in energy
$\mu_g(p_g)$	chemical potential of the saturated vapor
ΔG^*	nucleation free energy barrier height
$\Delta G_{i/1}$	free energy of the i-mer or monomer
$\mu_{i/1}$	i-mer or monomer chemical potential
$\mu_l(p_l)$	droplet chemical potential
ρ_{liq}	liquid-phase density
$\Omega_n(E)$	density – of – state histogram
ρ_{vap}	saturated vapor-phase density
$<R>$	ensemble partition function
a	onset activity
A	surface area
acc	acceptance probability
AVBMC	aggregation-volume-bias Monte Carlo

AVUS – HR	AV (AVBMC), US, and HR combined
B	1-butanol
$B(T)$	curvature correction
BBMC	bond-bias Monte Carlo
CBMC	configuration-bias Monte Carlo
CNT	classical nucleation theory
COM	center of mass
CPU	central processing unit
DFT	density functional theory
DOS	density – of – state
f	normalized activity fraction
$f_{\mathrm{bias}}(n)$	n-mer biasing potential
GC	grand canonical
h	Planck's constant
$\mathbf{H}(\mathbf{r}^i)$	step function
HR	histogram-reweighting
ICNAA	International Conference on Nucleation and Atmospheric Aerosols
iU_o	mean-field-like average interaction energy between cluster and vapor
J	nucleation rate
J_o	kinetic prefactor
k_{B}	Boltzmann's constant
K_{CNT}	kinetic prefactor
L	total number of particles generated
LBA	Lee – Barker – Abraham
LJ	Lennard-Jones

m	mass
M	total number of clusters in a given volume
MASA	monomer-addition-subtraction algorithm
MC	Monte Carlo
MD	molecular dynamics
N	*n*-nonane
NFE	nucleation free energy
$n_{i/1}$	*i*-mer or monomer number of molecules
N_l	number of molecules inside the droplet
NpT	isobaric-isothermal ensemble
NT	nucleation theorem
n_v	gas-phase chemical potential
O	order / around
$p_1<\tau_i>$	average excluded volume interaction between *i*-mer and the vapor
p_g	saturated vapor pressure
$p_{i/1}$	pressure of *i*-mer or monomer
$P_{i/1}$	probability of finding *i*-mer or monomer
p_l	droplet pressure
$P_n(E)$	probability of observing an *n*-mer with energy *E*
pop	frequency or population
q_i	*i*-mer partition function
q_i'	transformed *i*-mer partition function using the COM coordinate system
r_g	radius of gyration
$\mathbf{r}^i$	position coordinate
$\mathbf{s}^N$	reference point

T	absolute temperature
TST	transition state theory
U_{cl}	cluster cutoff criterion
U_i	cluster potential energy
US	umbrella sampling
V	volume
V_l	droplet volume
W	water
$X_{i/1}$	i-mer or monomer
z_i	number of points generated per unit volume around a point

Abstract

For over a century, nucleation for all systems was thought simplistically to be a process that advances through the formation of critical clusters with a well-defined composition. Our results show intriguing nucleation mechanisms that challenge the aforementioned notion. We employed the simple TraPPE-UA (transferable potential for phase equilibria – united atom) force field and the AVUS-HR approach (a combination of aggregation-volume-bias Monte Carlo, umbrella sampling, and histogram reweighting), to investigate the homogeneous vapor-to-liquid nucleation of various nucleating systems. We found out that these systems could nucleate through a variety of unique non-ideal mechanisms. Alongside existing experimental investigations, this dissertation presents pioneering works on the computer simulation of nucleation in multicomponent systems. Our results are very relevant to atmospheric aerosol formations but may also find its applications in drug encapsulations and the design of nanomaterials as well as in sorting out experimental and theoretical discrepancies.

This dissertation outlines the results of a series of nucleation investigations involving unary, binary, and ternary nucleating systems. Introductory and background information regarding nucleation, computer simulations, the classical nucleation theory and the AVUS – HR approach are provided in Chapters 1 and 2. The major findings of this work are given in Chapters 3, 4, 5, and 6. They are presented here in order of increasing complexity. Chapter 3 is on unary nucleation of 1-pentanol. Chapter 4 is on the investigation of the *n*-Nonane/1-Alcohol binary series. Finally, our pioneering works on the various ternary nucleation studies are discussed in Chapters 5 and 6.

Chapter 1. Introduction

1.1 Nucleation and Computer Simulation

Nucleation phenomena play a vital role in many atmospheric, technological, and biological processes. Some of these processes include condensation and evaporation, crystal growth, and thin film deposition.[1] From the formation of atmospheric aerosols to the design of novel nanomaterials, nucleation is the critical first step in such processes. It is an activated process where a new phase is formed from a metastable supersaturated mother phase. As such, fundamental understanding of how particles and phases nucleate and grow is essential both in our path to technological breakthroughs and our awareness of climate change and its ill effects.[2-5] In this work, we focused on systems with one or more of the following compounds: water, *n*-nonane, and 1-alcohol. These three compounds represent polar/hydrophilic, nonpolar/hydrophobic, and amphiphilic/surfactant materials, respectively, in the atmosphere. Moreover, *n*-nonane, a hydrocarbon/oil, and water are everywhere and they are two of the most studied systems in homogeneous nucleation research. Knowing the immiscibility of water and oil, a surfactant compound that could link a polar and a nonpolar material is intriguing to investigate with. In addition, changing the alkyl chain length of the surfactant could provide us wealth of information on how the hydrophilic-lipophilic balance affects the behavior of the nucleating system. This study could provide insight on how condensation in a semi-complex (mimicked multicomponent system) atmosphere undergo. Multicomponent nucleation is of particular interest since in a realistic environment, various condensable species can participate in these processes. For instance, especially in coastal environments, the formation of atmospheric aerosols is thought to be a multiple component type of nucleation triggered by the homogeneous nucleation of water in the presence of sulfuric acid, ammonia, salts, organic substances, and

other trace species.[4,5] Although this dissertation is focused mainly on gas-to-liquid nucleation, in a broader sense, nucleation is involved in phenomena such as electron condensation in solids, diamond synthesis, volcanic eruption, micelle formation, the black hole formation, crack-mediated fracture, decompression sickness, the formation of particulate matter in space, earthquakes, the rupture of foam, the formation of electron-hole pairs in liquid semiconductors and a lot more.[1,6]

Due to the inherent difficulties involved in probing this process, nucleation studies have been vibrant for over a century. Since the pioneering work of Volmer and Weber,[7] and Becker and Döring,[8] a great deal of experimental and theoretical research has led to the recent emergence of sophisticated experimental[7-18] techniques that allow the measurement of nucleation rates with unprecedented accuracy not only for unary systems but also for multicomponent mixtures. Alongside, novel theoretical[21-29] and simulation[30-43] methods have been put forward for a more accurate description of nucleation. Recent breakthroughs in simulation methods have made computer simulation a complementary tool to study nucleation phenomenon using realistic, atom-based models.[37-40, 43-45]

Until the recent emergence of novel simulation techniques, molecular based information on atmospherically and technologically related nucleation phenomena remained highly elusive. The problem originates from the fact that nucleation is an activated process and probing and quantifying both the thermodynamic and structural properties of the critical nuclei is extremely difficult. The critical nuclei, which are at the top of the free energy barrier, are transient and have occurrence probabilities that are extremely low. Being statistically unfavorable species, critical nuclei are not amenable to direct experimental observation especially for multicomponent systems. Experimental information on the critical clusters often relies on indirect measurements

such as the use of the nucleation theorem (NT).[46-50] This approach yields the size and average composition of the critical cluster but not the distribution of compounds within the clusters. This interpreted composition is often insufficient to distinguish multiple nucleation pathways especially for systems that exhibit microscopic miscibility.[26, 28, 31, 38, 40, 44, 51-54] Examples are *n*-nonane/1-alcohol and water/1-alcohol mixtures for which the clusters can exhibit different miscibility behavior from bulk phases. As such, it is extremely appealing to resort to computer simulation as an alternative method to gather information on the molecular-level details of the nucleation process.

In principle, molecular simulation should still suffer from the same problem of extremely low occurrence probability for critical clusters. The advent of smarter simulation methodologies such as the development of AVUS-HR,[39,40] allows routine molecular investigation of the gas-to-liquid nucleation events for various systems.[40, 44, 45, 51] The AVUS-HR approach is a combination of aggregation-volume-bias Monte Carlo (AVBMC),[55-57] umbrella sampling (US),[58] and histogram reweighting (HR)[59-63]. One of the major advantages of this atomistic approach compared to other theoretical methods (such as classical nucleation theory and density functional theory) is its ability to use realistic, atom-based models that are parameterized to experimentally known thermodynamic properties such as phase equilibrium data.[37-40, 44, 45, 51, 52] As such, results from molecular simulations can be qualitatively compared to experimentally measured or interpreted nucleation data. Furthermore, these simulations can provide molecular-level information that includes the thermodynamic free energy landscape and the structural arrangements and distribution of species inside all the clusters sampled during the simulation.

Moreover, compared to laboratory experiments, computer simulations are in a better position to handle extreme conditions such as very high pressure and temperature. The

complementary use of computer simulations with laboratory experiments could also minimize the wasteful use of chemicals. In a general sense, computer simulation is used to understand macroscopic behaviors by utilizing the chemistry of the microscopic world. In particular for complex multicomponent systems, an in-depth understanding of the relation between microscopic interactions and their corresponding macroscopic consequences could put us in a better position to make accurate predictions in the absence of experimental data.

Computer simulation has a dual purpose. It can both serve as a test of theories and a basis for evaluating conflicting experimental results. Due to this dual function, computer simulation has the capability to bridge between models and theoretical predictions on one hand and between models and experimental results on the other,[64] acting as a bridge between theory and experiment. Moreover, aside from being cheap, clean, and able to handle extreme conditions, computer simulation allows control of time resolution,[57] and can be used as a purely exploratory tool[65].

To elaborate this "bridging" function of computer simulation, let us take this specific scenario. Prior to 1995, using a plethora of experimental nucleation techniques, significant inconsistencies between nucleation rate measurements using different techniques and disagreement between theoretical predictions and experimental results and between simulation and theory/experiments have been reported. These problems prompted the nucleation community to benchmark existing methods.[66] During the 1995 Prague *Workshop on Nucleation Experiments – State of the Art and Future Developments*,[66] a consensus to perform a joint 1-pentanol nucleation experiment in a well-defined standard system was reached. Instead of clearing up contradictions in the previous experimental results, these experiments "seem to raise even more questions about the quality of the different techniques".[19] Prompted by this quagmire, computer

simulation can be utilized as a bridge between theory and experiment and, hence, can help to rank the different experimental measurements.

As unusual as it may sounds, computer simulation can also be used as an exploratory tool.[65] It can be utilized to look into the possible atmospheric nucleation of the major gaseous component in the Martian atmosphere. It has been suggested that the Martian atmosphere could only support simple atmospheric processes[67] but the difficulty and expense of experiments on Mars makes this difficult to verify. A computer simulation that mimics Martian conditions can be set-up and the results could possibly provide us insight into the fate of Mars' atmospheric vapors and provide knowledge of the complexity or simplicity of extraterrestrial atmospheric processes.

1.2 The Classical Nucleation Theory and Beyond[68]

Let us first look into the free energy change as the process of forming a spherical cluster from the starting homogeneous vapor-phase occurs. The total energy of the system contains the surface, and the bulk contributions.[68] We can then describe the energy of the initial state or the homogeneous vapor as follows

$$U = T_0 S - pV + \gamma A + \sum \mu_i N_i \tag{1.1}$$

while the energy of the homogeneous part of the system is given by

$$U_0 = T_0 S_0 - p_0 V_0 + \sum \mu_{i,g}^0 N_{i,g}^0. \tag{1.2}$$

The subscripts 0, *g*, *l*, and *s* refer to initial state, gas, liquid, and surface, respectively. The variables *T*, *S*, *p*, *V*, γ, *A*, *i*, μ, *N* are the temperature, entropy, pressure, volume, surface tension, surface area, component identity, chemical potential, and number of molecules, respectively. The final energy of the system comprising of the cluster surrounded by the vapor has the form

$$U = T_0 S - p_g V_g - p_l V_l + \gamma A + \sum \mu_{i,g} N_{i,g} + \sum \mu_{i,l} N_{i,l} + \sum \mu_{i,s} N_{i,s}. \tag{1.3}$$

In this situation, the free energy of the nucleating system could be properly described using an appropriate ensemble or set of conditions. These sets of conditions could be very well represented by the three ensembles, namely, the canonical ensemble, the grand-canonical ensemble, and the isobaric isothermal ensemble.

In the canonical ensemble, variables such as the number of molecules (*N*), the volume (*V*), and the temperature (*T*) are kept constant. Under this set of conditions, equations 1.4 to 1.6 are true.

$$N_{i,tot} = N_{i,g} + N_{i,l} + N_{i,s} = N_{i,g}^{0} \tag{1.4}$$

$$V_{tot} = V_g + V_l \tag{1.5}$$

$$T_0 = T \tag{1.6}$$

The characteristic free energies for this ensemble (Helmholtz free energy) are

$$F_0 = U_0 - T_0 S_0 = p_0 \left(V_l + V_g\right) + \sum \mu_{i,g}^{0} N_{i,g}^{0} \tag{1.7}$$

$$F = U - T_0 S = -p_g V_g - p_l V_l + \gamma A + \sum \mu_{i,g} N_{i,g} + \sum \mu_{i,l} N_{i,l} + \sum \mu_{i,s} N_{i,s} \tag{1.8}$$

for the initial (1.7) and final state (1.8). Using equations 1.7 and 1.8, the change in the Helmholtz free energy change, ΔF has the form

$$\Delta F = (p_0 - p_l)V_l + \left(p_0 - p_g\right)V_g + \gamma A + \sum(\mu_{i,g} - \mu_{i,g}^{0})N_{i,g} + \sum(\mu_{i,l} - \mu_{i,g}^{0})N_{i,l} + \sum(\mu_{i,s} - \mu_{i,g}^{0})N_{i,s}. \tag{1.9}$$

Assuming that the gas pressure is unperturbed ($p_0 = p_g$), and since the composition is unchanged, then according to the Maxwell relation, at constant composition (x_i) and temperature (T)[68]

$$d\mu_i = v_i dp \tag{1.10}$$

and the chemical potential should also be the same, $\mu_{i,g} = \mu^{0}_{i,g}$. The symbol v_i is the partial molecular volume. As such, equation 1.9 can be simplified into equation 1.11.[68]

$$\Delta F = (p_0 - p_l)V_l + \gamma A + \sum(\mu_{i,l} - \mu_{i,g}^0)N_{i,l} + \sum(\mu_{i,s} - \mu_{i,g}^0)N_{i,s} \quad (1.11)$$

In the grand-canonical ensemble, variables such as the chemical potential (μ), the volume (V), and the temperature (T) are kept unchanged. In this set of conditions equations 1.5 and 1.6 are still true. In addition $\mu_{i,g} = \mu^0_{i,g}$. The grand free energy for the initial state is

$$\Omega_0 = U_0 - T_0 S_0 - \sum \mu_{i,g}^0 N_{i,g}^0 = -p_0 V_0 = -p_0(V_l + V_g) \quad (1.12)$$

and

$$\Omega = U - T_0 S - \sum \mu_{i,g}^0 N_{i,tot} = U - T_0 S - \sum (N_{i,g} + N_{i,l} + N_{i,s})\, \mu_{i,g}^0 \quad (1.13)$$

$$= -p_g V_g - p_l V_l + \gamma A + \sum(\mu_{i,l} - \mu_{i,g}^0)N_{i,l} + \sum(\mu_{i,s} - \mu_{i,g}^0)N_{i,s}$$

for the final state. Using the Maxwell's relation (equation 1.10), and equations 1.12 - 1.13, the grand free energy difference, $\Delta\Omega$ is[68]

$$\Delta\Omega = (p_0 - p_l)V_l + \gamma A + \sum(\mu_{i,l} - \mu_{i,g}^0)N_{i,l} + \sum(\mu_{i,s} - \mu_{i,g}^0)N_{i,s} \quad (1.14)$$

Finally, for the isobaric isothermal case, the number of molecules (N), the pressure (p), and the temperature (T) are constant, $p_0 = p_g$, and equations 1.4 and 1.6 hold true. The initial and final Gibbs free energy are

$$G_0 = U_0 - T_0 S_0 + p_0 V_0 = \sum \mu_{i,g}^0 N_{i,g}^0 \quad (1.15)$$

$$G = U - T_0 S + p_0 V_{tot} = U - T_0 S + p_0 (V_g + V_l) \quad (1.16)$$

$$= (p_0 - p_l)V_l + \gamma A + \sum \mu_{i,g} N_{i,g} + \sum \mu_{i,l} N_{i,l} + \sum \mu_{i,s} N_{i,s}$$

and the Gibbs free energy difference, ΔG has the form[68]

$$\Delta G = (p_0 - p_l)V_l + \gamma A + \sum(\mu_{i,l} - \mu_{i,g}^0)N_{i,l} + \sum(\mu_{i,s} - \mu_{i,g}^0)N_{i,s}. \quad (1.17)$$

As shown, equations 1.11, 1.14, and 1.17 are equal ($\Delta F = \Delta\Omega = \Delta G$), and at the equilibrium, the terms with summation vanish and the work of formation for CNT is normally presented in these forms (equations 1.18 – 1.20)[8, 68-71]

$$\Delta G = (p_0 - p_l)V_l + \gamma A \tag{1.18}$$

$$\Delta G(r) = 4\,\pi\, r^2\,\gamma + \frac{4}{3}\,\pi\,\rho\, r^3\ \Delta\mu \tag{1.19}$$

$$\Delta G(n) = 4\,\pi\,(\frac{3}{4\,\pi})^{2/3}\,\frac{\gamma}{\rho^{2/3}}\,n^{2/3} + n\,\Delta\mu \tag{1.20}$$

Moreover, the barrier height can be obtained by maximizing the free energy difference, ΔG with respect to the radius (r) or to the number of molecules (n), and has the form[8, 68-71]

$$\Delta G^* = (16\,\pi\,\gamma^3)\ /\ (3\,\rho^2\ \Delta\mu^2). \tag{1.21}$$

Also, the critical radius (r*) and the critical cluster size (n*) can be approximated using equations 1.22 and 1.23. [8, 68-71]

$$r^* = (2\,\gamma)\ /\ (\rho\,|\Delta\mu|) \tag{1.22}$$

$$n^* = (32\,\pi\,\gamma^3)\ /\ (3\,\rho^2\,|\Delta\mu|^3) \tag{1.23}$$

The classical nucleation rate has the form[19] (widely used by experimentalists)

$$J_{\mathrm{CNT}} = K_{\mathrm{CNT}}\ exp(-\Delta G^*_{\mathrm{CNT}}\ /\ k_{\mathrm{B}}T) \tag{1.24}$$

where

$$K_{\mathrm{CNT}} = (2\gamma\ /\ \pi m)^{1/2}\ v_l N_1^2 \tag{1.25}$$

$$\Delta G^*_{\mathrm{CNT}} = \frac{16}{3}\pi\ v^2\gamma^3\ /\ (k_{\mathrm{B}}T\ lnS)^2 \tag{1.26}$$

$$S = p_1\ /\ p_1^{eq} \tag{1.27}$$

Due to the widespread failure of CNT in predicting nucleation rates, various modifications to the work of formation have been proposed. Girschick and Chiu[72] proposed a self-consistent (SC) CNT where the contribution from the monomer work of formation is removed and a 1/S term is inserted in the exponential part.

$$\Delta G_{\mathrm{SC-CNT}}(n) = \Delta G_{\mathrm{CNT}}(n) - A_1\gamma_\infty + k_B T \ln S \tag{1.28}$$

Using a phenomenological approach, Dillman and Meier (DM)[73] argued that corrections must be made both in the four (translational, rotational, vibrational, and configuration) degrees of freedom (τ and q_0) as well as in the surface energy deviation of the cluster from the macroscopic droplet (K_i).

$$\Delta G_{\mathrm{DM}}(n) = K_i A_n \gamma_\infty - n k_B T \ln S + \tau k_B T \ln n - k_B T \ln q_0 V + k_B T \ln N_{tot} \quad (1.29)$$

Other extensions of the CNT involve length scale correction (replacement free energy, R) by Reiss, Kegel, and Katz (RKK)[74]

$$\Delta G_{\mathrm{RKK}}(n) = \Delta G_{\mathrm{CNT}}(n) - k_B T \ln R + k_B T \ln S \quad (1.30)$$

and the additional non-equilibrium translational and rotational corrections from Reguera and Ruby (RR)[75] to the RKK

$$\Delta G_{\mathrm{RR}}(n) = \Delta G_{\mathrm{RKK}}(n) + 4 k_B T \ln n \quad (1.31)$$

Independent from the classical nucleation theory, nucleation theorems present alternative ways of obtaining nucleation information. These two theorems derived entirely from statistical mechanics are the 1st nucleation theorem by Kaschiev[49,76-78]

$$(d(\Delta G^*)/\, d(lnS))_T = -\Delta n^* \quad (1.32)$$

$$(d(\ln J)/\, d(lnS))_T = \Delta n^* + 1 \quad (1.33)$$

and the 2nd nucleation theorem by Ford[50]

$$(d(\Delta G^*)/\, d(T))_\mu = -\Delta S^* \quad (1.34)$$

$$(d(\ln J)/\, d(T))_\mu = (1/k_B T^2)[(\Delta H)^2 + \Delta U^* - k_B T] \quad (1.35)$$

where ΔH and ΔU^* are the enthalpy of vaporization, and energy difference, respectively.

Chapter 2: The AVUS – HR Approach

2.1 Introduction

All the investigations of nucleation in this dissertation are empowered by the recently developed AVUS-HR approach.[39, 40] By combining AVBMC,[55, 56] US,[58] and HR[59-63], the resulting approach delivers superior efficiency in the study of rare nucleation events. The advantage of this method in studying rare events lies in its ability to overcome several types of sampling difficulties including the large free energy barriers (or low probabilities for the occurrence of clusters near the critical nucleus size) and the inherent micro-heterogeneity of the phase space (i.e., coexistence of monomers and clusters). This was achieved through US[58] and AVBMC[55, 56], respectively. The incorporation of the configurational-bias Monte Carlo (CBMC) scheme[79-81] further improves its efficiency by enhancing the acceptance rate for particle exchanges and most importantly, allows the use of realistic, atom-based force fields, thus enabling direct comparisons with experimental results. Moreover, since large energy fluctuations occur in the sampling of small clusters, it is advantageous to perform HR. Using HR,[59-63] the probability (or free energy) information for neighboring thermodynamic states can be obtained *without additional simulations*.[38, 40]

2.2 Nucleation in the Grand Canonical Ensemble

2.2.1 Cluster Definition

The cluster definition is an integral part of molecular simulations. Since molecules do not carry labels identifying their membership in a group or cluster, a rather arbitrary yet reasonable designation has been put forward. A review on this topic and its importance to the nucleation process is given by Senger and coworkers.[82] Under the classical nucleation theory (CNT),[8, 21-23, 69-71] the cluster is defined as a liquid drop surrounded by meta-stable phase (e.g. supersaturated

vapor) and has bulk-like properties such as density and interfacial tension. Authors of analytical molecular theories have categorized cluster definitions into five different classes. These are (1) the microcrystalline cluster, (2) the stable cluster, (3) the Stillinger cluster, (4) the density functional cluster, and (5) the Monte Carlo simulative cluster. In the computer simulation community, clusters have been defined using bonding energy,[83] nearest neighbor connectivity,[84] rigid spherical volume (LBA cluster),[85] connectivity to liquid-like particles,[30] combined volume and connectivity,[86] TST (Transition State Theory) dividing surface or evaporation rate minimization,[87] and quasibound dynamics[88]. In all the work presented here, we used an energy-based Stillinger-type of cluster criterion. We defined the cluster as a group of molecules in which every molecule has at least one neighbor in the group with interaction energy less than the cutoff criterion, U_{Cl}.

2.2.2 Free Energy of Formation[32,36]

The nucleation free energy of formation, ΔG_i, can be defined as the reversible work of transforming i monomers to one i-mer (see equation 2.1) at the partial pressure of the monomer, p_1, (see equation 2.2) or as the i-mer chemical potential difference at pressures p_i and p_1 (see equation 2.3),[32,36]

$$i\, X_1 \rightleftharpoons X_i \tag{2.1}$$

$$\Delta G_i = \mu_i(p_1) - i\,\mu_1(p_1) \tag{2.2}$$

$$\Delta G_i = \mu_i(p_1) - \mu_i(p_i) \tag{2.3}$$

where X_1 and X_i are the monomer and i-mer, respectively. By performing Gibbs-Duhem integration on the ideal gas equation,[32] the term $\mu_i(p_1)$, is approximately

$$\mu_i(p_1) \approx \mu_i(p_i) + k_B T \ln(n_1 / n_i). \tag{2.4}$$

By substituting equation 2.4 to equation 2.2, we can have an expression relating free energy to the number of monomer and *i*-mer molecules as follows:

$$\Delta G_i = \mu_i(p_i) + k_B T \ln(n_1 / n_i) - i\,\mu_1(p_1) \tag{2.5}$$

Since the combination of equation 2.2 and 2.3 leads to $\mu_i(p_i) = i\mu_1(p_1)$, then equation 2.5 can be written as

$$\Delta G_i = k_B T \ln(n_1 / n_i). \tag{2.6}$$

2.2.3 Cluster in the Grand Canonical Ensemble

Using a Stillinger-type[84] or any appropriate cluster criterion, the partition function of an *i*-mer can be written as follows

$$q_i = \frac{1}{i!\,\Lambda^{3i}} \int_0^V H(\mathbf{r}^i) \exp[-\beta U_i(\mathbf{r}^i)]\ \mathrm{d}\mathbf{r}^i \tag{2.7}$$

where $\Lambda = (h^2 / (2\pi m k_B T))^{1/2}$ is the thermal de Broglie wavelength, h is Planck's constant, m is mass, k_B is Boltzmann constant, T is absolute temperature, $\beta = 1 / k_B T$, U_i is the cluster potential energy, $\mathbf{r}^i$ is the position coordinate, and $H(\mathbf{r}^i)$ is the unit step function (that assumes a value of 1 if the cluster criterion is obeyed and zero if not). The cluster criterion, as a consequence, restricts the displacement of the molecules within a small region from the center-of-mass (COM). As such, equation 2.7 can be reformatted using the COM coordinate system[32] as follows:

$$q_i' = \frac{i^3 V}{i!\,\Lambda^{3i}} \int_0^V H(\mathbf{r}'^{i-1}) \exp[-\beta U_i(\mathbf{r}'^{i-1})]\ \mathrm{d}\mathbf{r}'^{i-1} \tag{2.8}$$

The new terms i^3 and V are from the Jacobian of the coordinate transformation and from the integration over the COM coordinate, respectively.[32,36]

Using a small-system grand canonical ensemble, Oh and Zeng[32] found out that the most probable number of *i*-mers is as follows:

$$n_i = i^{3/2}\,\Lambda^{-3}\,V\,q_i'\exp(\beta i\mu_1)\exp(-\beta p_1 < \tau_i >)\exp(-\beta i U_o) \tag{2.9}$$

where $p_1\langle\tau_i\rangle$ is the average excluded volume interaction between *i*-mer and the vapor molecules, and $iU_0 = n_1U_1 / 2$, is the mean-field-like average interaction energy due to the attraction between the cluster and the vapor. These two terms will vanish upon assuming that the vapor-cluster interaction is negligible and equation 2.9 becomes

$$n_i = i^{3/2}\,\Lambda^{-3}\,V\,q_i^{'}\exp(\beta i\mu_1). \tag{2.10}$$

This assumption is only acceptable at conditions where the ideal gas approximation is true (low density phases).[34, 35, 55] From equation 2.10, we can say that the total number of clusters (M) in volume, *V* is

$$\mathrm{M} = \sum_{i=1}^{i_{max}} n_i = \sum_{i=1}^{i_{max}} i^{3/2}\,\Lambda^{-3}\,V\,q_i^{'}\exp(\beta i\mu_1) \tag{2.11}$$

and the probability of finding an *i*-mer in *V* is

$$\begin{aligned}\mathrm{P}_i &= n_i \,/\, \mathrm{M} \;=\; n_i \,/\, \sum_{i=1}^{i_{max}} n_i \\ &= \left(i^{3/2}\,\Lambda^{-3}\,V\,q_i^{'}\exp(\beta i\mu_1)\right)/\left(\sum_{i=1}^{i_{max}} i^{\frac{3}{2}}\,\Lambda^{-3}\,V\,q_i^{'}\exp(\beta i\mu_1)\right).\end{aligned} \tag{2.12}$$

Since $\mathrm{P}_1 = n_1 / \mathrm{M}$ or $n_1 = \mathrm{P}_1\mathrm{M}$, then equation 2.6 can also be written as follows:

$$\Delta G_i = k_\mathrm{B}T\ln(\mathrm{P}_1\mathrm{M} / \mathrm{P}_i\,\mathrm{M}) = k_\mathrm{B}T\ln(\mathrm{P}_1 / \mathrm{P}_i) \tag{2.13}$$

2.3 Metropolis Monte Carlo[89]

Our inability to analytically obtain the partition function in macroscopic systems due to the overwhelming dimensionality of the phase space leads to the use of importance sampling developed by Metropolis and coworkers.[89] As the name "important sampling" implies, for integration problems, instead of doing calculations on all points, this method performs calculation only on important points where the Boltzmann factor is not negligible. Consider equation 2.14, used to calculate the average value of a measurable property *R*, instead of focusing on the denominator (configurational part of the partition function), Metropolis et al. suggested an efficient Monte Carlo scheme to sample such a ratio[65, 89]

$$< R >= \frac{\int ds^N \exp\left[-\beta U(s^N)\right] R(s^N)}{\int ds^N \exp\left[-\beta U(s^N)\right]} \tag{2.14}$$

$$N(s^N) = \frac{\exp\left[-\beta U(s^N)\right]}{\int ds^N \exp\left[-\beta U(s^N)\right]} \tag{2.15}$$

$$z_i = L\, N(s^N) \tag{2.16}$$

$$< R >= \frac{1}{L} \sum_{i=1}^{L} z_i \; R(s_i^N) \tag{2.17}$$

where equation 2.15 is the probability distribution to randomly generate points in configuration space, L is the total number of points generated, and z_i is the number of points generated per unit volume around a point s^N. In the Metropolis Monte Carlo scheme, equation 2.14 is transformed to equation 2.17. Using this form, we are only required to calculate $\exp[-\beta U(s^N)]$ but not both $\exp[-\beta U(s^N)]$ and $\int ds^N \exp[-\beta U(s^N)]$ (configurational part of the partition function). In this case, only $\exp[-\beta U(s^N)]$, the relative probability of visiting various points in configuration space is known. In a more concrete example, the scheme suggests that in measuring the depth of Mississippi River within the state of Louisiana, measurements will only be done within the path of the river and not in any other locations in Louisiana. The implementation of this method involves the use of a Markov chain, a sequence of trials where the outcome of each trial solely depends on the outcome of the previous trial and the outcome of each trial belongs to a state space or finite set of outcomes $\{\Gamma_1, \Gamma_2, \ldots, \Gamma_m, \Gamma_n, \ldots\}$. Here the transition matrix, π connects the two states Γ_m and Γ_n.[64]

For clarity, let us say, for example, that a power interruption during manual ballot counting in the Philippines follows a certain known pattern. The pattern is as follows. If the power interruption happens on one day, then the next day has a 20% chance of having the same problem (off-off chance is 20%, off-on chance is 80%). If the power is on for the entire day, the chance of having a power interruption on the next day would soar up to 90% (on-off chance is

90%, on-on chance is 10%). As such the transition matrix for this particular scenario is of the form (off and on written on columns and rows are legends),

$$\pi = \begin{pmatrix} & off & on \\ off & 0.20 & 0.80 \\ on & 0.90 & 0.10 \end{pmatrix}.$$

If we begin with the assumption that the two events, with (off) and without (on) power interruption, have equal chances to occur, then the initial probability has the state space,

$$\rho^{(1)} = \begin{pmatrix} off & on \\ 0.50 & 0.50 \end{pmatrix}.$$

The probability of having a power interruption on the second day is of the matrix form,

$$\rho^{(2)} = \rho^{(1)}\,\pi = (0.50, 0.50)\begin{pmatrix} 0.20 & 0.80 \\ 0.90 & 0.10 \end{pmatrix}$$

$$= (0.50\ x\ 0.20 + 0.50\ x\ 0.90, 0.50\ x\ 0.80 + 0.50\ x\ 0.10)$$

$$= (0.55, 0.45)$$

with a 55 % chance of a power interruption. The next day will have a 51.50 % chance of an electrical outage.

$$\rho^{(3)} = \rho^{(2)}\pi = \rho^{(1)}\,\pi\,\pi = \rho^{(1)}\,\pi^2 = (0.55, 0.45)\begin{pmatrix} 0.20 & 0.80 \\ 0.90 & 0.10 \end{pmatrix}$$

$$= (0.55\ x\ 0.20 + 0.45\ x\ 0.90, 0.55\ x\ 0.80 + 0.45\ x\ 0.10)$$

$$= (0.515, 0.485)$$

In the long run, the chance can be predicted by the general formula (or the limiting distribution),

$$\rho = \lim_{t\to\infty}(\rho^{(1)}\,\pi^t). \tag{2.18}$$

From equation 2.18, ρ must satisfy the eigenvalue equation

$$\rho\,\pi = \rho \tag{2.19}$$

$$\sum_m \rho_m\,\pi_{mn} = \rho_n. \tag{2.20}$$

with 1 as the eigenvalue.[57, 64] By definition, the rows in a stochastic matrix add up to unity.

$$\sum_n \pi_{mn} = 1 \tag{2.21}$$

A way to satisfy equations 2.19 and 2.20 is by imposing a strong condition of "microscopic reversibility",[57, 64]

$$\rho_m \, \pi_{mn} = \rho_n \, \pi_{nm} \tag{2.22}$$

since

$$\sum_m \rho_m \, \pi_{mn} = \sum_m \rho_n \, \pi_{nm} = \rho_n \sum_m \pi_{nm} = \rho_n \tag{2.23}$$

and the Metropolis et al.[89] solution, also known as the asymmetrical solution, to the transition probability matrix, π, is,[57,64]

$$\pi_{mn} = \alpha_{mn} \qquad \rho_n \geq \rho_m \qquad m \neq n \tag{2.24}$$

$$\pi_{mn} = \alpha_{mn} \left(\frac{\rho_n}{\rho_m}\right) \qquad \rho_n < \rho_m \qquad m \neq n \tag{2.25}$$

$$\pi_{mm} = 1 - \sum_{n \neq m} \pi_{mn} \tag{2.26}$$

where α, known as the underlying matrix of the Markov chain, is a symmetrical stochastic matrix ($\alpha_{mn} = \alpha_{nm}$).

In 1953, Metropolis et al. introduced the following random walk algorithm/approach.[65, 89] Metropolis translational move:

1. Randomly select particle i and calculate its energy, E_A.
2. Give particle i a random displacement, and calculate its new energy, E_B.
3. Calculate the change in potential energy, $\Delta E = E_B - E_A$
4. Accept the move using the probability,

$$acc(A \rightarrow B) = \min\left[1, exp\left(-\frac{\Delta E}{k_B T}\right)\right] \tag{2.27}$$

For strongly associating fluids, the standard Metropolis Monte Carlo method[89] fails.[55] This is due to the use of a symmetric underlying Markov matrix that results to low efficiency of locating the

few bonded configurations in the vastness of phase space. Furthermore, its standard acceptance rule makes the destruction of bonded configurations very slow.[55] In fact this scheme has been modified to handle simulations of various challenging systems especially in the simulation of rare events such as nucleation.

2.4 Aggregation-Volume-Bias Monte Carlo (AVBMC)[35,39, 55-57]

Since the conventional Metropolis Monte Carlo technique uses a symmetrical underlying Markov matrix and utilizes solely the Boltzmann weight for the acceptance probability, its implementation especially for systems of highly associating fluids like H_2O and HF is ineffective.[57] There are two main issues with the conventional Metropolis Monte Carlo scheme. First, the volume of the bonded region is very small compared to the total volume of the phase space. As a consequence, the ratio between the volume of the bonded region and the total phase space volume is very low. This would equate to very infrequent occurrences of moving a particle from a non bonded region to the bonded region. Secondly, the difference in the energies of the bonded and non bonded states is large. This energetic penalty causes very low acceptance in bonding to non bonding moves. In summary, the Metropolis Monte Carlo scheme could either miss forming bonded configurations or be trapped in a bonded configuration. It would ultimately succumb to the problem of poor sampling (and the obtained ensemble averages may not be reliable) of the phase space which could eventually be solved by running simulations for an extremely long time. But such a solution is computationally expensive. A smarter way to solve such problems is to directly increase the transition probability for moves from non bonded to bonded region and enhance the acceptance rate for bonding to non bonding moves.[57]

The goal of biased algorithms is to alleviate the deficiency of the conventional Monte Carlo algorithm and ultimately provide a reasonable procedure to sample the entire phase space.

These algorithms are the association-biased Monte Carlo (ABMC),[90, 91] the bond-bias Monte Carlo (BBMC),[92] the monomer-addition-subtraction algorithm (MASA),[93, 94] and the aggregation-volume-bias Monte Carlo (AVBMC) method.[55, 56] ABMC is not that easy to implement and is CPU time intensive since it involves 2-particle displacement that necessitates a specific determination of the bonding regions.[90, 91] Although BBMC is simpler than ABMC, it requires that one molecule should be within another's known bonding volume.[92] On the other hand, the MASA algorithm does not allow branched-aggregate formation and is limited to bivalent associating fluids.[93, 94] The bias introduced in these algorithms is then corrected by adjusting the acceptance rule. A detailed discussion on this topic is found elsewhere.[94]

The aggregation-volume-bias Monte Carlo (AVBMC)[55, 56] algorithm attempts to work on the shortcomings of these prior schemes. Its basic tenet is efficiency in hopping from bonded and non bonded configurations. This is done by introducing a biased intra-box swap move. This move is analogous to the particle swap moves used in grand canonical and Gibbs ensemble simulations. The following outlines the steps of an AVBMC trial intra-box swap move.[55-57]

AVBMC intra-box swap move:

1. Randomly select a 1st particle i and calculate its energy, E_A.
2. Randomly select a 2nd particle j (where j acts as the target molecule and $j \neq i$).
3. Case A: With a probability of P_{bias}, swap particle i to B_{in} (bonded region of particle j) and calculate its energy, E_B.

   Case B: With a probability of 1- P_{bias}, swap particle i to B_{out} (non-bonded or outside the bonded region of particle j) and calculate its energy, E_B.
4. Calculate the change in potential energy, $\Delta E = E_B - E_A$

5. Case A: For events that do not involve particle i entering (out→in) or leaving (in→out) the bonded region of particle j, meaning, only for out→out and in→in cases, accept the move using the probability,

$$acc(A_{out} \rightarrow B_{out}) = \min\left[1, \exp\left(-\frac{\Delta E}{k_B T}\right)\right] \quad (2.27)$$

$$acc(A_{in} \rightarrow B_{in}) = \min\left[1, exp\left(-\frac{\Delta E}{k_B T}\right)\right] \quad (2.27)$$

Case B: For out → in case, that results in the formation of a bonded configuration of i and j, accept the move using the probability,

$$acc(A_{out} \rightarrow B_{in}) = \min\left[1, \frac{(1-P_{bias})\,V_{in}}{P_{bias}\;V_{out}} \exp\left(-\frac{\Delta E}{k_B T}\right)\right] \quad (2.28)$$

Case C: For in → out case, that results in the destruction of a bonded configuration of i and j, accept the move using the probability,

$$acc(A_{in} \rightarrow B_{out}) = \min\left[1, \frac{(P_{bias})\,V_{out}}{(1-P_{bias})\,V_{in}} exp\left(-\frac{\Delta E}{k_B T}\right)\right] \quad (2.29)$$

AVBMC also uses an asymmetric underlying Markov matrix. The bias introduced in this matrix is then removed by a correction factor in the acceptance rule. By doing this, the detailed balance condition or the condition of microscopic reversibility is satisfied for all four cases (in → out, in → in, out → out, and out → in). Moreover, unlike other biased algorithms, the AVBMC algorithm is model independent and allows all types of bonded aggregates to form. The additional computational cost comes from the selection of particle j, the determination of whether particle i is *in* or *out* of the bonded region of particle j, and from the trial site exploration. Since these sources are system size independent, the additional cost is deemed negligible for all practical cases.[55-57]

For the grand canonical implementation, the following outlines the intra-box swap moves:

1. With equal probabilities, randomly perform deletion or insertion.
2. Randomly select the target particle (j) for the swap move.
3. Case A. Insertion move: Insert particle from the ideal gas phase to a randomly chosen position in the in region of particle j.

   Case B. Deletion move: Randomly choose a particle from the in region of j to be deleted.
4. Calculate the potential energy difference of the two states.
5. Case A. Accept the insertion move using the following acceptance probability,[55, 56]

$$acc(A \rightarrow B) = \min\left[1, \frac{N\ V_{in}}{(N+1)(N_{in}+1)} exp\left(\frac{\mu}{k_B T}\right) exp\left(-\frac{\Delta E}{k_B T}\right)\right] \quad (2.30)$$

   Case B. Accept the deletion move using the following acceptance probability,[55, 56]

$$acc(A \rightarrow B) = \min\left[1, \frac{N\ N_{in}}{(N-1)\ V_{in}} exp\left(-\frac{\mu}{k_B T}\right) exp\left(-\frac{\Delta E}{k_B T}\right)\right] \quad (2.31)$$

where μ is the chemical potential of the ideal gas.

2.5 Umbrella Sampling (US) [56, 58]

Umbrella sampling is a technique that enhances sampling of high free energy configurations to facilitate faster convergence of the cluster distributions.[56, 58] To achieve reasonable sampling of the clusters near the barrier height (*e.g.*, low probability area $O(10^{-30})$), an exceedingly long simulation must be performed both for Monte Carlo or Molecular Dynamics simulations. In the umbrella sampling technique, this issue has been addressed through the use of a removable biasing potential. This potential enhances the frequencies of all the clusters and thereby hastens the convergence. In a study of vapor-liquid nucleation for a Lennard-Jones

system performed by ten Wolde and Frenkel,[30] they chose the harmonic function based on the size of the largest cluster, *n*, of the form

$$W_{bias} = \frac{1}{2} k (n - n_0)^2 \tag{2.32}$$

The k and n_0 in their approach dictate the width and location of a window of cluster sizes to be sampled and by increasing n_0, the size of the cluster is also increased.[30] In their study, 15 windows (simulation runs) were used to calculate the nucleation free energy barrier.

The implementation of the biasing potential could be further improved by enhancing the frequencies of all cluster sizes of interest in a single window, eliminating the need for multiple simulations. This is done by using a biasing potential that is the negative of the cluster's nucleation free energy, $-\Delta G(n)$. Since $\Delta G(n)$ is not known in advance, the biasing potential, $f_{\text{bias}}(n)$, is solved iteratively using a self-adapting procedure for up to $n = 20$ molecules. A good approximation of the biasing potential for $n > 20$ molecules can be obtained by using the classical nucleation theory (see Chapter 1),[8, 69-71]

$$\Delta G(n) = 4\pi(\frac{3}{4\pi})^{2/3} \frac{\gamma}{\rho^{2/3}} n^{2/3} + n\Delta\mu. \tag{1.20}$$

At large values of *n*, *i.e.*, 15-20 molecules, equation 1.20 can be utilized to predict the nucleation free energy of neighboring cluster sizes.[41, 95-97]

$$\begin{aligned} \delta\Delta G(n) &= \Delta G(n) - \Delta G(n-1) \\ &= 4\pi(\frac{3}{4\pi})^{2/3} \frac{\gamma}{\rho^{2/3}} \left[n^{2/3} - (n-1)^{2/3}\right] + [n-(n-1)]\Delta\mu \\ &= 4\pi(\frac{3}{4\pi})^{2/3} \frac{\gamma}{\rho^{2/3}} \left[n^{2/3} - (n-1)^{2/3}\right] + \Delta\mu \end{aligned} \tag{2.33}$$

By utilizing the free energy at $n \geq 15$, the plot of $\delta\Delta G(n)$ vs. $n^{2/3} - (n-1)^{2/3}$ yields a straight line. After obtaining the equation of the line, extrapolation can be done to obtain nearby $\Delta G(n)$. This

can be extended to multicomponent systems by considering the nucleation free energy of one component at a time.

The biasing potential can be removed in the final calculation of the nucleation free energy as follows,

$$\Delta G(n) = -k_B T \ln \frac{pop_n}{pop_1} - f_{bias}(n) \quad (2.34)$$

where pop_1 and pop_n are the monomer and *n*-mer frequencies/populations (number of times visited), respectively.

2.6 Histogram-Reweighting (HR)[59-63]

The incorporation of histogram-reweighting technique[59-63] enhances the capability of our approach by mining additional useful information without resorting to additional simulations.[39] Histogram-reweighting involves sorting of simulation data in the forms of histograms of fluctuating observables. In the microcanonical ensemble, the system can access the same set of microcanonical states under different simulation conditions with different probabilities. That is, the microcanonical partition function of a given system of *n*-mer cluster is a function of energy only and is independent of simulations parameters such as temperature and chemical potential. The one-dimensional histogram $\Omega_n(E)$ can be constructed as follows[39]

$$\Omega_n(E) = P_n(E) \exp[\frac{(-n\mu_1 + E)}{k_B T}] \quad (2.35)$$

where T, k_B, μ_1, $P_n(E)$ are the absolute temperature, Boltzmann's constant, the gas-phase (monomer) chemical potential, and the probability of observing an *n*-mer with energy, *E*, respectively. With this density-of-state histogram, the calculation of the nucleation free energy of formation of the *n*-mer, ΔG_n^*, at a standard state of $n_v^* = 1$ molecule per $Å^3$ is as follows[36-39]

$$\Delta G_n^* = -k_B T \ln[\int \Omega_n(E) \exp(-\frac{E}{k_B T}) \, dE] \quad (2.36)$$

and at any other gas-phase chemical potential or monomer density n_v by applying

$$\Delta G_n = \Delta G_n^* - (n-1)k_B T \ln \frac{n_v}{n_v^*}. \quad (2.37)$$

Equation 2.37 can be traced back to equation 2.38, the cluster size distribution as follows:

$$P(n)/\,P(1) = \exp(-\Delta G_n\,/k_B T) \quad (2.38)$$

The implementation of this technique to multicomponent nucleation is straightforward except for some modifications to the computation of the density-of-states (DOS) histograms. For example, in a binary system for a cluster with a given composition (n_1, n_2), where n_1 and n_2 denote the number of molecules for type 1 and 2, respectively, the DOS histograms $\Omega_{(n1,n2)}(E)$ can be constructed from the simulations as follows:

$$\Omega_{(n_1,n_2)}(E) = P_{(n_1,n_2)}(E)\ \exp[\frac{(-n_1\mu_1 - n_2\mu_2 + E)}{k_B T}] \quad (2.39)$$

where $P_{(n1,n2)}(E)$ is the absolute probability density (expressed in terms of droplets per cubic angstrom) to observe this cluster with an intermolecular energy value of E, μ_1 and μ_2 are the gas-phase (monomer) chemical potentials for type 1 and 2, respectively, k_B is Boltzmann's constant, and T is the absolute temperature. With these DOS histograms $\Omega_{(n1,n2)}(E)$, we can extract the absolute probability density at any other gas phase chemical potentials (μ_1 and μ_2) and temperature ($T^* = T + \Delta T$) using the following equation:

$$P^*_{(n_1,n_2)} = \int \Omega_{(n_1,n_2)}(E)\ \exp(\frac{n_1\mu_1^* - n_2\mu_2^* + E}{k_B T^*})\ dE] \quad (2.40)$$

Correspondingly, the NFE of this cluster can be calculated from

$$\Delta G^*_{(n_1,n_2)} = -k_B T^* \ln[P^*_{(n_1,n_2)}(E)] \quad (2.41)$$

Such extrapolation is valid provided that there are significant overlaps of the states sampled at these two different temperatures. Typically for the cluster-size range of our interest, the extrapolated results were found acceptable if T^* ranges from T- 30 K to T + 30 K.

Chapter 3. Exploring the Discrepancies between Experiment, Theory, and Simulation for the Homogeneous Gas-to-Liquid Nucleation of 1-Pentanol

3.1 Introduction

As with other experiments (including molecular simulation as a computational experiment), nucleation rate measurements are subject to systematic and random errors. These errors contribute to the significant deviations between experimental results using different methods, between experiments and simulations, or between experiments / simulations and classical nucleation theory (CNT). Comparing CNT with either simulation or experiment is extremely difficult due to CNT's failure to properly describe small clusters.[41, 95-97] On the other hand, since simulations of nucleation processes are highly sensitive to the description of the intermolecular interactions, a direct comparison to experimental results would require simulations with a level of accuracy that existing force fields cannot meet.[39, 41, 43, 98, 99] However, for a consistent model, simulations on a variety of systems indicated that the sources of error for CNT are contained in the non-zero work of formation for the monomer as well as deviations due to non-compact small clusters. These errors accumulate into a large offset between the barrier height predicted by CNT and calculated by simulations.[41, 95-97] Moreover, simulation studies on water using different models have shown that the offset due to the small clusters (excluding the monomer) is relatively model-independent.[95] Therefore, it is tempting to suggest that this part of the deviation between simulation and CNT for a consistent model system would be comparable to that observed between the experiment and CNT for the corresponding real system. Indeed, using an argon system, we were able to show that experiment and simulation disagree roughly equally with CNT at reasonably high temperature.[41] In this work, a detailed nucleation investigation was carried out on 1-pentanol. As will be shown, the results obtained here allow us

to gauge the relative agreement between simulation and experiment, identify outlying experimental results, and sort out discrepancies.

3.2 Simulation Details

For computational efficiency, all simulations in this work were performed using the grand-canonical version of the nucleation algorithm. Here a single cluster is physically isolated from the rest of the system. As part of the simulation conditions, the number density (or chemical potential) of the vapor phase (treated as an ideal gas) is specified. The total energy was computed by summing up all pair interactions for the entire cluster. The Transferrable Potential for Phase Equilibria - United Atom, TraPPE-UA, force field was used to model 1-pentanol.[81,93] Since it is a 7-site chain molecule, we employed an energy-based Stillinger-type cluster criterion.[84] That is, we defined a cluster as a group of molecules in which every molecule has at least one neighbor in the group with interaction energy of less (more favorable) than –260 k_B K. As previously observed, the choice of cluster criterion (as long as it is reasonable) does not significantly affect the nucleation free energies.[37,39] Simulations were done at 3 different temperatures: 235, 280, and 340 K. HR was used to obtain the complete set of data from 220 K to 360 K. Each cluster size was visited at least 10^9 times.

3.3 Results and Discussions

In the classical nucleation theory (CNT),[8, 69-71] the cluster's free energy of formation, $\Delta G(r)$ (see equation 1.19) or $\Delta G(n)$ (see equation 1.20) (where r is the radius of the cluster and n is the number of molecules in the cluster), is given by the surface (1st term) and the bulk free energy (2nd term) involved in a particular phase transition,

$$\Delta G(r) = 4\pi r^2 \gamma + \frac{4}{3}\pi r^3 \rho \Delta\mu \qquad (1.19)$$

or

$$\Delta G(n) = 4\pi(\frac{3}{4\pi})^{2/3}\frac{\gamma}{\rho^{2/3}}n^{2/3} + n\Delta\mu. \tag{1.20}$$

In CNT, these clusters are assumed to be perfectly compact and spherical, with bulk-like properties such as density (ρ), surface tension (γ), and chemical potential (μ). Although these assumptions break down toward small clusters, for sufficiently large droplets, CNT provides a convenient procedure to extrapolate bulk information from finite sized clusters[41, 95-97]

$$\begin{aligned}\delta\Delta G(n) &= \Delta G(n) - \Delta G(n-1)\\ &= 4\pi(\frac{3}{4\pi})^{2/3}\frac{\gamma}{\rho^{2/3}}\left[n^{2/3} - (n-1)^{2/3}\right] + [n-(n-1)]\Delta\mu\\ &= 4\pi(\frac{3}{4\pi})^{2/3}\frac{\gamma}{\rho^{2/3}}\left[n^{2/3} - (n-1)^{2/3}\right] + \Delta\mu\end{aligned} \tag{2.33}$$

Using equation 2.33, CNT predicts that a plot of $\delta\Delta G(n)$ vs. $n^{2/3} - (n-1)^{2/3}$ yields a straight line. Our simulation data are plotted in this form in Figure 3.1. Although most of the points for a given temperature lie on a straight line (CNT prediction), small clusters (i.e., $n < 15$) deviate significantly from the CNT prediction. As shown, the deviation is highest at the lowest temperature and decreases toward higher temperatures. The sum of the ΔG difference between CNT and simulation for, small clusters ($2 \leq n < 15$) is referred to as $B(T)$ in Merikanto and coworkers.[95] (Note in this calculation, the linear fit was performed only on the portion of the $\delta\Delta G$ data obtained by the simulation for clusters with $n > 14$ (see Figure 3.2) from which both $\gamma / \rho^{2/3}$ (= slope/4.836) and $\Delta\mu$ (= y-intercept) were obtained. Together with the bulk phase density

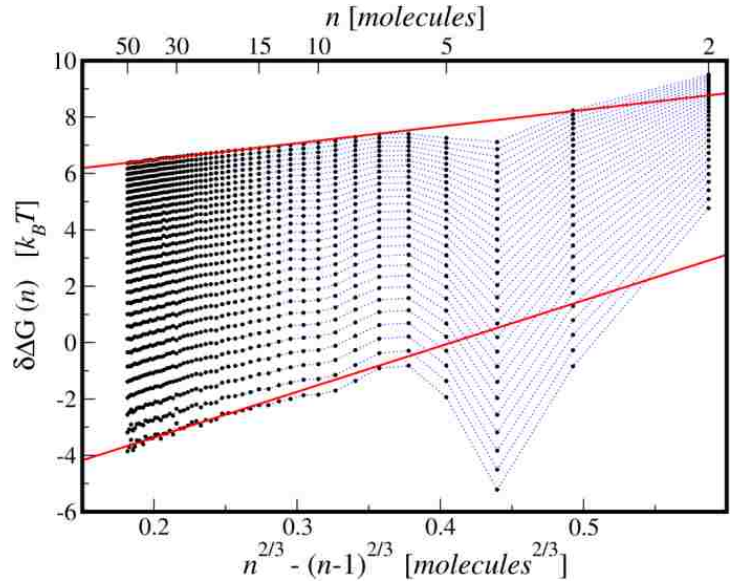

Figure 3.1. $\delta\Delta G(n)$ plotted against the function $n^{2/3} - (n\text{-}1)^{2/3}$ for 29 different temperatures. From bottom to top, these temperatures are 220 K – 360 K in 5 K intervals.

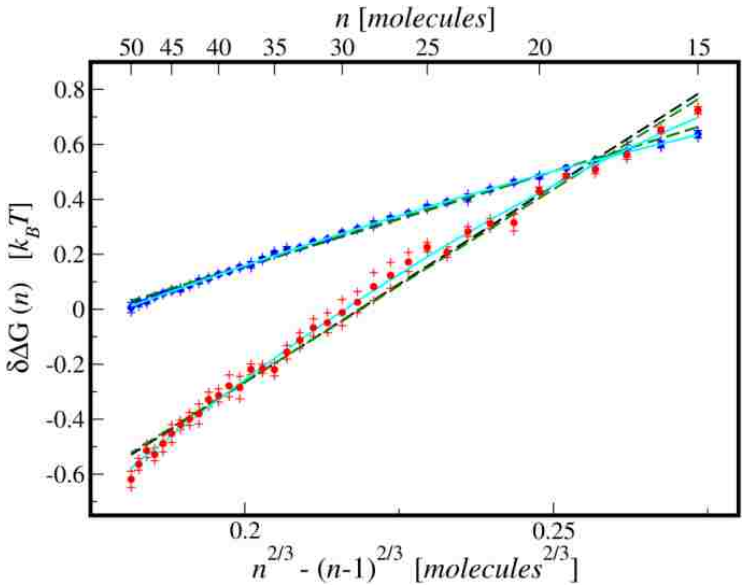

Figure 3.2. Magnification of the portion of Figure 3.1 where the linear fits are performed ($15 \leq n \leq 50$). For clarity, only the data at 235 K (red) and 340 K (blue) are shown. The dashed black line, dashed green line, and the cyan line are the resulting standard linear fit, weighted linear fit, and nonlinear (cubic) fit for each temperature. The cross pertains to the standard deviation of each point.

(ρ) data obtained from an additional *NpT* ensemble simulations, the CNT predicted surface tension (γ) was calculated). The $B(T)$ effect and the ΔG (1) (non-zero ΔG for the monomer in CNT) make up the total deviation, $\Delta\Delta G^*$, between the ΔG^*_{CNT} and ΔG^*_{SIM}.[41, 95]

For a given temperature, Becker and Döring[8] stipulated that the classical nucleation rate (J_{CNT}) has both a classical kinetic prefactor (K_{CNT}) and a thermodynamic barrier height (ΔG^*_{CNT}) component and is of the form:

$$J_{CNT} = K_{CNT} e^{-\Delta G^*_{CNT} / k_B T}. \tag{1.24}$$

From equation 1.24, a similar mathematical expression can also be written for the nucleation rate obtained from simulation (J_{SIM}). The ratio between these two nucleation rates would be

$$\ln\left(\frac{J_{SIM}}{J_{CNT}}\right) = \ln\left(\frac{K_{SIM}}{K_{CNT}}\right) + \frac{\Delta G^*_{CNT} - \Delta G^*_{SIM}}{k_B T}. \tag{3.1}$$

If the contribution from the natural logarithm of the pre-factor ratio, {ln (K_{SIM} / K_{CNT})}, is negligible,[100] then the natural logarithm of the nucleation rate ratio between simulation and CNT, {ln (J_{SIM} / J_{CNT})}, can directly be obtained through the differences in their barrier heights, (ΔG^*_{CNT} - ΔG^*_{SIM}) / $k_B T$. In all our succeeding analysis, we use a vapor density where the simulation predicted barrier height is 25 $k_B T$ while the nucleation barrier height encountered in the experiment is much higher (~40 $k_B T$). However, roughly equal value of {ln (J_{SIM} / J_{CNT})} obtained (see Figure 3.3) regardless of the choice of simulation predicted barrier heights (20, 25, 30, 35, and 75 $k_B T$), simply because the critical nucleus is already quite big (containing more than 15 molecules) whereas most of the deviation on the nucleation free energy values between simulation and CNT occurs at much smaller cluster sizes (see Figure 3.1).

Iland and coworkers[19] performed a comparative analysis between experiments and CNT (see Figure 6 in Iland et al.[19]). This reduced data is depicted together with our simulation data in Figure 3.4 and enables experimentalists and simulators to determine inconsistencies among the

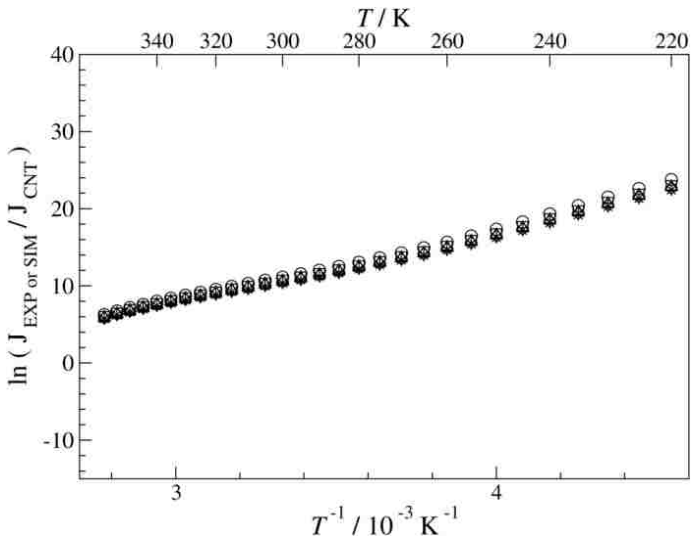

Figure 3.3. Natural logarithm of the nucleation rate ratio as a function of inverse temperature obtained at various conditions where the simulation predicted barrier height is 20 (star), 25 (diamond), 30 (triangle), 35 (square), and 75 k_BT (circle).

measurements as well as detect discrepancies with CNT.[19] Although the experimental results (using various techniques) coincide at 260 K, the temperature dependence of the nucleation rate ratio is rather inconsistent. Most of the experimental data[9, 13, 15, 18, 19] show a positive slope for the nucleation rate ratio versus inverse temperature (i.e., an increase of the deviations with decreasing temperature), whereas a few experimental data[10, 17] show roughly constant deviations or even the opposite trend.[101] From this figure, an interesting coincidence between our simulation results and the experimental data of Iland and coworkers[19] and Hruby and coworkers[9] can be noticed, i.e., a very good agreement of the slope, but a near-constant shift to larger differences to CNT for the simulation data when the $B(T)$ effect is included. Using a least squares linear

regression, slopes of 130 K (Ar carrier gas),[19] 230 K,[9] and 110 K (our results) and *y*-intercepts of –19.0 (Ar carrier gas),[19] –8.1,[9] and –19.6 (our results) are found. The linear regression yields *x*-intercepts (where ln $\{J_{EXP/SIM}/J_{CNT}\}$ = 0) of about 400 K (Ar carrier gas),[19] 540 K,[9] and 460 K (our data). Temperatures within the range of these *x*-intercepts could be of interest in performing

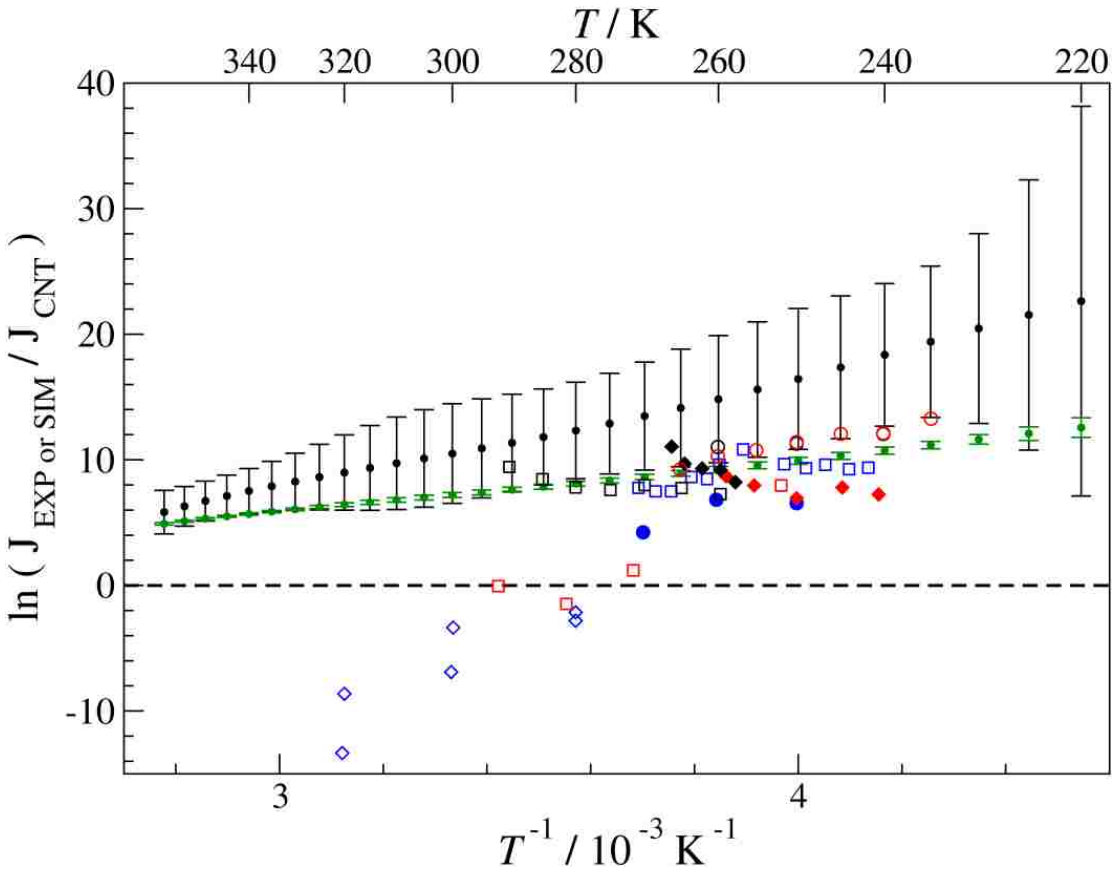

Figure 3.4. Natural logarithm of the nucleation rate ratio between experiment (or simulation) and CNT as a function of inverse temperature. The CNT prediction is shown as dashed horizontal line. The present simulation data including and excluding the $B(T)$ effect are depicted as filled black and green circles with error bars, respectively. The experimental data are shown as follows: nucleation pulse chamber with Ar (red open circle[19] and blue open square[9]) and He carrier gas[19] (black open circle), upward thermal diffusion cloud chambers with He carrier gas[13] (blue open diamond), expansion cloud chamber with Ar carrier gas[18] (red open square), laminar flow diffusion chamber with He carrier gas (filled black diamond[101] and black open square[17], piston-expansion tube with N_2 carrier gas[15] (filled blue circle), and expansion wave tube with He carrier gas[10] (shaded red diamond).

future standardized experiments. Furthermore, as suggested by McGraw and Laaksonen,[100] a single scaling parameter that depends only on temperature, $D(T)$, could be used to systematically remove the discrepancies between CNT and experiment. In addition, Iland and coworker[19] hinted that from the linear least square analysis, the slope could be used to correct the enthalpy and the *y*-intercept for entropy correction. From these results, we suggest that further experimental investigations at higher temperatures should be done to further assess the rather promising agreement between our simulations and experimental data of Iland and coworkers.[19]

As mentioned earlier, the total deviation in the ΔG^* between simulation and CNT can be attributed to the $B(T)$ effect as well as the difference in the ΔG value of the monomer (i.e., zero in simulation vs. $A_1\gamma - |\Delta\mu|$ in CNT).[41, 95] Figure 3.5 shows how these contributions significantly affect the overall offset. These contributions generally decrease with increasing temperature. The temperature dependence of $\Delta\Delta G^*$ is similar to both the $B(T)$ (with large uncertainties) and the $A_1\gamma$ (with minimal uncertainties) contributions. Moreover, the $|\Delta\mu|$ and $B(T)$ contributions decrease with increasing temperature thus making $A_1\gamma$ the major overall offset contributor. Although the curvature correction $B(T)$ which is related to the compressibility of the nucleus[30, 31, 102, 103] seems to show some sensitivity to the temperature (in contrast to previous reports[41, 95] of a nearly negligible temperature dependence of this property for other systems, such as LJ and water), the data reported here are also associated with very large error bars (comparable to the magnitude of $B(T)$ itself), arising mainly from the uncertainty in the linear interpretation of Figure 3.1's $\delta\Delta G$ data as described above. In particular, the slopes obtained from these linear fits come with much larger errors toward lower temperatures. Zooming of the portion of the $\delta\Delta G$ data used for the linear fits at 235 and 340 K (see Figure 3.2), (even with exceedingly long simulation runs) reveals more pronounced uncertainties from linearity at lower

temperatures (uncertainties of 2.68%, 2.37%, and 1.57% for the slope and of 1.71%, 1.68%, and 1.30% for the y-intercept at 235, 280, and 340 K, respectively). As shown in Figure 3.2, even if we consider the uncertainties, there are significant numbers of outlying points (cross does not touch the line). Even with the use of a weighted linear fit, outlying points still exist. In particular,

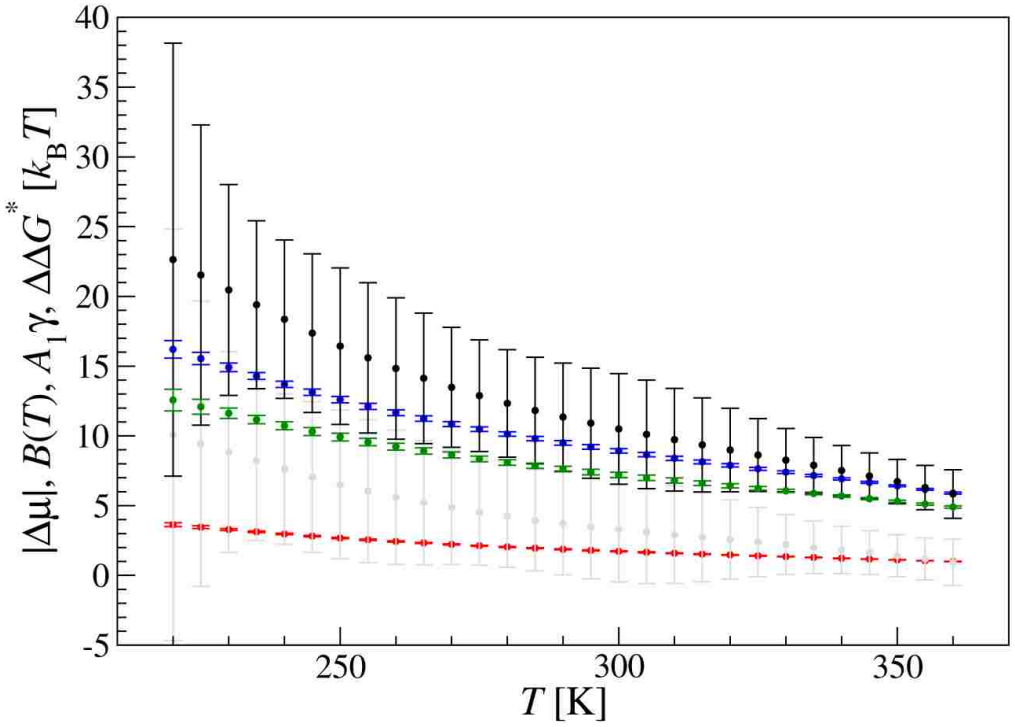

Figure 3.5. ΔG^* difference between CNT and simulation (black) as a function of temperature. The several contributions are separated above as $A_1\gamma$ (blue), $B(T)$ (gray), and $|\Delta\mu|$ (red). $\Delta\Delta G^*$s without the $B(T)$ effect are in green circles with error bars.

at 235 K, the use of the weighted linear fit significantly shifts the slope and y-intercept by 2.00% and 1.89%, respectively. It is tempting to interpret that the $\delta\Delta G$ data used for linear fit reveals a systematic "concave" curvature (see cyan line in Figure 3.2). While this systematic departure from linear behavior could pose another source of error for CNT, it also questions the accuracies on the bulk properties extrapolated from these clusters especially toward lower temperatures. As

such, it may be more appropriate to use bulk-phase simulations to determine quantities that are needed in the CNT predictions. However, extremely precise/accurate estimates of these properties would be required and the commonly reported data obtained from these bulk-phase simulations have errors that far exceed the range that is acceptable here, e.g., a 1% error on the surface tension (an order of magnitude smaller than the typical error associated with bulk-phase simulations) would already produce uncertainties of 1.80 and 0.87 k_BT for the estimation of the $B(T)$ term at 235 and 340 K, respectively.

For CNT and experiments, especially at high temperature, the major contributor in the $\Delta\Delta G^*$ offset could come from $A_1\gamma$ and $|\Delta\mu|$. Without the $B(T)$ effect, this would suggest that the $\Delta\Delta G^*$ difference between simulation and experiment comes from the ($A_1\gamma_{SIM} - A_1\gamma_{EXP}$) and ($|\Delta\mu|_{SIM} - |\Delta\mu|_{EXP}$) (or the free energy of the monomer). Using NpT simulations, we calculated the densities (ρ) of 1-pentanol at different temperatures. Furthermore, surface tension (γ) values at various temperatures were calculated using the calculated densities and the slopes ($4.836\gamma/\rho^{2/3}$) from the $\delta\Delta G(n)$ vs. $n^{2/3} - (n\text{-}1)^{2/3}$ plot in Figure 3.1 (see equation 2.33 for derivation). The values used for density (see equation 3.2)

$$\rho / kgm^{-3} = \sum_{i=0}^{5} a_i \left(1 - \frac{T}{588.15}\right)^{i/3} \tag{3.2}$$

$a_0 = 270$ $\quad$ $a_3 = 19226.001$

$a_1 = 1930.229$ $\quad$ $a_4 = -18559.303$

$a_2 = -8414.762$ $\quad$ $a_5 = 6555.718$

and surface tension (see equation 3.3)

$$\sigma / Nm^{-1} = 0.02685469 - 7.889 \times 10^{-5}(T - 273.15) \tag{3.3}$$

in the experiments[10-12, 17, 19, 101] are in excellent agreement with our obtained density and surface tension values (see Figure 3.6a,b). This agreement has an uncertainty of less than 0.5 k_BT for the ($A_1\gamma_{SIM}$ - $A_1\gamma_{EXP}$) (see Figure 3.6c). As such, considering the $B(T)$ effect and the free energy of the monomer (with a modest ($|\Delta\mu|_{SIM}$ - $|\Delta\mu|_{EXP}$) of around 1 k_BT), the experimental results that are in good agreement with our results should lie near the shaded black circles in Figure 3.4. On the other hand, assuming that the $B(T)$ effect is negligible (as suggested by Merikanto et al.[95] on various water models), then the experimental results that are in good agreement with our results should lie 1-2 units above or below the shaded green circles in Figure 3.4.

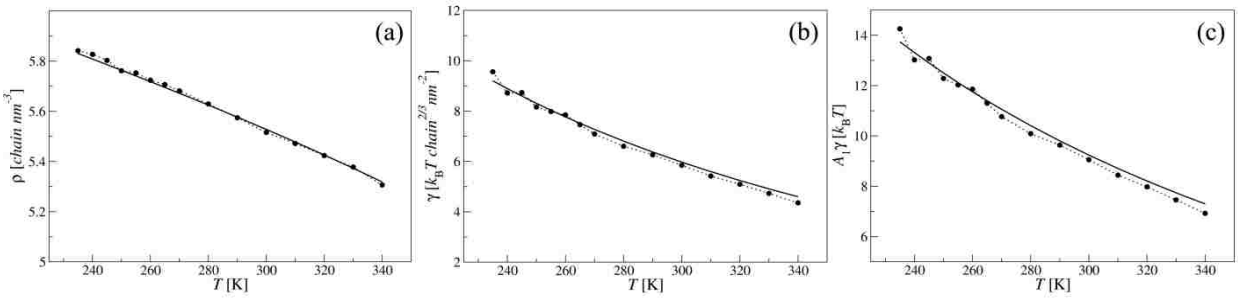

Figure 3.6. Comparison between experiment (solid black line) and simulation results (circles) for the temperature dependence of the (a) density, (b) surface tension, and (c) $A_1\gamma$ contribution.

The positive values for ln (J_{SIM} / J_{CNT}) signifies overestimation of ΔG^* for CNT (ΔG^*_{CNT} > ΔG^*_{SIM}). In contrast, data points lying below the dashed line in Figure 3.4 suggest underestimation of ΔG^* for CNT. These data are problematic since the work of formation for a monomer in CNT is always positive causing the said overestimation of the ΔG^* for CNT. Furthermore, the ln (J_{SIM} / J_{CNT}) data have a positive slope with inverse temperature because of the corresponding temperature dependence of the surface free energy of the monomer, $A_1\gamma$ (= 4.836 $\gamma/\rho^{2/3}$), with temperature. We can categorically attribute this trend to the surface tension, γ.

Although the density term ($\rho^{2/3}$) also decreases with temperature, the magnitude of the decreasing surface tension (γ) is the deciding factor.

In light of these discrepancies in the nucleation of 1-pentanol, we have investigated the molecular origin of these peculiarities. By inspection of Figure 3.1, we notice that the dip and non-CNT conforming points ($n < 15$) resemble those observed for water molecules. Figure 3.7, a comparison of the log-log plot of the aggregation number versus the reduced radius of gyration (r_g/r_l) for water, 1-pentanol, and LJ systems reveals an interesting similarity between the features of water and 1-pentanol. We found out that even for small clusters (n of up to 14 1-pentanol molecules), the slopes (corresponding to various temperatures) tilt more toward the water curve than to the LJ system curve. Much more, from $n \geq 15$, the slope is close to 3 regardless of the temperature, and the 1-pentanol clusters are compact. In addition, Figure 3.8 shows that clusters of 1-pentanol molecules can exhibit stable extended cyclic hydrogen bonded aggregates. These cyclic hydrogen bonded aggregates may exist as single or multiple rings.

To test the aforementioned observations, we performed hydrogen bonding analyses for 14, 28, and 46-molecule clusters at 235, 280, and 340 K. Here a hydrogen bonded aggregate is defined using the following criteria: $r_{OO} \leq 3.3$ Å, $r_{OH} \leq 2.5$ Å, $\cos\theta_{OH\ldots OL} \leq -0.1$, and $u_{head} \leq -13$ kJ/mol. The potential energy between the two $-CH_2OH$ head groups is the u_{head}, the angle between the OH bond vector on the donating molecule and the oxygen lone pair vector on the accepting molecule is the $\cos\theta_{OH\ldots OL}$, and the r_{OO} and r_{OH} are the oxygen-oxygen and the oxygen-hydrogen distance, respectively. [104, 105] Results are shown in Table 3.1. These values are in great agreement with the results obtained from the additional *NpT* (bulk phase) simulations using 500 1-pentanol molecules performed at various temperatures. Since the overwhelming fraction of 1-pentanol molecules has two neighbors, indeed, 1-pentanol forms stable cyclic

structures. This scenario where a 1-pentanol molecule is hydrogen bonded to approximately two 1-pentanol neighboring molecules has also been observed in various other neat alcohols.[104-108]

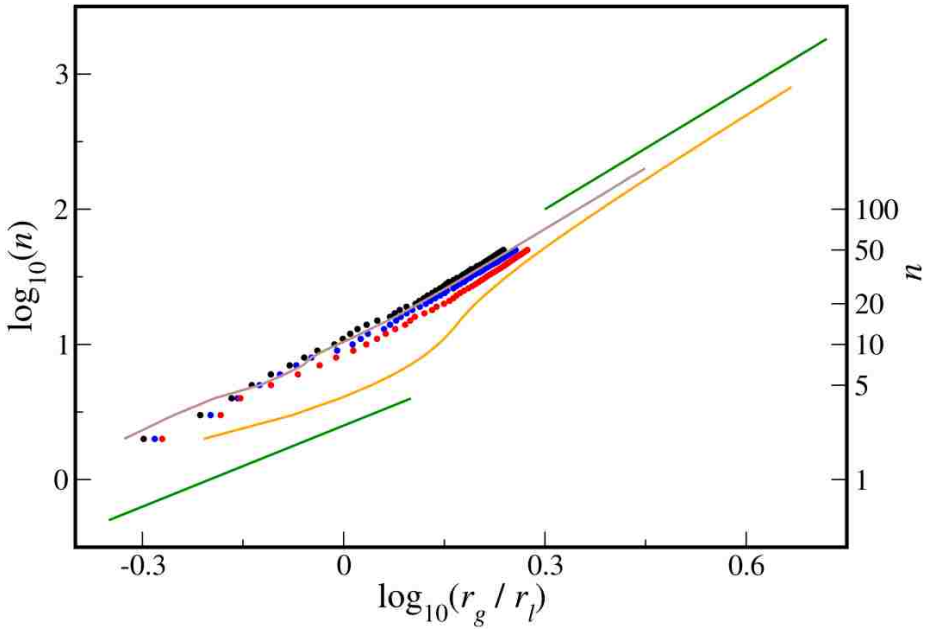

Figure 3.7. Log – log plot of *n*-pentanol cluster size versus the reduced radius of gyration at 235 K (black), 280 K (blue), and 340 K (red). The factor r_l (the reciprocal of the cube root of the number density of the liquid phase, $\rho_l^{-1/3}$) is used to place the various systems on the same scale. For comparison, LJ (orange) and water (brown) systems are also included in the plot. Data were obtained at $T^* = 0.6$ and the Stillinger cluster criterion at 1.5σ was used for the LJ system and at $T = 230$ K using an energy cutoff criterion of -260 k_B K for water.[43] The green lines indicate 2-D and 3-D dimensional growth.

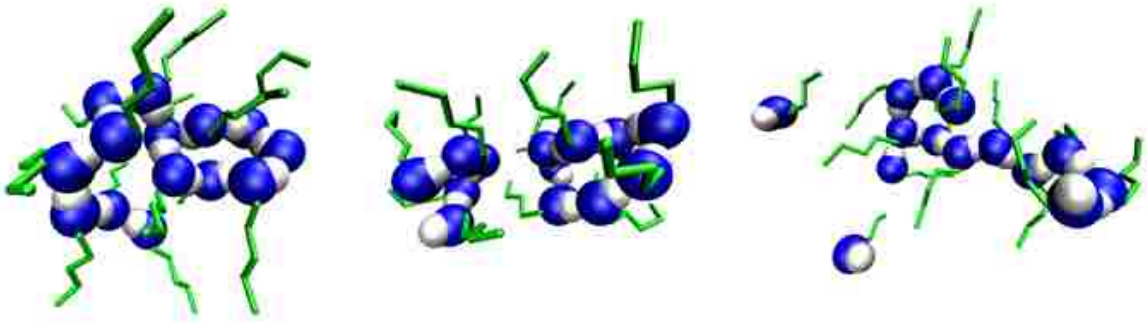

Figure 3.8. Snapshots of clusters containing 14 1-pentanol molecules taken at 235 K (left), 280 K (middle), and 340 K (right). Color notation: oxygen (blue); hydrogen (white); and alkyl tails (green stick).

Furthermore, we calculated the fraction of molecules involved in different sized hydrogen bonded aggregates within a single cluster. For the 14-molecule clusters (see Figure 3.9a), at lower temperature, more molecules are involved in forming a single 14-molecule hydrogen bonded aggregate. As temperature increases, more molecules are involved in forming pentameric 1-pentanol hydrogen bonded aggregates than any other sizes. For the 28-molecule clusters (see Figure 3.9b) and 46-molecule clusters (see Figure 3.9c), at 235 K, although large aggregates are

Table 3.1. Average hydrogen bond number of 1-pentanol molecule at a specific temperature (235, 280, and 340 K) and cluster size (14, 28, and 46-molecule cluster). Data obtained from additional *NpT* (bulk phase) simulation using 500 1-pentanol molecules at various temperatures are also included. Subscripts are the statistical uncertainties of the last decimal places.

	235 K	280 K	340 K
14	1.960_{8}	1.884_{16}	1.638_{17}
28	1.957_{7}	1.881_{9}	1.644_{13}
46	1.956_{7}	1.880_{21}	1.657_{9}
500	1.961_{2}	1.893_{4}	1.705_{5}

dominant, with multiple size can be found in the same cluster. This shows that even for unary 1-pentanol, micro-heterogeneity within a single cluster occurs. As temperature increases, structural reorganization may occur leading to more uniform aggregates in a cluster. Furthermore, as shown in Figure 3.9(d-f), an increase in temperature favors small hydrogen bonded aggregates with predominantly 5 molecules. The population of these multiple large aggregates decreases with increasing temperature shifting the scenario from cluster with heterogeneous aggregates (see Figure 3.9d,e) to cluster with uniform aggregates (see Figure 3.9f). The minima at sizes

close to the maximum size are caused by the low propensity for non-hydrogen-bonded molecules, i.e., a cluster of *N* molecules prefers to break up into one large cluster of *N*–5 molecules and a pentameric cluster. In comparison to the bulk phase simulations (see Figure 3.9(d-f), unlike clusters at 340 K, low temperature (235 and 280 K) clusters are far from being bulk like. At lower temperatures, 50-molecule hydrogen bonded aggregates and bigger exist while at 340 K, hydrogen bonded aggregate are no bigger than 50 molecules. Indeed, it is only at higher temperature that the bulk like CNT assumption works and, hence, this contributes to the discrepancy between simulation and CNT. This information could be construed as caution in extrapolating nucleation information via cluster based analysis. Such analysis should be done on a case to case basis. In this particular case, at least 100 1-pentanol molecules should be investigated to obtain a bulk like behavior at temperatures of 235 and 280K.

In addition, we compared the hydrogen bonded aggregate profile from the cluster-based simulations and bulk phase *NpT* simulations (see Figure 3.9(d-f). Here we also observed the formation of large aggregates, coexistence of aggregates of multiple sizes, and at changing profile with temperature. In particular, at 235 K (Figure 3.9d) and 280 K (Figure 3.9e), even a 46-molecule cluster, does not yet mimic the bulk behavior. As shown, results from *NpT* simulations at 235 K might experience poor aggregate sampling for molecules of this type. This issue could be addressed by optimizing the CBMC scheme or by implementing parallel tempering / replica exchange techniques.[109-112] While at 340 K, the aggregate distribution in the 28 and 46-molecule cluster are almost bulk-like with minor differences for *n*-aggregate above and below 10. For $n < 10$, the fraction of molecules forming these aggregates is higher compared to the bulk, whereas for $n > 10$, the opposite is observed. This non-bulk-like behavior exhibited

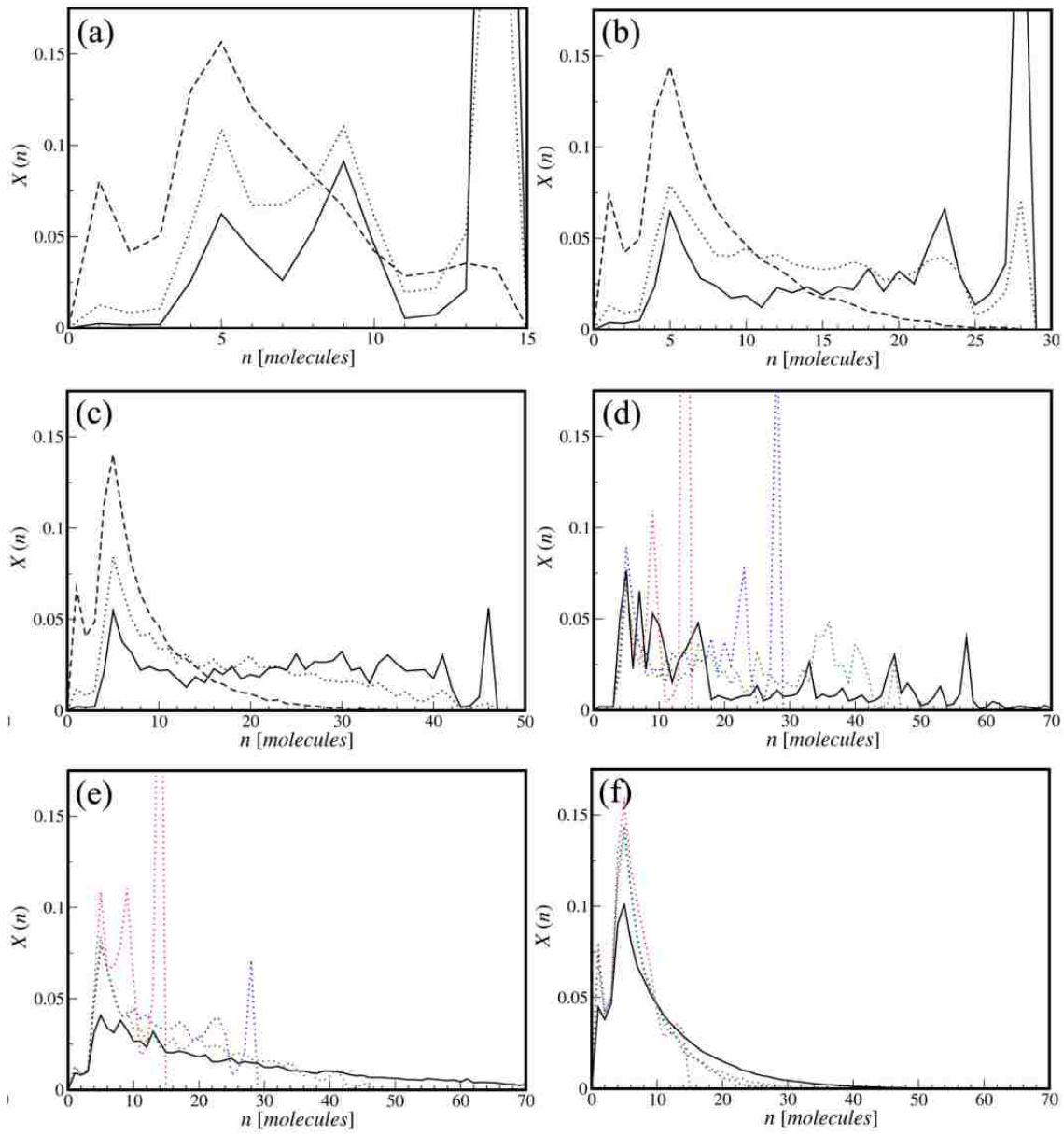

Figure 3.9. (Panels a-c: constant cluster size per panel) Fraction of molecules in a hydrogen bonded *n*-aggregate at 235 K (solid line), 280 K (dotted line), and 340 K (dashed line) for (a) 14-molecule cluster [not shown ($X(n)$ = 0.614 at 235 K) and ($X(n)$ = 0.327 at 280 K)], (b) 28-molecule cluster [not shown ($X(n)$ = 0.303 at 235 K)], and (c) 46-molecule cluster. (Panels d-f: constant temperature per panel) Fraction of molecules in a hydrogen bonded *n*-aggregate for 500-molecule *NpT* (bulk phase) simulations (black), and for 14-molecule cluster (red), 28-molecule cluster (blue), and 46-molecule cluster (green) at (d) 235 K [not shown (n = 14, $X(n)$ = 0.614) and (n = 28, $X(n)$ = 0.303)] , (e) 280 K [not shown (n = 14, $X(n)$ =0.327)], and (f) 340K.

by all cluster sizes at various temperatures may be an issue on the applicability of using equation 2.33 in extrapolating bulk properties especially the surface tension.

3.4 Concluding Remarks

We conclude that due to CNT's positive work of formation for the monomer that leads to an overestimation of the ΔG^*_{CNT}, ln (J_{SIM} / J_{CNT}) or the differences between the free energy barrier heights between CNT and simulations, (ΔG^*_{CNT} - ΔG^*_{SIM}) / $k_B T$, are always positive. As a consequence, experimental results having negative ln (J_{EXP} / J_{CNT}) are likely incorrect. Moreover, our results strongly support the correctness of experimental results that show a positive slope of the nucleation rate ratio with inverse temperature. This trend is mainly caused by the lower surface tensions at higher temperatures. On the molecular level, near-critical clusters of 1-pentanol molecules are compact but contain multiple hydrogen bonded aggregates and the corresponding aggregate size distribution depends strongly on temperature and also on the overall size of the cluster system. Finally, we suggest that linear interpretation from CNT (equation 2.33) should be used with caution. For 1-pentanol, we suggest that quantities needed for CNT predictions should be obtained from bulk phase simulations. Finally, the use of polarizable force field in bulk-phase simulation is encouraged since TraPPE-UA force field most likely overestimates the binding energy for the dimer and trimer.

Chapter 4. Probing the Nucleation Mechanism for the Binary *n*-Nonane/1-Alcohol Series with Atomistic Simulations[P1]

4.1 Introduction

Here the AVUS−HR approach[39] was extended to multicomponent nucleation systems. It was applied to investigate the homogeneous vapor−liquid nucleation for the binary *n*-nonane/1-alcohol series, including *n*-nonane/methanol, *n*-nonane/ethanol, *n*-nonane/1-propanol, *n*-nonane/1-butanol, *n*-nonane/1-hexanol, and *n*-nonane/1-decanol. This study was partly initiated by a previous simulation on *n*-nonane/ethanol, for which a striking discovery of a multiple pathway mechanism was interpreted from the calculated nucleation free energy (NFE) profile.[52] These systems, the *n*-nonane/1-alcohol series, were chosen to specifically examine how the nucleation behavior would evolve when the system approaches the macroscopic miscibility gap. It is well-known that the miscibility between *n*-nonane and 1-alcohol slowly changes with the chain length of the alcohol. In fact, *n*-nonane and methanol already exhibit a miscibility gap at the nucleation condition considered here. Moreover, this study was inspired by the experimental results obtained by Viisanen and coworkers.[91] In particular, they discovered an unusual type of non-ideal nucleation behavior for this binary series compared to other non-ideal binary systems (such as water/ethanol) that they examined before. Normally, for macroscopically miscible fluids, the nucleation rate is expected to increase with the addition of the second component. However, for the *n*-nonane/alcohol systems, the nucleation rate was found to remain relatively undisturbed with the addition of the second component, even when the normalized activity of the second component is more than half of the first component in some cases. This behavior seems

to resemble the water/*n*-nonane system, an immiscible mixture in both macroscopic and microscopic lengths,[38] which questions whether *n*-nonane and alcohol conucleate. Furthermore, such tendency to demix is in sharp contrast to the macroscopic miscibility known for most of these mixtures. The reluctant nucleation is even present, although less severe, in the *n*-nonane/1-hexanol system (1-hexanol is the longest alcohol molecule studied by them). In addition, they raised an open question on the possible orientation of OH groups of the alcohol molecules.

4.2 Simulation Details

4.2.1 Molecular Models

For simplicity, all calculations were done using the TraPPE-UA (Transferable Potentials for Phase Equilibria-United Atom) force field.[56, 113] This force field yields both single and multicomponent phase diagrams that are in good agreement with the experimental data.[56, 81, 113, 114] Previous simulations on single-component nucleation of *n*-heptane using the TraPPE-UA force field have shown that this force field overestimates the nucleation rate by a few orders of magnitude (or less than 10 $k_B T$ in terms of NFE barrier heights).[37] However, nucleation properties are extremely sensitive to molecular interactions.[39] Although quantitative comparison to experiments is still deemed as a challenge to molecular simulation for properties such as nucleation rates, previous simulations using this force field have shown that it was able to reproduce the non-ideal nucleation behavior observed for such non-ideal binary systems.[38,52]

4.2.2 Nucleation Free Energy (NFE) Calculations

For computational efficiency, all simulations were carried out using the grand-canonical version of the nucleation algorithm,[36] where the interactions between the cluster and the gas phase are neglected. As demonstrated previously, this approximation is acceptable in the low-temperature and low-density cases where these interactions are negligible.[37] Since *n*-alkane and

1-alcohol are chain molecules, an energy-based Stillinger-type cluster criterion was used, in which a cluster is defined as a group of molecules in which every molecule has at least one neighbor in the group with an interaction energy less than U_{cl}. Based on previous knowledge of these systems, a U_{cl} of −260 K (or any value close in magnitude to the simulation temperature) was chosen for all pairs of like molecules, whereas a U_{cl} of −120 K was used for all pairs of unlike molecules. It has been shown previously that the NFE results are relatively insensitive to the choice of the cutoff criterion.[37-39]

The HR technique combined with high-temperature simulations was applied to facilitate the convergence of the NFE data. Simulations were initially carried out at T = 300 K where relatively short simulation runs ($O(10^8)$ Monte Carlo moves) were used in the iterations for the convergence of the NFEs or the biasing potential. Once the NFEs (or the biasing potential) have been converged for clusters of all sizes of interest, a simulation run consisting of 10^9 Monte Carlo moves is used to obtain the DOS histograms (using equation 2.39 with a bin width of $20k_B$ K). From these histograms, the NFE results were extrapolated at a temperature lower by about 30 K using equations 2.40 and 2.41. These extrapolated NFE results served as an initial guess for constructing the biasing potentials for simulations at this lower temperature. They were further smoothed through a couple of quick iterations, followed by a longer production run where the DOS histograms were calculated again for another extrapolation of the NFE results at an even lower temperature. This iterative extrapolation procedure was continued (usually one more time) until the NFE results were obtained at the temperature where the experiments were carried out, 230 K. It should be noted that the simulation length needs to increase gradually with the decrease in the temperature to compensate for the loss of the acceptance rate on the AVBMC swaps. This was achieved by using multiple independent simulations (as many as 32 for the lowest

temperature 230 K) that ran in parallel on different processors, a natural parallelization scheme in Monte Carlo. Since each of them started from a different configuration, this strategy also helps to ensure the sampling of clusters of all sizes/compositions of interest. All pair interactions (including both LJ and Coulombic) were included in the computation of the total energy of the cluster. The type of Monte Carlo move was selected at random according to the following probabilities: particle insertion (20%), particle deletion (20%), conformational changes using CBMC (10%), translation (25%), and rotation (25%). These moves were equally shared between the two molecular types present in the binary mixtures except for the AVBMC-enhanced particle insertion/deletion moves. Because a much higher acceptance rate (by about an order of magnitude) was observed for the AVBMC moves on *n*-nonane relative to that on alcohol molecules, 90% of the AVBMC moves were performed on alcohol, and the rest (10%) were performed on *n*-nonane to enable a comparable number of swap moves accepted for both types of molecules.

4.2.3 Determination of Onset Activities

Experimentally, the onset activities (a_i) are the gas phase activities needed to observe a predetermined fixed nucleation rate.[68, 91] Here, a constant nucleation barrier height was used to construct the onset activity plots, similar to previous simulation studies.[38,52] Although the conversion between the nucleation barrier and the nucleation rate requires the knowledge of an additional preexponential factor, this kinetic factor depends only weakly on the vapor-phase activities. Following a previous analysis performed on the *n*-nonane/ethanol system, a combined nucleation barrier was employed, which allows one to account for the contributions from more than one nucleation pathway present on the NFE map. In the calculations of this combined barrier, the NFE profiles (two-dimensional diagrams originally plotted as a function of the

numbers of molecules for the two components) were projected onto a single coordinate, the combined size of the cluster. Thus, for a cluster with a total size of *n*, its free energy formation is calculated as follows:

$$\exp[-\Delta G^{tot}(n)/\,k_B T] \;=\; \sum_{n_1=0}^{n} \exp[-\Delta G(n_1, n-\,n_1)/\,k_B T] \tag{4.1}$$

With this one-dimensional plot, the determination of the barrier height and critical cluster size is straightforward (similar to single-component nucleation). A value of around 50.64 $k_B T$ for the barrier height, which corresponds to a concentration of 100 droplets/cm^3 for the critical nuclei, was chosen to plot the onset activities for our simulation. For both *n*-nonane and ethanol, this critical cluster concentration is about to yield a nucleation rate of 10^7 droplets/cm^3/s, based on the following classical expression[115] for the nucleation rate, *J*, for single-component systems in terms of the critical cluster concentration ρ_{n^*}:

$$J = \frac{\rho_{vap}^2}{\rho_{liq} S}\left(\frac{2\gamma}{\pi m}\right)^{1/2} \exp(-\beta \Delta G^*) = \frac{\rho_{vap}}{\rho_{liq} S}\left(\frac{2\gamma}{\pi m}\right)^{1/2} \rho_{n^*} = J_0 \rho_{n^*} \tag{4.2}$$

where ρ_{vap} and ρ_{liq} are the densities of the supersaturated vapor and the liquid phase at coexistence, respectively, *S* is the supersaturation, γ is the surface tension, *m* is the molecular mass, and ΔG^* is the nucleation barrier height (relative to the monomer's free energy). The term $\rho_{vap}/(\rho_{liq} S)$ can be approximated by the ratio of the saturated vapor-phase density to the liquid-phase density. Using the experimental coexistence densities, J_0 is estimated to be around $O(10^5)$ s^{-1} for both *n*-nonane and ethanol at 230 K.

4.3 Results and Discussions

4.3.1 Nucleation Free Energy (NFE) Contour Maps

Plotted in Figure 4.1-4.3 are the contours of the two-dimensional NFEs as a function of the number of *n*-nonane and alcohol molecules calculated for the various *n*-nonane/alcohol systems at a composition condition when both species contribute roughly equally to the nucleation event.

For comparison, the NFE contours obtained previously[52] for the *n*-nonane/water and water/ethanol systems were also plotted in Figure 4.3. It is clear from this figure that the binary *n*-nonane/1-alcohol nucleation systems exhibit rather unique mechanistic features that are distinct from the *n*-nonane/water and water/ethanol systems. Most noticeable is the widely open saddle point region that appears to stretch from the *n*-nonane-enriched domain to the alcohol-enriched domain. This is an indication that, for the *n*-nonane/1-alcohol systems, nucleation could proceed through multiple channels compared to the one or two noticed for the other binary systems. This feature is particularly prominent for those systems involving medium-length alcohols, such as ethanol, 1-propanol, and 1-butanol. In addition, by monitoring how this feature dissipates towards the two ends (either to the shortest alcohol (methanol) or to longer alcohols, such as 1-hexanol and 1-decanol), it is tempting to conclude that the appearance of this elongated saddle point region arises from a nearly perfect balance between the tendency to mix and the tendency to demix among the *n*-nonane and the alcohol molecules. For example, the rising of an island at the center of the saddle point region, as noted for the *n*-nonane/methanol system, is clearly a sign of demixing on a microscopic length between these two species, which is consistent with the macroscopic miscibility gap known for this mixture. This island apparently separates the saddle point region into two parts, which leads to a two-pathway type of nucleation map, resembling, to some extent, the one found for the *n*-nonane/water mixture. At the other end, the NFE maps for both *n*-nonane/1-hexanol and *n*-nonane/1-decanol systems display a more normal type of shape with the central part sunk (instead of rising, as compared to *n*-nonane/methanol) to become a "true" saddle point, although it is still elongated but to a lesser degree. This points to an enhanced mixing behavior between *n*-nonane and longer alcohol molecules (consistent with their better macroscopic miscibility), namely, the formation of a

mixed critical nucleus is now more preferable than forming two types of phase-separated critical nuclei, similar to water/ethanol. On the other hand, for binary mixtures involving medium-length alcohols from ethanol to 1-butanol, the appearance of a highly elongated saddle point region is a result of a roughly equal probability of forming critical nuclei of all compositions (balanced by their tendencies to mix and demix). Another distinct feature for the *n*-nonane/alcohol systems is the appearance of the ellipsoidal island, mainly due to the formation of stable hydrogen-bonded alcohol complexes (i.e., cyclic pentamers).

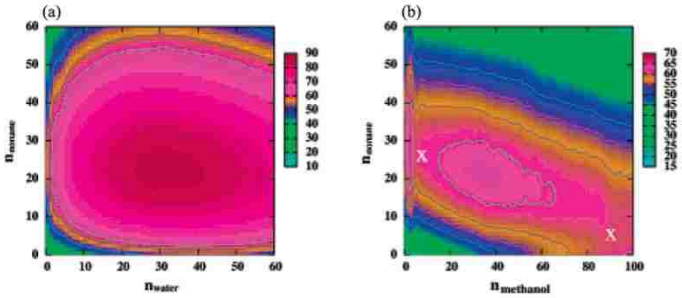

Figure 4.1. Contour of the two-dimensional NFEs (in units of k_BT) as a function of the number of molecules for the two components involved in each binary mixture calculated from the simulation at (a) $n_v^{nonane} = 1.71 \times 10^{-7}$ Å^{-3} and $n_v^{water} = 4.36 \times 10^{-8}$ Å^{-3}; and (b) $n_v^{nonane} = 1.34 \times 10^{-7}$ Å^{-3} and $n_v^{methanol} = 8.11 \times 10^{-8}$ Å^{-3}.The crosses represent saddle points. For the binary *n*-nonane/water system, nucleation proceeds along the two axes (either via pure *n*-nonane or via pure water). For clarity, the contour levels with NFE values of 50, 54, 58, and 62 k_BT are depicted explicitly as lines.

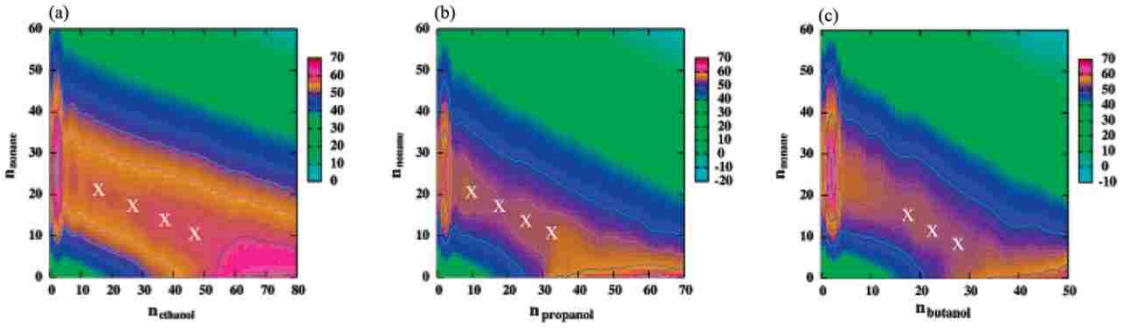

Figure 4.2. Contour of the two – dimensional NFEs (in units of k_BT) as a function of the number of molecules for the two components involved in each binary mixture calculated from the simulation at (a) $n_v^{nonane} = 1.45 \times 10^{-7}$ Å^{-3} and $n_v^{ethanol} = 3.83 \times 10^{-8}$ Å^{-3}; (b) $n_v^{nonane} = 1.58 \times 10^{-7}$ Å^{-3} and $n_v^{1\text{-propanol}} = 1.41 \times 10^{-8}$ Å^{-3}; and (c) $n_v^{nonane} = 1.45 \times 10^{-7}$ Å^{-3} and $n_v^{1\text{-butanol}} = 5.71 \times 10^{-9}$ Å^{-3}. Crosses and counter levels are the same as in Figure 4.1.

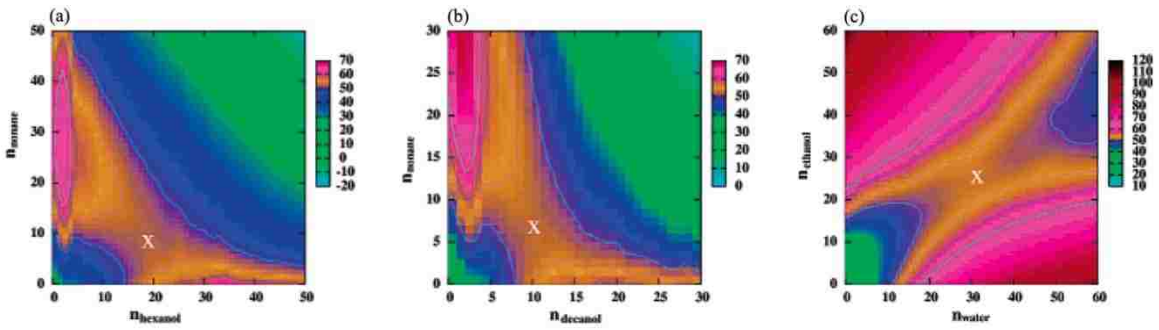

Figure 4.3. Contour of the two-dimensional NFEs (in units of k_BT) as a function of the number of molecules for the two components involved in each binary mixture calculated from the simulation at (a) $n_v^{\text{nonane}} = 1.26 \times 10^{-7}$ Å^{-3} and $n_v^{\text{1-hexanol}} = 6.87 \times 10^{-10}$ Å^{-3}; (b) $n_v^{\text{nonane}} = 1.11 \times 10^{-7}$ Å^{-3} and $n_v^{\text{1-decanol}} = 2.34 \times 10^{-11}$ Å^{-3}; and (h) $n_v^{\text{ethanol}} = 1.61 \times 10^{-8}$ Å^{-3} and $n_v^{\text{water}} = 1.71 \times 10^{-8}$ Å^{-3}. Crosses and counter levels are the same as in Figure 4.1.

The NFE maps shown in Figure 4.1-4.3 detail a rather subtle evolution of the miscibility between *n*-nonane and 1-alcohol with the increase in the alcohol chain length. This small-length scale information seems to parallel well with the available macroscopic miscibility data between these two species. Experimentally, methanol and *n*-nonane were shown to have a miscibility gap already at room temperature. Ethanol is fully miscible with *n*-nonane at room temperature but will approach a miscibility gap at lower temperatures.[91] With further increase of the alcohol chain length, an increasingly better miscibility with *n*-nonane is expected on a macroscopic length scale. Similarly, this trend was also observed for clusters on a much smaller length scale. Furthermore, this systematic study on the homogeneous nucleation of the homologous *n*-nonane/1-alcohol series reveals an interesting finding on how nucleation behaves when the system approaches the macroscopic miscibility gap. Namely, the nucleation event switches from a single-pathway mechanism (as observed for *n*-nonane/1-hexanol) to a two-pathway one (for *n*-nonane/methanol), while between it adopts a multi-pathway mechanism (for binary mixtures involving medium-length alcohols). Such a mechanistic switch was, to some extent, already

captured by previous theoretical studies[26, 28, 31, 53, 54] employing relatively simple models, such as Lennard-Jonesium (LJ). For example, in the simulation study carried out by ten Wolde and Frenkel[31] on binary LJ mixtures, it was found that nucleation proceeds via a single type of critical nuclei for fully miscible systems. For mixtures with a miscibility gap, nucleation could still proceed via a mixed nucleus but become more likely to adopt a two-pathway mechanism for larger cluster sizes or when their demixing tendency is enhanced through the change of the mixing parameter. In addition, they found that a regime exists for partially miscible mixtures, where the critical nuclei seem to be miscible in all proportions.

Although this mechanistic switch has been qualitatively reproduced by the early studies, the relatively simple LJ models employed therein did not allow direct, quantitative comparison with the experiments, especially considering that neither chain molecules nor the orientationally dependent hydrogen-bond interactions (involved by alcohols) can be sufficiently described via the use of a spherical LJ bead.[37] A benefit of using realistic, atom-based models (that were previously parametrized to experimentally known thermodynamic properties, such as phase equilibrium data) is that such models allow for a side-by-side comparison to the experimental nucleation data for various systems. This comparison is important, as some of the NFE maps obtained have challenged the theory with respect to whether a simplistic view of the nucleation process holds for all systems. In particular, those maps that show the coexistence of multiple nucleation channels are directly at odds with a fundamental assumption employed by the theory, that is, nucleation proceeds on a well-defined path via the formation of a critical nucleus with a well-defined structure and composition, upon which the theoretical formalism of the nucleation rate can be derived.[21-24, 91] Thus, it needs to be verified that these contour plots are actually consistent with the non-ideal nucleation behavior observed experimentally for these systems.

4.3.2 Plots of the Onset Activities

The various combinations of onset activities for the vapor-liquid nucleation of the different *n*-nonane/1-alcohol mixtures, including *n*-nonane/ethanol, *n*-nonane/1-hexanol, and *n*-nonane/1-decanol are shown in Figure 4.4.[40] These onset activities are normalized by the activities of neat *n*-nonane and neat 1-alcohol vapors and correspond either to a constant nucleation rate of 10^7 droplets/cm^3/s, as measured experimentally, or to a combined nucleation barrier height of around 50.64 k_BT, as calculated from the simulations (see section 4.2.3). For comparison, the onset activity data obtained previously for the *n*-nonane/water and water/ethanol systems[52] as well as the available experimental data[47, 115, 116] for these systems, are also plotted in Figure 4.4. It should be noted that the use of this combined barrier (see equation 4.1) naturally takes into account an important factor unique for these mixtures, namely, the size of the saddle – point region, since, in general, the larger this area, the greater the number of nucleation

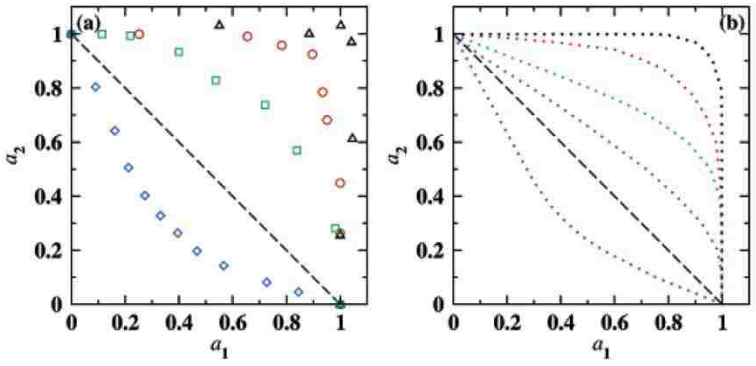

Figure 4.4. Plots of reduced onset activities. In the left panel are the experimental data[47, 91, 117] for binary *n*-nonane/ethanol, *n*-nonane/1-hexanol, *n*-nonane/water, and water/ethanol mixtures at a constant nucleation rate of 10^7 droplets/cm^3/s. Simulation counterparts (right panel) were drawn using dotted lines. The colors black, red, green, purple, and blue represent *n*-nonane/water, *n*-nonane/ethanol, *n*-nonane/1-hexanol, *n*-nonane/1-decanol, and water/ethanol, respectively. The ideal case would correspond to the dashed straight line. For binary systems involving *n*-nonane, a_1 refers to the *n*-nonane vapor phase activity and a_2 for the other component. For water/ethanol, a_1 and a_2 are the water and ethanol vapor phase activity, respectively.

pathways, and the higher the nucleation rate. As is evident from this figure, both the experimental and simulation data show that nucleation of the *n*-nonane/1-alcohol occurs at much higher activities than expected for an ideal mixture, for which the reduced onset activities simply fall on a straight line and sum to unity. These higher onset activities signal a reluctant co-nucleation between *n*-nonane and 1-alcohols, which becomes more apparent if one compares these data to those for the *n*-nonane/water mixture, in which nucleation proceeds through a two-pathway mechanism (one via an *n*-nonane-enriched nucleus and the other via a water-enriched nucleus; see the NFE map shown in Figure 4.1 - 4.3). In addition, the simulation data semi-quantitatively reproduce the experimentally observed chain-length dependency of this non-ideal behavior; that is, the reduced onset activities lower gradually with the increase in the alcohol chain length and approach those for the ideal mixtures, although appreciable deviation from the ideal behavior is observed even for *n*-nonane/1-decanol, the longest alcohol investigated here. This evidence of increasing tendency to conucleate for longer alcohols with *n*-nonane is expected in view of their enhanced miscibility with each other, both macroscopically and microscopically. In sharp contrast, another fully miscible mixture, water/ethanol, shows an opposite behavior, with the onset activities curved to the other side, which was interpreted previously as a sign of mutual nucleation enhancement by both experiments[47] and the simulations.[55, 56]

4.3.3 Molecular Content of Nuclei

The increasing non-ideality of the *n*-nonane/1-alcohol mixtures with the decreasing alcohol chain length is also evident from the composition diagrams for the critical nuclei shown in Figure 4.5.[40] The composition for the critical nuclei was calculated through averaging the composition of all clusters with the critical cluster size weighted by their corresponding probability densities. Again, a very good agreement was found between the experiments and

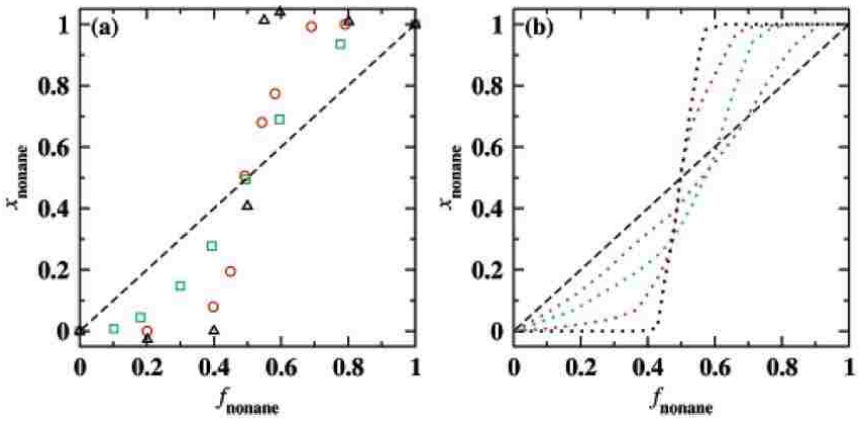

Figure 4.5. Average mole fraction of *n*-nonane in the critical nuclei as a function of the normalized activity fraction of *n*-nonane. Symbols and panels are the same as those in Figure 4.4.

the simulations, with both showing that the composition of the critical nuclei evolves in a nonlinear way as a function of the normalized activity fraction, $f_{nonane} = (a_{nonane} / a^0_{nonane}) / (a_{alcohol} / a^0_{alcohol} + a_{nonane} / a^0_{nonane})$. The sigmoidal shape of these plots is a sign of a depletion of alcohol at low alcohol activity or a depletion of *n*-nonane at low *n*-nonane activity, providing additional evidence of the reluctant conucleation between these two species. The good agreement between the experiments and the simulations also seems to support the applicability of using the nucleation theorem[47-50] in the experimental interpretation of the content of the critical nuclei (i.e., determined from the slopes of the nucleation rate surface). However, it should be noted that this averaged molecular content, a single number, belies the miscibility information and the fact that a wide range of compositions could be present for the critical nuclei, as already indicated from the NFE contours shown in Figure 4.1 – 4.3. Therefore, it would be misleading to use this average content of the critical nuclei to locate the true saddle point in the nucleation pathway. For example, in the case of an *n*-nonane/water mixture, an *n*-nonane mole fraction of close to 0.5 obtained at an f_{nonane} of 0.5 cannot be interpreted as the formation of a single mixed critical

nucleus with equal molar amounts of the two components involved. Rather, this value appears to accidentally arise from the formation of two major critical nuclei, one *n*-nonane-enriched and the other water-enriched.

The same behavior may be expected for the *n*-nonane/1-alcohol systems. The situation becomes even more complicated because the critical nuclei were found to be miscible in all proportions for these cases. Fortunately, the simulations described here sample the entire spectrum of clusters (i.e., clusters of different sizes and all possible compositions), and thus allow a quantitative elaboration of these microscopic details. Plotted in Figure 4.6[40] are the density distributions for the critical cluster nuclei as a function of the composition at a normalized *n*-nonane activity fraction of 0.5. As expected, this plot switches from a concave shape for *n*-nonane/methanol to a convex shape for *n*-nonane/1-decanol, while between it is relatively more flat for *n*-nonane/ethanol (also for *n*-nonane/1-propanol and *n*-nonane/1-butanol, which were not shown here for clarity purposes). The concave shape with a dip centered around a δ ($= n_{\text{nonane}} - n_{\text{alcohol}}$) value of zero is a clear indication of demixing or a two – pathway nucleation mechanism that mimics the *n*-nonane/water system. Even for *n*-nonane/ethanol, the flat region seems to be dipped slightly in the middle, implying that a full miscibility remains unfavorable, despite the fact that the mole fraction of ethanol averaged over all the critical nuclei is close to 0.5 at this condition. On the other hand, the convex shape observed for longer alcohols with a maximum centered around the average nuclei composition signals an enhanced miscibility and a tendency to adopt a single – pathway nucleation mechanism. Such an evidence of enhanced miscibility even extends to small clusters with a few molecules (see Figure 4.7).[40] However, irrespective of the alcohol chain length, clusters with a molecular content of around two alcohols are discouraged for all sizes. This is consistent with the ellipsoidal island present on

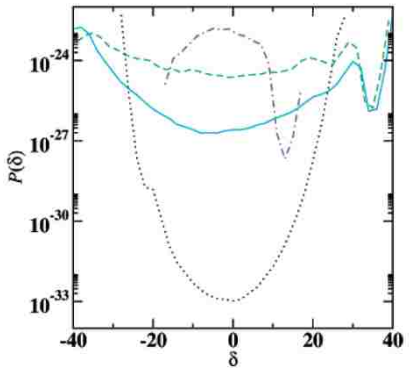

Figure 4.6. Probability density (expressed as an absolute concentration) of the critical cluster nuclei as a function of $\delta = n_{\text{nonane}} - n_{\text{alcohol}}$ for the nucleation of *n*-nonane/methanol (cyan solid), *n*-nonane/ethanol (green dashed), *n*-nonane/1-decanol (purple dashed – dotted), and *n*-nonane/water (black dotted) at a normalized *n*-nonane activity fraction of 0.5 with a combined nucleation barrier height of 50.64 $k_B T$.

the NFE contour maps shown in Figure 4.1 – 4.3. Both indicate that the initial mixing of alcohols with *n*-nonane needs to pass through this unfavorable phase (i.e., formation of alcohol dimers).

4.3.4 Microscopic Structures of Clusters

From visual inspection of the cluster configurations (see Figure 4.8),[40] it is immediately clear that, inside these clusters, there is another layer of microheterogeneity (apart from the major type of heterogeneity due to the presence of a wide spectrum of clusters), which arises from the aggregation of alcohol molecules through hydrogen – bonding interactions.[104, 105] In fact, this aggregation leads to an internal "microphase separation" (see Figure 4.8).[40] This feature is more prominent for systems involving shorter alcohols (such as methanol and ethanol) where the clusters typically exhibit a core/shell shape structure in which the hydrogen – bond aggregates attempt to wrap around the nonpolar core formed by the *n*-nonane molecules (see Figure 4.8c). Occasionally, these small aggregates further cluster together and form one large hydrogen – bond aggregate that leads to a fully phase – separated structure (see Figure 4.8b), resembling, to some extent, the double – layer structure observed for the *n*-nonane/water mixture

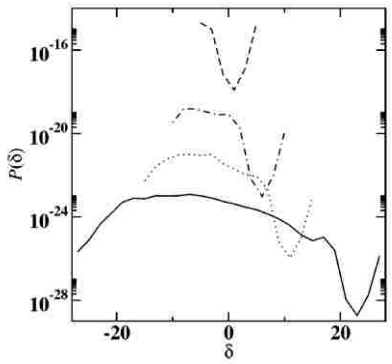

Figure 4.7. Probability density of the critical cluster (solid) and the precritical clusters containing 5 (dashed), 10 (dashed−dotted), and 15 (dotted) molecules as a function of $\delta = n_{\text{nonane}} - n_{\text{1-hexanol}}$ for nucleation of the binary *n*-nonane/1-hexanol system at a normalized *n*-nonane activity fraction of 0.5 with a combined nucleation barrier height of 50.64 $k_B T$.

(see Figure 4.8a). On the contrary, as the hydrophobic chain length of the alcohol component increases, the hydrogen – bond aggregates tend to disperse inside the nonpolar domain formed by the *n*-nonane molecules (see Figure 4.8d – f). For longer alcohols, the alkyl tails can be preferentially solvated by *n*-nonane, which is the microscopic origin for the enhanced miscibility between these two species. Analysis of radial density profiles of mixed clusters containing a roughly equal number (20 ± 2) of *n*-nonane and 1-alcohol molecules also supported this picture (see Figure 4.9).[40] For systems involving shorter alcohols (i.e., methanol or ethanol), there is a noticeable enrichment of the alcohol oxygen and hydrogen densities toward the surface, which is consistent with the core/shell structure pattern shown above. In contrast, for the *n*-nonane/1-hexanol system, the 1-hexanol oxygen and hydrogen density profiles shift substantially toward the center of the cluster, leading to an interior enrichment of the 1-hexanol carbon densities accompanied by a depletion of the *n*-nonane carbon densities.

Clearly, the formation of hydrogen – bond aggregates is the most important structural motif for clusters involving polar alcohol molecules. We further analyzed the distribution of the alcohol molecules over the aggregate size. In this analysis, a simple distance cutoff ($r_{OO} < 3.3$

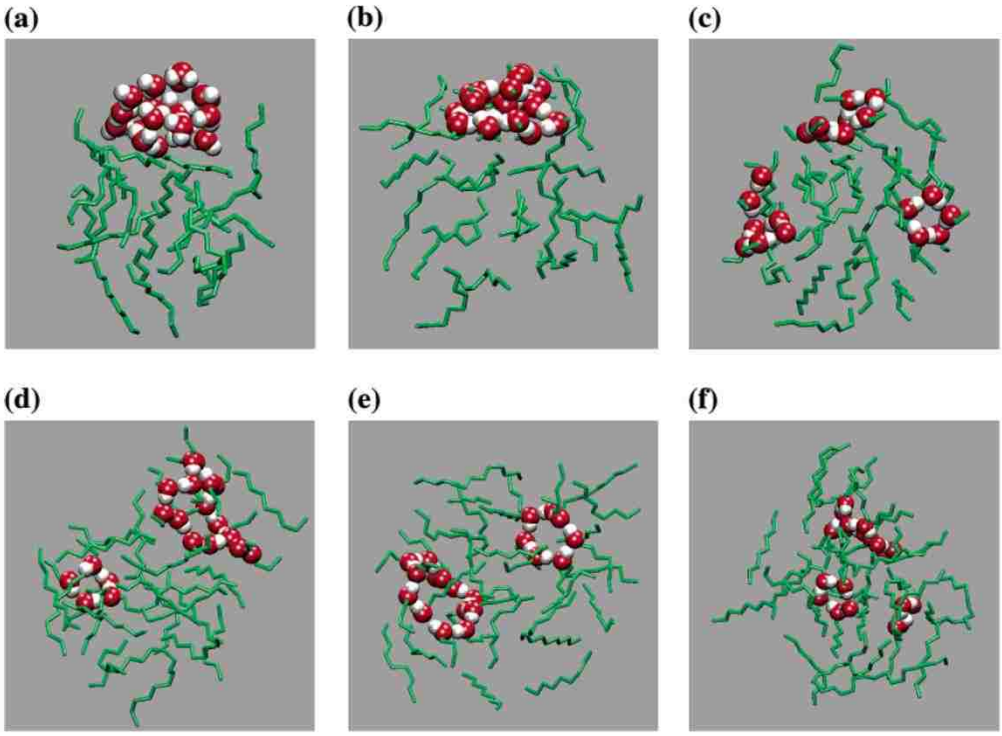

Figure 4.8. Representative snapshots of clusters (consisting of 20 *n*-nonane and 20 alcohol or water molecules) obtained at T = 230 K for (a) *n*-nonane/water, (b) *n*-nonane/methanol, (c) *n*-nonane/ethanol, (d) *n*-nonane/1-propanol, (e) *n*-nonane/1-butanol, and (f) *n*-nonane/1-hexanol. Oxygens and hydrogens are shown as a sphere in red and white, respectively. A stick representation is used for the alkyl tails.

Å)[118] was used to determine whether two alcohol molecules belong to the same hydrogen – bonded aggregate. The results were plotted in Figure 4.10.[40] The overall distribution looks quite similar between the different alcohols studied here. In particular, a majority of these hydrogen – bonded aggregates consist of four to eight alcohol molecules with five as the most probable number. This is consistent with those representative snapshots and with the aforementioned presence of an ellipsoidal island on the NFE maps. In addition, the distribution is rather broad, which seems to suggest that a very diverse spectrum of hydrogen – bonded aggregates is present inside these clusters. All these features already resemble those reported previously for the bulk alcohol phases.[106, 118]

4.3.5 Further Discussions

From the detailed microscopic insights presented above, it is now clear that *n*-nonane and alcohol nucleate together under certain conditions by forming clusters containing both species. However, they mix with each other rather reluctantly. First, with a decrease in the alcohol chain length, we start to observe a trend of demixing with *n*-nonane, as evident from the concave shape exhibited by the composition diagram shown in Figure 4.6. This trend is consistent with the ultimate appearance of the macroscopic miscibility gap observed for the *n*-nonane/methanol mixture at this temperature. Second, even if they come together forming clusters, these two components tend to separate from each other microscopically because the polar OH groups of the alcohols will always point away from the nonpolar alkyl chains and bind to themselves through hydrogen bonds forming polar aggregates. For shorter alcohols, further clustering of these aggregates would take place, leading to entirely phase – separated structures, like the double – layered one observed for *n*-nonane/methanol and *n*-nonane/ethanol.

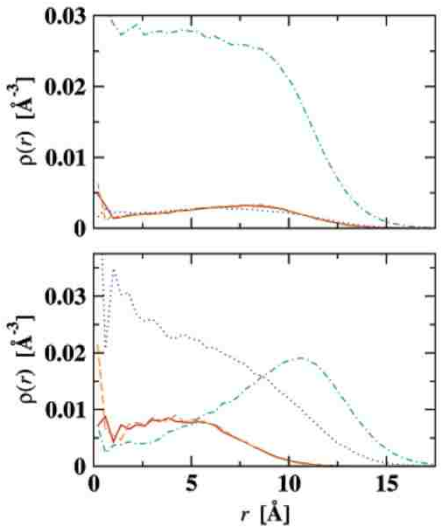

Figure 4.9. Radial density profiles for the *n*-nonane/methanol (top) and *n*-nonane/1-hexanol (bottom) systems averaged over clusters containing a roughly equal number (20 ± 2) of *n*-nonane and 1-alcohol molecules. The red solid, orange dashed, blue dotted, and green dashed – dotted lines represent the number density profiles for the alcohol oxygen atoms, the alcohol hydrogen atoms, the alcohol carbon atoms, and the *n*-nonane carbon atoms, respectively.

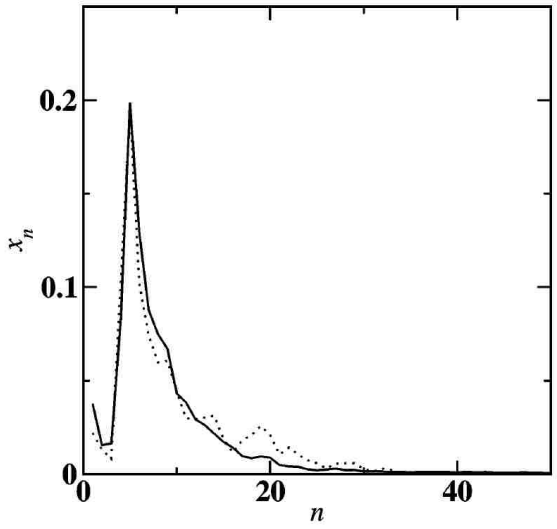

Figure 4.10. Distributions of 1-alcohol hydrogen – bonded aggregates with aggregation number *n* for *n*-nonane/methanol (solid) and *n*-nonane/1-hexanol (dotted) found in those clusters near the saddle – point region shown in Figure 4.1 and Figure 4.3, i.e., with an NFE value between 58 and 62 k_BT for *n*-nonane/methanol or between 50 and 54 k_BT for *n*-nonane/1-hexanol.

4.4 Concluding Remarks

In conclusion, the AVUS−HR approach was extended to multicomponent nucleation systems to allow calculation of the properties for binary vapor−liquid nucleation of *n*-nonane/methanol, *n*-nonane/ethanol, *n*-nonane/1-propanol, *n*-nonane/1-butanol, *n*-nonane/1-hexanol, and *n*-nonane/1-decanol mixtures at an ultralow temperature of 230 K. Using the TraPPE-UA force field, it was found that these simulations were able to reproduce the experimentally observed non-ideal nucleation behavior for this *n*-nonane/1-alcohol series, that is, a reluctant conucleation between them. In particular, with a decrease in the alcohol chain length, the onset activities were found to approach those for the *n*-nonane/water mixture (where independent nucleation was shown to take place), consistent with the experiments. Also, the calculated compositions on the critical nuclei agree with those interpreted from the slope of the experimental nucleation rate surface based on the nucleation theorem. Both indicate a reluctant mixing behavior between these two species, i.e., depletion of the alcohol at low alcohol activity

or depletion of *n*-nonane at low *n*-nonane activity. However, caution is needed when using the average content of the critical nuclei to identify the true saddle point in the nucleation pathway, as a wide range of compositions were found to be present for the critical nuclei at certain conditions for the *n*-nonane/1-alcohol systems. Additional analysis on composition and structure further confirmed this reluctant mixing/conucleation behavior. More importantly, the calculated NFE maps reveal an interesting mechanistic switch for this *n*-nonane/1-alcohol series when approaching the miscibility gap. Specifically, the nucleation mechanism evolves from a single-pathway type for *n*-nonane/hexanol to a somewhat two-pathway type for *n*-nonane/1-methanol. In contrast, for binary mixtures involving medium-length alcohols, the NFE maps display the most striking feature, with the saddle point stretched almost all the way from the *n*-nonane-enriched to the alcohol-enriched domain, implying that multiple pathways coexist on the nucleation map. These findings have challenged the theory with respect to whether a simplistic view of the nucleation process holds for all systems. In particular, those theoretical models based on the assumption that nucleation proceeds through the formation of mixed critical clusters with a certain well-defined composition would have to be modified accordingly for an accurate prediction of the nucleation rates for these systems.

Chapter 5. Ternary Nucleation

5.1 Dumbbells and Onions in Ternary Nucleation[P2]

Important models for atmospheric nucleation are mixtures of water, an alcohol, and/or an alkane. Viisanen and Strey[46] utilized a nucleation pulse chamber to measure accurately the homogenous vapor-liquid nucleation rates for the ternary water, *n*-nonane (oil), and 1-butanol (surfactant) system. Using the nucleation theorem one can extract the average critical cluster composition,[46, 48-50] but not the distribution of compounds within the cluster. Viisanen and Strey found that the critical nuclei (consisting of ~30 molecules) contain significant amounts of water, oil, and surfactant at intermediate vapor compositions, and speculated that clusters form an "onion-like" structure with a water-rich core and an oil-rich corona separated by a surfactant-rich interfacial shell.[46] The core/shell structures have been suggested as important motifs for explaining the high organic content of some aerosols as well as for the prebiotic environment needed for life development.[119-123] Another plausible structure would be a "dumbbell" where water-rich and oil-rich droplets are connected through a surfactant handle.

To resolve the structure of critical clusters for this ternary system, we employ the AVUS-HR Monte Carlo simulation approach[39, 40] that was recently developed by combining aggregation-volume-bias Monte Carlo (AVBMC),[55, 56] configurational-bias Monte Carlo (CBMC),[79-81] umbrella sampling (US), [58] and histogram reweighting (HR)[59-63]. The advantage of this method in studying rare nucleation events lies in its ability to overcome the large free energy barriers (or low probabilities for the occurrence of clusters near the critical nucleus size) through the use of US, and the inherent microheterogeneity of the phase space (*i.e.*, coexistence of

[P2]Reproduced by permission of the PCCP Owner Societies; http://www.rsc.org/ej/CP/2007/b705385a.pdf

clusters and monomers) by AVBMC. The incorporation of CBMC further enhances its efficiency and most importantly allows the use of realistic, atom-based force fields, thus enabling direct comparisons with the experiments.[36-40, 52] For example, in the simulations reported in this section, we employed the atom-based transferable force fields that have previously been shown to yield accurate descriptions for the binary nucleation of water/ethanol and water/*n*-nonane mixtures,[3] *i.e.*, TraPPE-UA models for *n*-nonane[81] and 1-butanol[106] and TIP4P for water[124].

Our simulations, the first atomistic characterization of an atmospheric ternary system, demonstrate that a very diverse set of nucleation mechanisms is present. Our definition of a_2' and a_3' here are the same as those of Viisanen and Strey[46] as shown below

$$a_2' = a_2 / (a_1 + a_2) \tag{5.1}$$

$$a_3' = a_3 / (a_1 + a_2 + a_3) \tag{5.2}$$

where a_1, a_2, and a_3 are the normalized onset activities for water, *n*-nonane, and 1-butanol, respectively. Looking at the vapor compositions with slightly more oil than water ($a_2' = 0.6$) over the full range of normalized surfactant activity fractions (a_3') at a temperature of 230 K, we obtained an excellent agreement between the simulation and the experiment[46] for the onset activity results (see Figure 5.1). In particular, both indicate a non-ideal nucleation behavior for this ternary mixture, with an interesting switch from a concave-up curvature at lower a_3' values to a concave-down curvature at higher a_3' values. While the former feature resembles that found for the *n*-nonane/alcohol system,[52, 116, 125] the latter is similar to the behavior found for the water/alcohol systems.[29, 38, 47, 52, 126-128] These two types of curvatures have been interpreted separately for those two groups of binary systems either as a sign of reluctant conucleation or a sign of mutual nucleation enhancement (see Chapter 4).[38, 52]

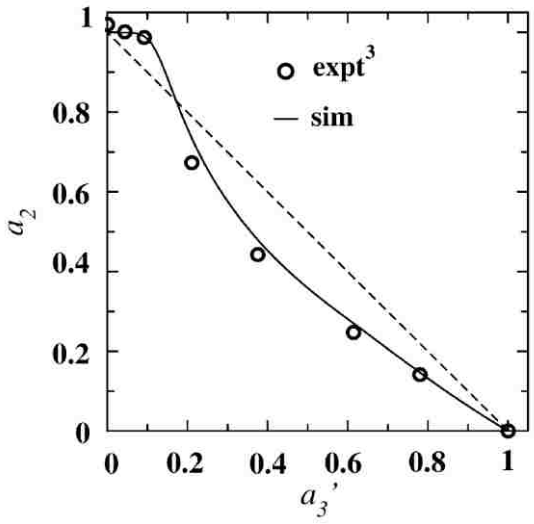

Figure 5.1. Plot of the reduced onset activities at a_2' = 0.6. While circles represent the experimental data[46] at a constant nucleation rate of 10^7 droplets cm^{-3} s^{-1}, the solid line depicts the simulation results at a constant nucleation barrier height of 50.64 k_BT. The dashed line is drawn as a guide to show the presence of the two types of curvatures and the location where they switch on the onset activity plot.

This excellent agreement also extends to the average composition of the critical clusters for this ternary system with both showing a similar, non-ideal evolution of this property as a function of the activity fraction (see Figure 5.2). Moreover, at an a_3' value of around 0.14 (near the switching point for the two types of curvatures found for the onset activity plot shown in Figure 5.1) both simulation and experiment indicate roughly equal contributions from all three components to the critical nuclei. It is tempting to suggest that 1-butanol works as a surfactant to bring the two incompatible components water and oil (*n*-nonane) together in a single cluster, our simulations reveal that critical nuclei with significantly different compositions are actually present at this particular vapor composition (see Figure 5.3). Thus, using only the average composition of the critical clusters one cannot distinguish between true conucleation involving mixed clusters and multi-pathway nucleation where critical clusters of different compositions are

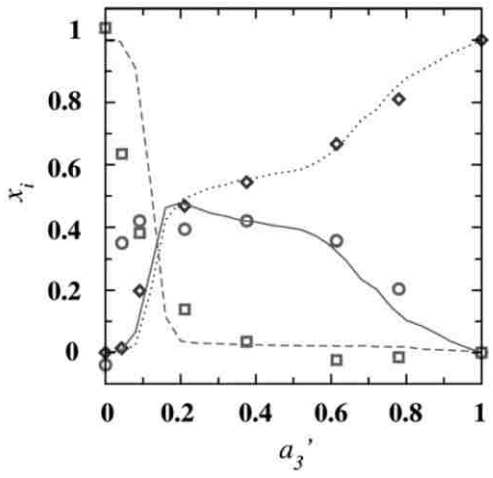

Figure 5.2. The average mole fraction of water (circles and solid line), *n*-nonane (squares and dashed line), and 1-butanol (diamonds and dotted line) found in critical nuclei at a_2' = 0.6 as a function of the normalized activity fraction a_3'. The symbols and lines denote the experimental data[46] and simulation results, respectively.

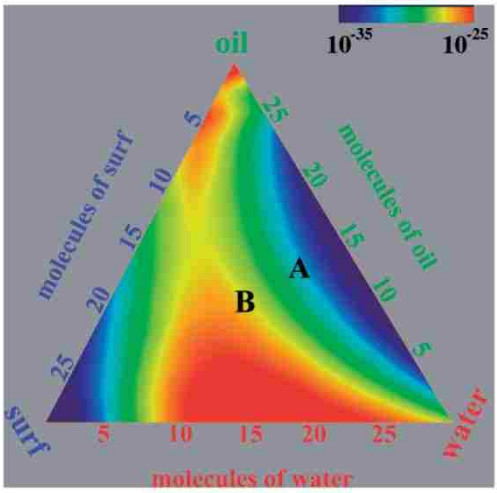

Figure 5.3. Probability density (absolute concentration in units of droplets $Å^{-3}$) of critical clusters as a function of cluster composition at a_2' = 0.6 and a_3' = 0.14, a condition when all three components contribute significantly to the critical clusters. A and B denote the compositions of the clusters shown in Figure 5.4.

found concomitantly.[26, 28, 31, 38, 52-54, 117, 129] Importantly, the simulations provide evidence for "dumbbell" and "onion" motifs (see Figure 5.4A and 5.4B). As indicated in Figure 5.3, "onion-type" structures are more likely than "dumbbells" at this vapor composition. If the number of surfactant molecules, n_{surf}, is too low, then oil and water nucleate independently.[38, 117, 129] For intermediate n_{surf}, the surfactants cannot cover the entire water droplet and aggregate on one side, leading to the formation of "dumbbells". The "onions" found here for $n_{surf} > 5$, are somewhat distorted with oil depositing mostly on one side, and surfactants with longer tails may be needed for the formation of more spherical structures, which may, in turn, lead to further improved conucleation between water and oil. As shown here, the computation of "nano-phase diagrams" (Figure 5.3) will allow one to determine optimal conditions for tailor-made nanoparticles.

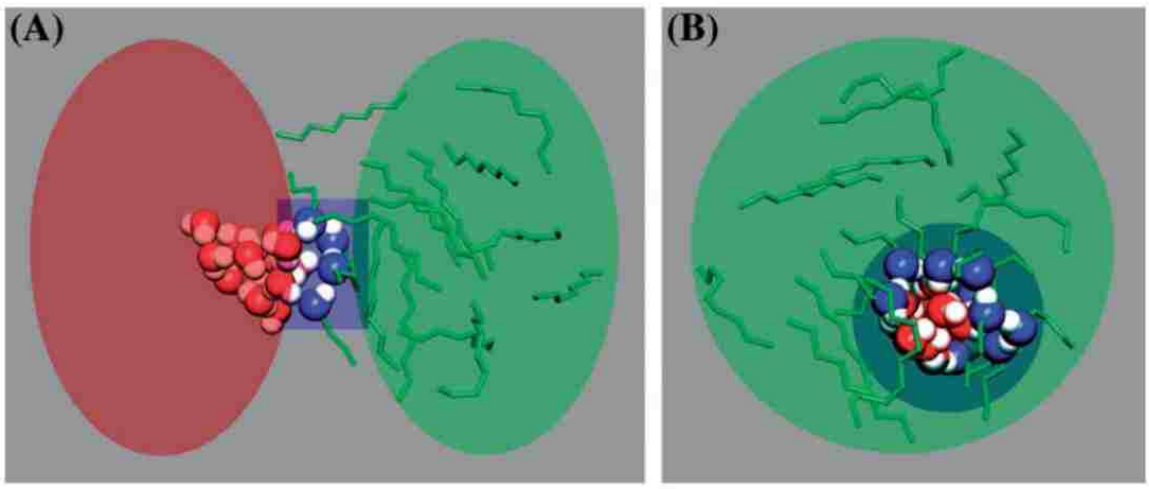

Figure 5.4. (A) Snapshot of a "dumbbell" critical cluster consisting of 13 water, 13 oil, and 4 surfactant molecules; (B) Snapshot of an "onion" critical cluster consisting of 10 water, 10 oil, and 10 surfactant molecules. Colour notation: water oxygen (red), butanol oxygen (blue), polar hydrogen (white), and alkyl tails (green).

5.2 Towards Understanding the Nucleation Mechanism for Multicomponent Systems: An Atomistic Simulation of the Ternary Nucleation of Water/*n*-Nonane/1-Butanol[P3]

5.2.1 Introduction

Following our previous success on the atomistic study of binary vapor-to-liquid nucleation events,[40, 52] we investigated the ternary nucleation of water/*n*-nonane/1-butanol mixture. Apart from being important model systems for atmospheric nucleation events, vapor mixtures that contain water, alcohol, and alkanes exhibit interesting non-ideal nucleation features.[46-48, 115-117, 125-129] This mixture, the ternary water/*n*-nonane/1-butanol nucleation system, has been previously reported by Viisanen and Strey[46] to display the most complex behavior reported to date. This was directly reflected by the onset activity results with a concurrent appearance of multiple distinct non-ideal characteristics, which implies that this system may take on various unique mechanisms (or pathways) during the nucleation process. Interest in this system was also driven by its relevance to microemulsion research. Water and *n*-nonane are known to be an immiscible pair, in both macroscopic and microscopic lengths, whereas 1-butanol, being an amphiphile, is fully miscible with either component in bulk phases and has the typical structural motifs for being a surfactant. Viisanen and Strey[46] attempted to address how the addition of this amphiphile could help improve the mutual miscibility between water and *n*-nonane. Through analysis of the average composition of critical clusters by applying the nucleation theorem (NT) to their experimental nucleation rate data, they found that at intermediate vapor compositions critical clusters contain significant amounts of each component. Viisanen and Strey interpreted this as a sign of enhanced miscibility and suggested that 1-butanol does this through an internally phase-separated cluster structure, which built upon the core (water) – shell (1-butanol) structure found for binary water/1-alcohol systems with *n*-nonane

[P3]Reproduced by permission of the PCCP Owner Societies; http://www.rsc.org/ej/CP/2008/b713189e.pdf

deposited outside forming an additional layer. A former simulation study carried out by us (see section 5.1)[51] has partly confirmed this structural speculation but also revealed a more complex miscibility behavior and nucleation mechanism than previously suggested for this system. Here, the entire range of vapor-phase composition conditions was investigated to acquire a detailed microscopic/mechanistic understanding for this ternary nucleation.

5.2.2 Simulation Details

For computational efficiency, all simulations in this section were carried out using the grand-canonical version of the nucleation algorithm,[36, 37] where the gas-phase chemical potential (or the corresponding gas-phase activity) is directly specified as part of the simulation conditions. In these calculations, the interactions between the cluster and the gas phase are neglected, which is acceptable for low-temperature and low-density cases.[37] This approximation also makes the configurational integral (or the Helmholtz free energy) of a cluster at any size *n* become independent of the chemical potential (or activity) of the gas-phase.[34, 36] Thus, the NFE values obtained at one gas phase activity *a* can be conveniently used to calculate those at any other condition *a*' as follows,

$$\Delta G_{a'}(n) = \Delta G_a(n) \; - nk_B T \ln \frac{a'}{a}. \tag{5.3}$$

Note that this equation differs slightly from that in reference 36 as the zero reference point for the NFE data reported here was set at a concentration of 1 droplet per $Å^3$ (that is, clusters with this concentration would have an NFE value of zero) so that the NFE values can be directly converted to absolute concentrations expressed in this unit. Equation 5.3 can be extended to a multicomponent form where the NFE data are expressed as function of the numbers of molecules for all components involved (n_i) and depend on the gas-phase activity of each component (a_i), *e.g.*, for a three component system, as follows,

$$\Delta G_{a_1', a_2', a_3'}(n_1, n_2, n_3) = \Delta G_{a_1,\ a_2,\ a_3}(n_1, n_2, n_3) - \sum_{i=1}^{3} n_i\, k_B T \ln \frac{a_i'}{a_i} \qquad (5.4)$$

Equations 5.3 and 5.4 greatly simplify our simulation task here as we only need to determine the NFE values directly from the simulations at one set of gas-phase activities and then apply these equations to map all the possible combinations of gas-phase activities that would yield similar barrier heights (or nucleation rates) for the construction of the onset activity plots.

Following the procedure in section 4.2.3 for binary nucleation systems,[40] the onset activities were determined by a constant combined nucleation barrier height of 50.64 $k_B T$. This barrier height corresponds to a critical cluster concentration of 10^{-22} droplets per $Å^3$ or 100 droplets per cm^3. For multicomponent systems, more than one nucleation pathway (or critical cluster) can be present on the NFE map. In order to account for the contributions from all possible pathways (critical nuclei), a combined nucleation barrier (or combined critical cluster concentration) was employed. In the calculation of this quantity, the NFE data, $\Delta G(n_1, n_2, n_3)$, or equivalently cluster concentration, $P(n_1, n_2, n_3) = \exp[-\Delta G(n_1, n_2, n_3)/k_B T]$, were projected onto a single coordinate, the combined size of the cluster n (= $n_1 + n_2 + n_3$). Specifically, for a cluster with a total size of n, its overall concentration $P^{tot}(n)$ is obtained by,

$$P^{tot}(n) = \sum_{n_1=0}^{n} \sum_{n_2=1}^{n-n_1} [P(n_1, n_2, n - n_1 - n_2)] \qquad (5.5)$$

Then $P^{tot}(n)$ can be converted back to the combined NFE for this given cluster size, $\Delta G^{tot}(n)$. With this one-dimensional free energy plot, the determination of the barrier height and critical cluster size is straightforward, just like single-component nucleation.

Considering that both *n*-nonane and 1-butanol are chain molecules, an energy-based Stillinger-type cluster criterion was employed, in which a cluster is defined as a group of molecules of which every molecule has at least one neighbor in the group with interaction energy less than U_{cl}. Based on experience (see section 4.2), U_{cl} is set to $-260\ k_B$ for all pairs of like or

unlike molecules except for the water/*n*-nonane pair and the *n*-nonane/1-butanol pair for which U_{cl} is set to –30 k_B and –120 k_B, respectively. In all calculations, the TraPPE-UA[81,106] force field was used for 1-butanol and *n*-nonane while the TIP4P[124] model was used for water. All simulations were carried out at T = 230 K, a common condition used for the experiments[116, 117, 125-128] and also for our previous simulations[38, 40, 51, 52] on binary mixtures. Thus the converged free energy data obtained therein were directly used for the construction of the initial biasing potential for this study. HR was used in a few cases for the interpretation of the data at 240 K, where the ternary nucleation experiment[46] was carried out. Each cluster of a specific size and composition was visited at least 10^5 times and on average about 10^6 times.

5.2.3 Results and Discussions

5.2.3.1 The Entire Onset Activity Surface for This Mixture

The onset activity plots (see Figure 5.5) form a surface in a three dimensional $a_1 - a_2 - a_3$ space. This surface intercepts with each of the three axes with a unit value where unary onset nucleation of each of the three corresponding components occurs. This surface also crosses with the three binary planes, yielding three separate curves which correspond to the onset activities of the three binary systems that can be made by mixing any two of the three components.

While for an ideal mixture, the onset activities would fall onto a plane with a_1, a_2, and a_3 summed up to be one, the onset activity surface plotted in Figure 5.5 clearly deviates from this planar-like ideal behavior. More interestingly, this surface displays several types of deviations or non-ideal features, which implies that the inherent nucleation mechanism can be rather diverse. These non-ideal features are also evident in the experimental onset activity plots constructed by Viisanen and Strey (see Figure 5.5b).[46] In fact, the two sets of onset activity plots, calculated and experimental, nearly coincide with each other. It should be noted that the experimental data

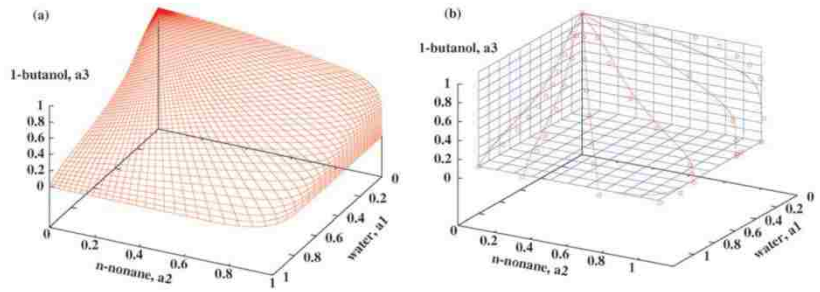

Figure 5.5. (a) The entire onset activity surface obtained from the simulation at any vapor – phase composition ratios; (b) Comparison of onset activities between the simulation at 230 K (solid lines) and the experiment[46] at 240 K (circles) at constant a_2' from 0 to 1 at 0.2 interval by varying the 1-butanol content. The dashed-dotted lines represent the simulation results interpreted from the histogram-reweighting technique at 240 K.

were only measured at a very sparse set of conditions, categorized according to the value of the normalized activity fraction of *n*-nonane, a_2', which changes from 0 to 1 at 0.2 interval, but these conditions are already representative enough to capture all the major non-ideal characteristics for this ternary mixture. Furthermore, these discretized a_2' values provide important landmarks that delineate a steady evolution/switching of the distinct types of non-ideal features shown in the onset activity data. For example, when a_2' is high (at 0.8), the onset activity plot closely resembles that observed for the binary *n*-nonane/1-butanol mixture (corresponding to a_2' = 1) by showing a higher combined activity than expected for an ideal mixture, which has been interpreted before as a sign of reluctant conucleation. When a_2' is low (up to 0.4), the onset activities curve to the opposite side, similarly to the binary water/1-butanol mixture (corresponding to a_2' = 0), which is a typical feature of mutual nucleation enhancement. On the contrary, at intermediate a_2' (*e.g.*, 0.6) both features are present on the onset activity plot.

5.2.3.2 Binary Water/1-Butanol- Like Non-Ideal Behavior at Low a_2'

To compare directly with the data obtained for the binary water/1-butanol mixture, the onset activity data calculated for this ternary system at low a_2' values were projected onto the a_1

– a_3 plane (see Figure 5.6a). Both our simulation and the experiment[46] show results for this ternary mixture that are almost identical to those found for the binary water/1-butanol system. It appears that *n*-nonane barely participates in the nucleation event at these low a_2' conditions, which is also evident from the average composition plots for the critical nuclei (see Figure 5.6b), where the mole fraction of *n*-nonane was shown to be consistently low over the entire range of conditions (specified by the a_3 value) for both our simulation and the experiment. It should be noted that the average composition of the critical nuclei was analyzed from the simulation through averaging the composition of all clusters with the critical cluster size weighted by their corresponding probability densities. In Viisanen and Strey's[46] experimental work, this property was derived indirectly from the application of the NT to the measured nucleation rate surface. Despite these rather different procedures, in all cases the two sets of data are in close agreement with each other, which seems to support the applicability of the NT in the experimental interpretation of this property. In addition, both indicate that the average composition of the critical nuclei (*i.e.*, the average mole fraction of each component) is hardly affected by the presence of *n*-nonane in the vapor phase, which supplies additional evidence for the notion of binary water/1-butanol-like nucleation behavior for this ternary mixture at these low a_2' conditions. Note that the negative mole fractions obtained for *n*-nonane from the experimental interpretation were due to the finite accuracy of the nucleation rate measurements, as pointed out by Viisanen and Strey.[46]

The NFE results obtained at the saddle point surface (or for clusters with the critical cluster size) further provide a mechanistic support of the binary-like behavior of this ternary mixture at the vapor-phase compositions considered here. In particular, at low a_2', these NFE landscapes consistently indicate that nucleation proceeds *via* mostly water/1-butanol-enriched

critical nuclei (see Figure 5.7). In addition, at each specific condition fully mixed critical clusters with the number of water and 1-butanol molecules proportional to their corresponding average mole fraction shown in Figure 5.6b were found more probable than clusters with other compositions. Thus, the nucleation mechanism can be classified as a single-pathway type at these conditions. However, in bulk phases, water and 1-butanol are known to exhibit a miscibility gap and the models used here have been shown to be consistent with this.[130] Clearly the appearance of only one major mixed critical nuclei (enriched by both water and 1-butanol components especially at intermediate a_3 values) deviates from this macroscopic trend (that would otherwise show an external phase separation from each other).

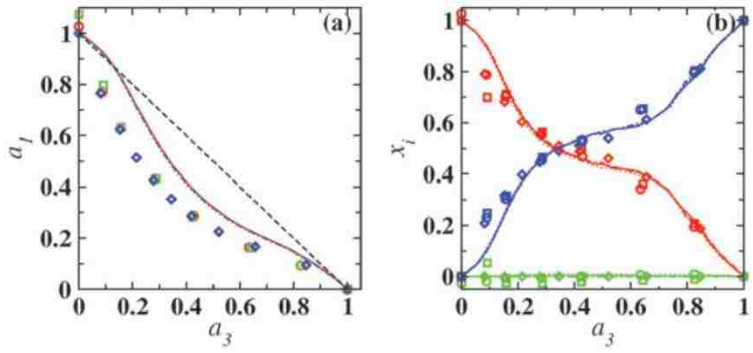

Figure 5.6. (a) Onset activities and (b) the average mole fraction of water (red), *n*-nonane (green), and 1-butanol (blue) of the critical nuclei as function of the vapor-phase composition obtained at a_2' value of 0 (diamonds and dashed-dotted lines), 0.2 (circles and solids lines), and 0.4 (squares and dotted lines). The symbols and lines denote the experimental data[46] and simulation results, respectively. The dashed straight line in panel (a) corresponds to the ideal case for a binary type of system.

Although these two components are both substantially present in the same cluster, visual inspection of the cluster configurations indicates that they tend to form an internally phase-separated structure (see Figure 5.7). That is, water molecules are located mainly in the interior of the cluster (forming a water core) and the 1-butanol molecules are enriched at the surface

(forming a 1-butanol corona), resembling the core-shell structure found previously for the binary water/ethanol nucleation.[38, 52] This core-shell structure is preferred for these clusters due to the same reason raised before for the formation of a 1-butanol monolayer at the bare water surface.[130] Namely, the enrichment of alcohol at both curved (for clusters) and infinitely planar surfaces (for bulk systems) allows additional hydrogen bonds to be formed between the excess free hydrogens of surface water and the excess hydrogen bond acceptor sites of alcohol. This core-shell structural pattern is also the microscopic origin for the observed mutual nucleation enhancement. In particular, surface enrichment of alcohol molecules lowers the surface tension and correspondingly the surface free energy as well as the nucleation free energy of clusters.[38] Thus, lower combined activities (than expected for an ideal mixture) are required to achieve the same onset nucleation rate or barrier height (see Figure 5.6a). As all alcohol molecules are capable of developing surface monolayers at the water surface, the mutual nucleation enhancement is expected to be a common feature for the water/1-alcohol series. Indeed, the experiments for binary nucleation of water mixed with 1-alcohol up to 1-hexanol all show this feature despite the even greater tendency to demix macroscopically for the longer alcohols.[40] It is likely that all these binary water/1-alcohol systems would also share a mechanistic landscape similar to the one shown in Figure 5.7b, with only one major nucleation channel. However, for longer alcohols, a bifurcation should eventually appear on the NFE map (resembling the phase separation observed for the bulk systems of these mixtures) but is not observed here for the water/1-butanol system due to the small cluster sizes sampled by these simulations.

5.2.3.3 Binary *n*-Nonane/1-Butanol-Like Behavior Mixed Slightly with Binary Water/1-Butanol-Like Behavior at High a_2'

While at lower a_2', the nucleation behavior of this ternary mixture can be unambiguously assigned as a binary water/1-butanol type, the results obtained at high a_2' turn out to be slightly

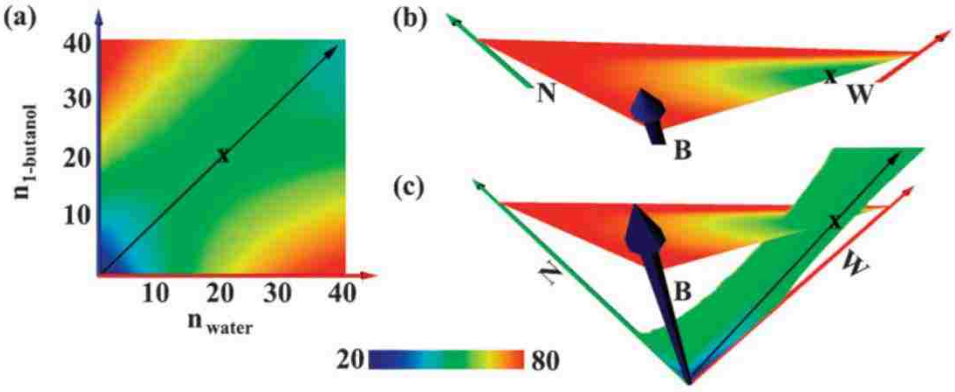

Figure 5.7. NFEs (in units of kBT) as function of cluster composition at a_1 = 0.428, a_2' = 0.4, and a_3' = 0.35: (a) a front view of this NFE landscape to illustrate the major nucleation channel along the water (W)/1-butanol (B) surface; (b) the NFE contour obtained at the saddle point surface or for clusters with the critical cluster size; and (c) a perspective view of the major nucleation channel on the NFE landscape to show how it passes through the saddle point surface. The cross and black line with an arrow head were drawn as a guide for the saddle point and the nucleation path, respectively.

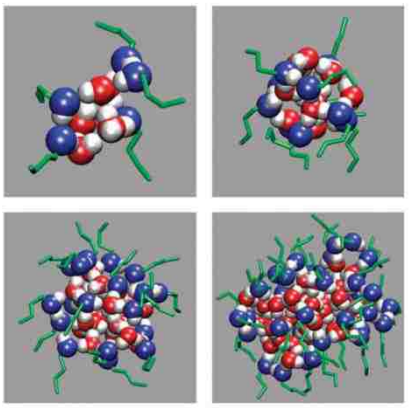

Figure 5.8. Representative snapshots of clusters (consisting of 5, 10, 20 and 40 molecules of each component) obtained from the binary nucleation simulation of water / 1-butanol. Color notation: water oxygen (red); 1-butanol oxygen (blue); hydrogen (white); and alkyl tails (green stick).

more complicated. Even at a_2' = 0.8, where the normalized activity of *n*-nonane is four times larger than that of water, substantial presence of water in the critical nuclei remains likely, as suggested from the average composition plots interpreted from the NT for the critical nuclei provided by the experimental paper[46] (see Figure 5.9). The same was found from our simulation.

In fact, our calculated average compositions for the critical nuclei again are nearly spotted on the experimental values for these high a_2' conditions. While these composition plots indicate that all three components can be substantially present at a certain range of conditions (centered at around an a_3 value of 0.35), outside that range the nucleation of this ternary mixture proceeds through either *n*-nonane-enriched or 1-butanol-enriched nuclei (similar to the binary *n*-nonane/1-butanol system). In particular, the composition plots for both *n*-nonane and 1-butanol components exhibit the typical reluctant conucleation characteristics found for the binary *n*-nonane/1-alcohol system, with a sigmoidal shape showing a depletion of 1-butanol at low 1-butanol activity or depletion of *n*-nonane at high 1-butanol activity. This reluctant conucleation feature is also evident from Figure 5.5, which displays higher combined onset activities than expected for an ideal mixture, just opposite to the water/1-butanol-like behavior discussed in Chapter 4.

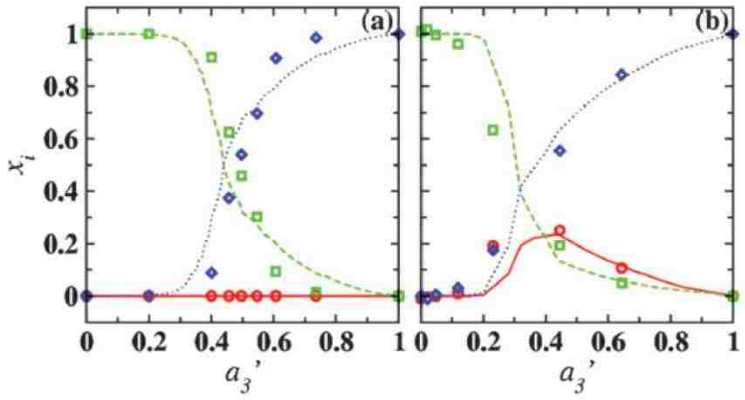

Figure 5.9. The average mole fraction of water (circles and solid lines), *n*-nonane (squares and dashed lines), and 1-butanol (diamonds and dotted line) of the critical cluster as function of the vapor-phase composition obtained at (a) a_2' = 1.0 and (b) a_2' = 0.8. The symbols and lines denote the experimental data[46] and simulation results, respectively.

Clearly the average composition data obtained at intermediate a_3' values (that indicate substantial presence of all three components in the critical nuclei) have turned this ternary

nucleation into a more intriguing case. Viisanen and Strey[46] interpreted these results as a sign of enhanced miscibility and suggested that 1-butanol works as a surfactant to bring the two incompatible components water and *n*-nonane together in a single cluster. In this interpretation, they seemed to implicitly assume that only one major critical cluster is present, despite the fact that the average composition on its own cannot completely rule out the possibility of the external phase separation for these cluster systems (or the coexistence of multiple critical nuclei, with each having a unique composition that can be significantly different from the average composition). As demonstrated from our previous simulation on binary systems (involving components similar to this ternary mixture),[38, 40, 52] the statistical averaging over multiple critical nuclei of different compositions can equally well produce an average composition that shows similar contribution from all components to the critical nuclei. The binary *n*-nonane/1-butanol mixture is an example, for which at intermediate vapor-phase compositions both the experiment and the simulation yielded an average mole fraction close to 0.5 in the critical nuclei for either component (see Figure 5.9a). But it was found from the simulation that critical nuclei with a wide range of compositions were actually present for this system – a special feature that was attributed to the nearly perfect balance between the tendency to mix and the tendency to demix between *n*-nonane and 1-alcohol for medium-length alcohols like 1-butanol.[40]

While the binary *n*-nonane/1-butanol-like multi-pathway feature remains prominent for this ternary system (see the NFE map shown in Figure 5.10a; which provides a mechanistic explanation of the reluctant conucleation observed at high a_2' conditions), the addition of a small amount of water also leads to the appearance of a new class of critical nuclei (or nucleation pathways) dominated by both 1-butanol and water components (see Figure 5.10b). Although the average composition obtained at this condition indicates the substantial presence of all three

components, the tendency for water and *n*-nonane to demix from each other is evident as the NFE map around the saddle point region shows a clear external phase separation into either water/1-butanol- or *n*-nonane/1-butanol-enriched critical nuclei. We calculated separately the average composition for these two groups of critical nuclei and found on average a critical cluster contains 11.1 water, 2.5 *n*-nonane, and 22.4 1-butanol in the former group (which constitutes about 60% of the overall critical nuclei) *versus* 1.2 water, 27.4 *n*-nonane, and 7.4 1-butanol in the latter group. Although neither group shows a substantial presence of all three components, these numbers compare more favorably to the miscibility data obtained solely between water and *n*-nonane. For example, at this condition in the absence of 1-butanol a water-enriched cluster with about 11 water molecules attracts < 0.1 *n*-nonane into the cluster. Even fewer water molecules (about 0.0002 on average) are found in an *n*-nonane-enriched cluster with a size of 28 (this size is chosen based on the number of *n*-nonane molecules contained by *n*-nonane-enriched critical nuclei in the ternary nucleation mixture). From this comparison, we

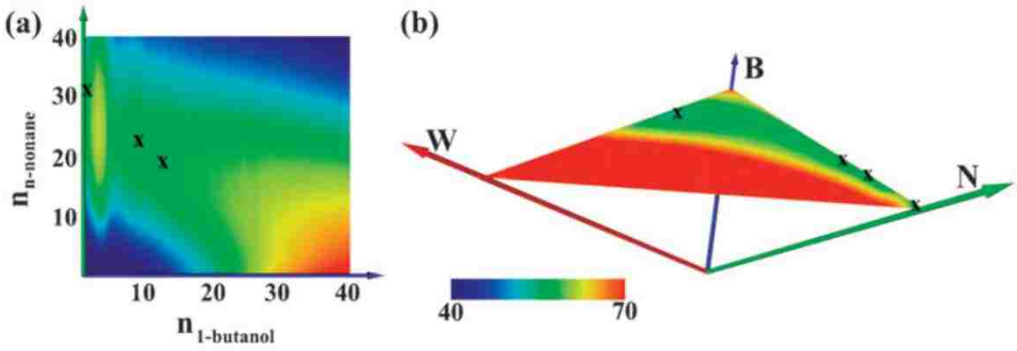

Figure 5.10. NFEs (in units of kBT) as function of cluster composition at a1 = 0.212, a′2 = 0.8, and a′3 = 0.35: (a) A front view of this NFE landscape to illustrate the multi-pathway feature along the n-nonane (N)/1-butanol (B) surface; and (b) the NFE contour obtained at the saddle point surface or for clusters with the critical cluster size. Crosses were drawn as a guide for the saddle points.

reached the same conclusion made by Viisanen and Strey,[46] that is, 1-butanol does work as a surfactant in this ternary mixture and leads to an enhanced miscibility between water and *n*-

nonane. However, this miscibility enhancement is still insufficient to make them fully miscible at the range of conditions examined here.

5.2.3.4 Binary *n*-Nonane/1-Butanol-Like Behavior Mixed Substantially with Binary Water/1-Butanol-Like Behavior at Intermediate a_2'

Our former simulation study (see section 5.1)[49] was carried out at an intermediate a_2' value of 0.6, where excellent agreement with the experiment[46] was found for the onset activities and the average composition of the critical nuclei. Here two neighboring conditions (a_2' = 0.5 and 0.7) were also added into this part of discussion. For all cases, the onset activity plots (see Figure 5.11a) revealed a similar non-ideal pattern that seems to arise from an optimal combination of the two classes of non-ideal nucleation behavior that were found for this ternary mixture at either lower or higher a_2'. While the reluctant conucleation behavior (characterized by a concave-up shape for the onset activity plot) is prominent at high *n*-nonane activity, the mutual nucleation enhancement feature (characterized by a concave-down shape for the onset activity plot) starts to take over immediately as a_2 is slightly below one. Analysis of the average composition of the critical nuclei indicated that around the switching locations (specified by the a_3' values) between these two types of non-ideal features, the critical clusters also experienced a revolutionary change of their molecular contents (see Figure 5.11b). Specifically, at those locations the mole fraction of *n*-nonane (an originally dominant component in the critical nuclei at low a_3') sharply decreases and the disappearance of *n*-nonane is accompanied by a rapid entering of 1-butanol into the critical clusters, followed by water. Note that the composition plots obtained at a_2' = 0.5 exhibit a unique feature of having both *n*-nonane and water present in the critical nuclei even in the absence of 1-butanol. This was shown previously as a result of forming two major critical nuclei, one water-enriched and the other *n*-nonane-enriched.[38, 40, 52] On the

other hand, the average composition data for a_2' = 0.7 look qualitatively the same as a_2' = 0.6 and thus are not included in Figure 5.11b.

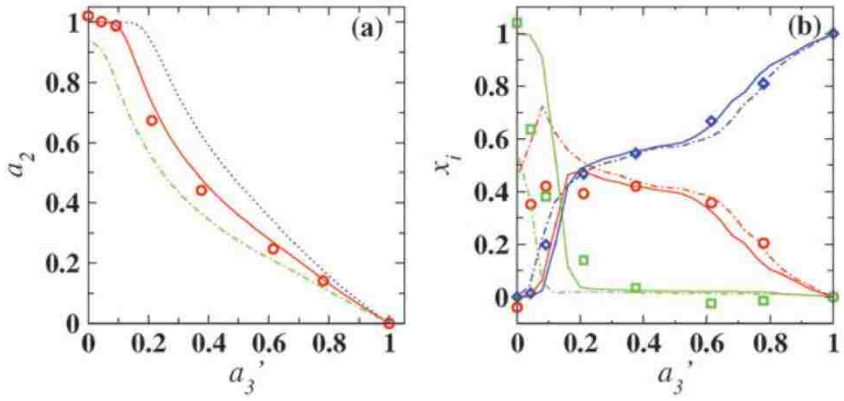

Figure 5.11. (a) Onset activities and (b) the average mole fraction of water (red), *n*-nonane (green), and 1-butanol (blue) of the critical nuclei as function of the vapor-phase composition obtained at a_2' value of 0.5 (dashed-dotted lines), 0.6 (solids lines), and 0.7 (dotted lines). For comparison, the experimental data[46] obtained at a_2' = 0.6 were also shown (as symbols).

Although the sharp change of the average composition for the critical nuclei implies a mechanistic transformation around those switching locations (*i.e.*, from *n*-nonane dominated pathways to those *via* water/1-butanol-enriched clusters), the exact details about this transformation cannot be completely determined from the average composition information. In particular, the nucleation mechanisms for this ternary mixture located exactly at these switching conditions remain uncertain as the average composition data there show substantial presence of all three components (which could be interpreted as forming either one single critical nuclei of this composition or multiple critical nuclei with different compositions). Similar to the a_2' = 0.8 case, the NFE results obtained at the saddle point surface (or for critical clusters) were used to resolve the mechanistic puzzle for this ternary mixture near these switching locations. As shown in Figure 5.12, external phase separation into multiple types of critical nuclei of different compositions is again the most prominent feature for these NFE maps, resembling the one shown

in Figure 5.10b. One major type of critical nuclei is still enriched by both water and 1-butanol components (containing on average 15.7 water, 0.9 *n*-nonane, and 13.4 1-butanol), while the other type is dominated by only *n*-nonane (containing on average 0.03 water, 29.9 *n*-nonane, and 0.09 1-butanol). This phase separation feature remains evident even for larger clusters, albeit a small improvement of the *n*-nonane:water ratio was found for the water/1-butanol-enriched clusters. For example, at a combined size of 60, the water/1-butanol-enriched clusters contain on average 34.2 water, 2.1 *n*-nonane, and 23.7 1-butanol.

Visual inspection of clusters (see Figure 5.13) containing equal molar amounts of the three components indicates an internal phase separation into a multilayered structure (called an "onion" in Nellas et al.[51]). In accord with the speculation by Viisanen and Strey,[46] the formation of this phase-separated structure is dictated by the core (water) – shell (1-butanol) motif found previously for the binary water/1-butanol mixture as well as the preference of *n*-nonane to interact with the alkyl tail of 1-butanol molecules. In fact, this core-shell structure prepares a non-polar surface (that is covered mainly by the alkyl tails of 1-butanol) for a more favorable deposition of *n*-nonane compared to the bare water surface. This leads to the enhanced

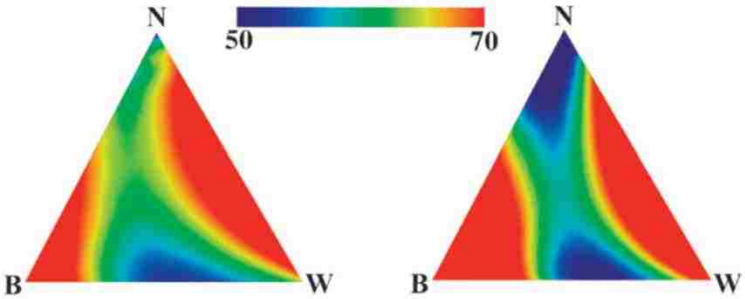

Figure 5.12. NFEs (in units of k_BT) of the critical clusters (left; at a size of 36) and the post-critical clusters (right; at a size of 57) as function of the cluster composition at $a_1 = 0.608$, $a_2' = 0.6$ and $a_3' = 0.14$. These contours are similar to the one shown in Figure 5.10b with W, N, and B denoting the same three axes there, but are projected in a different orientation so that we have a full frontal view of these surfaces.

miscibility of water with *n*-nonane observed in the presence of 1-butanol. However, the tendency for *n*-nonane to deposit just on one side of (rather than wrapping around) this core-shell structure may suggest that 1-butanol is just too short to act effectively as an amphiphile to bring water and *n*-nonane together to form a more symmetrical spherical structure. Clearly *n*-nonane molecules prefer to interact with themselves rather than with the non-polar tails of 1-butanol. Direct evidence on the formation of the core – shell structure has been recently provided by the small angle neutron scattering experiments on nano-droplets formed by water and 1-butanol.[119] Such a core-shell structure has been also suggested as an important motif for explaining the high organic content for many types of atmospheric aerosols as well as the likely prebiotic environment for the early development of life.[120-123]

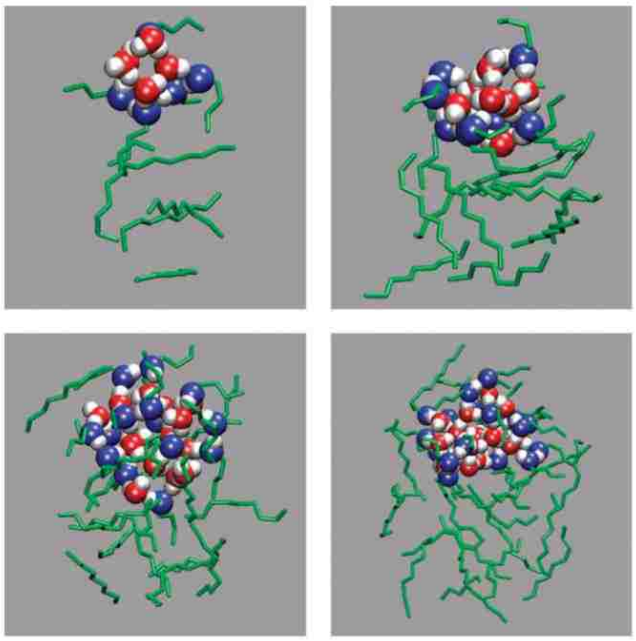

Figure 5.13. Representative snapshots of clusters (consisting of 5, 10, 15, and 20 molecules of each component) obtained from the ternary nucleation simulations. Color notation as Figure 5.8.

5.2.3.5 Implications from the Nanophase Diagrams on Tailor – Made Nanoparticles

The nucleation free energy landscapes displayed in Figures 5.7, 5.10, and 5.12 represent some of the very first "nanophase diagrams" reported to date. Compared to bulk systems, these diagrams indicate that many more intermediate "nanophases" are able to coexist for particles of nanometer in size without a sharp boundary. This seems to implicate that precise structural control for nano-objects would be a delicate issue. Fortunately, for particles of small sizes, the "nanophase diagram" evolves rapidly with a change of the condition (such as the activities) and the structure formed is dependent upon the presence of other species. Therefore, through the "nanophase diagram" and the molecular-level structural insights, our simulation approach may offer a way to predict the optimal conditions for making clusters of a particular structure.

5.2.4 Concluding Remarks

In summary, this section reports the atomistic simulation investigation of the ternary nucleation of the water/*n*-nonane/1-butanol system. Using the atom-based transferable force fields, these simulations were able to reproduce the complex non-ideal nucleation behavior observed experimentally for this system. In particular, good agreements were found between these simulations and the experiment by Viisanen and Strey[46] on both onset activities and the average composition of the critical nuclei. A close examination of the nucleation free energy landscape reveals that this ternary nucleation could take on various sets of paths at different vapor-phase compositions but none of the major pathways proceeds *via* critical nuclei that contain substantial amount of all three components. Furthermore, by comparing these results to those obtained for the binary water/1-butanol and *n*-nonane/1-butanol mixtures, it can be concluded that the seemingly complex non-ideal behavior observed for this ternary system can be described in terms of the two distinct types of non-ideal nucleation features exhibited by the

binary water/1-butanol mixture and the binary *n*-nonane/1-butanol mixture, respectively. For example, at low *n*-nonane activities, nucleation of this ternary mixture would proceed *via* a single binary-like water/1-butanol channel with the onset activity plots showing a dominant mutual nucleation enhancement feature, similar to that observed for water/1-butanol, due to the formation of a core (water)–shell (1-butanol) cluster structure. While at high *n*-nonane activities, nucleation of this ternary mixture would proceed *via* critical clusters enriched by mainly *n*-nonane and 1-butanol (sometime resembling the multi-pathway feature present in the binary *n*-nonane/1-butanol system when the normalized activities are comparable between *n*-nonane and 1-butanol), with reluctant conucleation as the main characteristic on the onset activity plots, just like *n*-nonane/1-butanol. On the other hand, a proper balance of these two major nucleation channels would lead to the mixing/switching of these two types of features, which produces a pseudo-ideal nucleation behavior that appears mainly at intermediate vapor-phase compositions. These findings may inspire new theoretical development on multicomponent nucleation phenomena. Through the construction of the "microphase diagram", our simulation approach may also offer a way to predict the optimal conditions for making clusters of a particular structure, which is important in the tailor-design of nano-objects.

5.3 Molecular Content and Structure of Aqueous Organic Nanodroplets from Vapor-Liquid Nucleation Study of the Water/*n*-Nonane/1-Alcohol Series[P4]

5.3.1 Introduction

In this section, the AVUS-HR approach was applied to investigate the homogeneous vapor-liquid nucleation of the ternary water/*n*-nonane/1-alcohol series. This includes water/*n*-nonane/ethanol, water/*n*-nonane/1-butanol, water/*n*-nonane/1-hexanol, and water/*n*-nonane/1

[P4]Reprinted with permission from *J. Phys. Chem. A* **2008**, 112, 2930-2939. Copyright 2008 American Chemical Society

octanol. This investigation was inspired from the experimental work of Viisanen and Strey[46] on water/*n*-nonane/1-butanol and on former simulations carried out by us (see sections 5.1 and 5.2).[44, 51] Based on our observation that 1-butanol may be too short to act effectively as a surfactant for water and *n*-nonane immediately prompted this investigation of other alcohols (especially longer ones). In addition, this simulation study provided other crucial molecular details regarding the composition and structural distribution of the three components and their miscibility in the clusters. Our results suggest an external separation into either water/1-butanol-enriched or *n*-nonane/1-butanol-enriched clusters even at those intermediate gas-phase compositions when the average content of the critical nuclei show equal contributions from all components involved.

Apart from being of relevance to microemulsions, multiple-component mixtures that contain these three species are ideal model systems for atmospheric organic aerosols. Concern was recently raised about the composition/structure of such carbonaceous droplets due to their direct impact on cloud albedo.[120, 131, 132] In addition, these particles possess a surprisingly high organic content that cannot be fully explained by the classical homogeneous model and the aqueous solubilities of the organic compounds.[120-123] In these organic aerosols, long chain amphiphiles (e.g., polyacids) were involved as an important component, which are well-known to cause a nonuniform structural/composition arrangement when mixing with either more polar species such as water or the more nonpolar hydrocarbon components. A core-shell (water−surfactant) structure has been proposed as a motif for explaining the high organic content for these atmospheric aerosols.[121-123] This speculation has been directly confirmed by small angle neutron scattering experiments on nanodroplets formed by water and 1-butanol[119] and also by simulations,[38, 44, 51, 52, 133] e.g., for binary water/ethanol and ternary water/*n*-nonane/1-butanol

clusters. Here it will be shown that the core-shell structure formed by longer alcohols (a better mimic of polyacids and other surfactant molecules) can further attract less polar organic materials (such as purely nonpolar alkanes) onto the cluster surface, which would not only lead to an enriched carbon content but also have some new implications for the properties of those atmospheric droplets.

5.3.2 Simulation Details

Being an activated event, nucleation can be characterized by a free energy (NFE) profile expressed as a function of order parameters, e.g., cluster size for single-component systems and also composition for multicomponent vapor-liquid nucleation (or numbers of molecules of each component contained by the cluster, i.e., $\{n_i\}$). Constructing this NFE landscape, $\Delta G(\{n_i\})$, or equivalently the cluster probability, $P(\{n_i\}) = \exp[-\Delta G(\{n_i\})/k_B T]$, becomes the major task for simulation. The simulations reported here were all carried out using the grand-canonical version of the nucleation algorithm.[36, 37] The NFE data were evaluated for all clusters of interest (i.e., up to a size slightly larger than the critical clusters) at only one set of gas-phase activities, which was directly specified as part of the simulation conditions. Interpretations at other conditions were then made using the following equation 5.4 (see section 5.2).[44] This interpretation allows us to map all the possible combinations of gas-phase activities that would yield similar barrier heights (or nucleation rates) for the construction of the onset activity plots. Following the procedure specified in the previous sections, a constant combined nucleation barrier height of 50.64 $k_B T$ (corresponding to a critical cluster concentration of 10^{-22} droplets/Å^3 or 100 droplets/cm^3) was used to determine the onset activities. This combined nucleation barrier allows us to take into account the contributions from all possible pathways (critical nuclei) present on the NFE map, which is important for multicomponent systems.

While water was modeled by TIP4P,[124] the TraPPE-UA[81, 106] force field was used for both *n*-nonane and 1-alcohol. As chain molecules were involved in these simulations, we employed an energy-based Stillinger-type cluster criterion.[84] Following our previous ternary nucleation work on water/*n*-nonane/1-butanol,[44, 51] U_{cl} is set to $-260\ k_B$ K for all pairs of like or unlike molecules except for the water/*n*-nonane pair and the *n*-nonane/1-alcohol pair for which U_{cl} is set to −30 and $-120\ k_B$ K, respectively. All simulations were carried out at T = 230 K, which is around the condition range accessible by the nucleation pulse chamber experiments for such systems (but only water/*n*-nonane/1-butanol has been studied experimentally).[46] Each cluster of a specific size and composition was visited at least 10^5 times and on average more than 10^6 times.

5.3.3 Results and Discussions

5.3.3.1 Plots of the Onset Activities

Plotted in Figure 5.14 are the various combinations of onset activities, $\{a_i\}$, with i = 1, 2, and 3, denoting water, *n*-nonane, and 1-alcohol, respectively, obtained for a constant combined barrier height of 50.64 k_BT (only the data for water/*n*-nonane/1-hexanol were shown and the other systems exhibit similar features). Because only two of the three a_i's are independent, the onset activity data form a surface in a three-dimensional $a_1 - a_2 - a_3$ space (represented by a mesh-network in Figure 5.14). These a_i's have been normalized by the activities of the corresponding neat component. Thus, the onset activity surface crosses each of the three axes with a unit value, where unary onset nucleation of each of the three components occurs.

Shown in Figure 5.15 are a discretized group of onset activity curves obtained at the conditions used by Viisanen and Strey[46] in their pulse chamber experiment for the water/*n*-nonane/1-butanol system. These conditions can be classified on the basis of the value of the

normalized activity fraction of *n*-nonane, a_2', defined as $a_2 / (a_1 + a_2)$ (see equation 5.1), which changes from 0 to 1 in intervals of 0.2. For comparison, their experimental data were also included in Figure 5.15. As is evident from this figure, the simulation data capture very well the several distinct types of non-ideal characteristics exhibited by the experimental onset activity results for this ternary system at the different vapor-phase composition conditions. Also these rather diverse sets of features seem to be common for the ternary water/*n*-nonane/1-alcohol series (at least up to 1-octanol). For example, at low a_2' conditions, a sign of mutual nucleation enhancement is prominent, especially for shorter alcohols, with the combined activity lower than

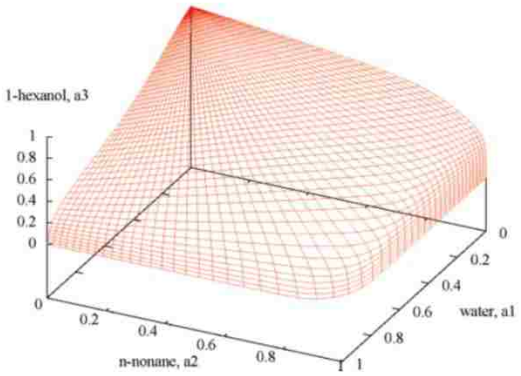

Figure 5.14. Entire onset activity surface obtained for the water / *n*-nonane / 1-hexanol system from the simulation at a constant combined barrier height of 50.64 $k_B T$.

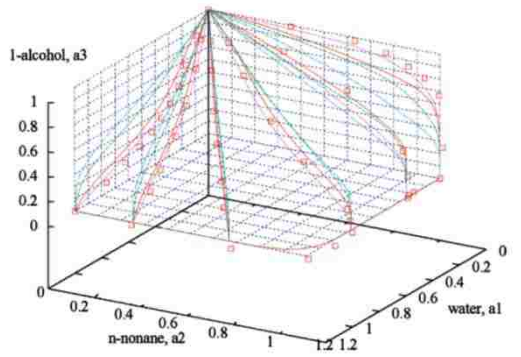

Figure 5.15. Onset activity curves obtained at a discretized set of varying from 0 to 1 at intervals of 0.2 for water/*n*-nonane/ethanol (magenta), water/*n*-nonane/1-butanol (red), water/*n*-nonane/1-hexanol (green), and water/*n*-nonane/1-octanol (cyan). The experimental data[46] obtained for water/*n*-nonane/1-butanol at 240 K are also included as red squares.

the unit value expected for an ideal mixture (similar to water/1-alcohol). On the contrary, when a_2' is high, the onset activity plots show a dominant reluctant conucleation feature, with the combined activity higher than for an ideal mixture (similar to binary *n*-nonane/1-alcohol). On the other hand, both features were found to be present in the onset activity plot obtained at intermediate conditions.

5.3.3.2 Core-Shell Structures Formed by the Water/1-Alcohol Clusters and Comparison to the Experimental Data for These Binary Series

Note that experimental data for this ternary series are only available for water/*n*-nonane/1-butanol, whereas extensive nucleation rate measurements have been carried out by Strey and coworkers for binary *n*-nonane/1-alcohol[116] and water/1-alcohol systems (up to 1-hexanol).[47, 128] The ternary nucleation simulations reported here allow a convenient examination of these two groups of binary systems (by setting to either one or zero) to compare with the experimental data. For the former series, this comparison has already been done by us previously (see Chapter 4).[40] Important results are (i) the simulation data reproduced well the non-ideal reluctant conucleation characteristics reported previously from the experiment[116] on the *n*-nonane/1-alcohol series and (ii) when this series moves away from the miscibility gap, the nucleation mechanism evolves from a two-pathway type for *n*-nonane/methanol to a single-pathway mechanism for *n*-nonane mixed with longer alcohols, and passes through a multiple-pathway-like mechanism for those intermediate cases involving medium-length alcohols such as ethanol. This microscopic miscibility information matches well with the macroscopic miscibility data for these two species. For example, methanol and *n*-nonane are known to have a miscibility gap, which vanishes quickly with increasing alcohol chain length.

Similar to the *n*-nonane/1-alcohol series, the macroscopic miscibility between water and 1-alcohol also exhibits a chain-length dependence but in this case decreases with the number of

carbon atoms in the alcohol. For example, 1-butanol is the shortest 1-alcohol that already displays a miscibility gap with water. Although the maximum water solubility in 1-butanol (or longer alcohols) is about 0.5 (or lower) in terms of mole fraction, the alcohol solubility in water drops rapidly with increasing chain length and is below 0.02 for all except the fully miscible alcohols.[128] In contrast, the molecular content of the critical nuclei inferred from the experimental nucleation rate[128] through the nucleation theorem[49] indicated that the average composition could range continuously from pure water to pure alcohol irrespective of the alcohol chain length (see Figure 5.16). The results from our simulation are not much different. In fact, the two sets of results (calculated versus experimental[47, 116, 128]), plotted as a function of the normalized activity fraction of 1-alcohol, a_3', defined as $a_3 / (a_1 + a_2 + a_3)$ (see equation 5.2), follow each other closely. For ideal mixtures, it is expected that these data will fall onto a straight-line linked by the two end points that correspond to the unary nucleation of either water or 1-alcohol (see the dashed line included in Figure 5.16). Clearly, both the simulation and experimental data show a certain degree of enrichment of 1-alcohol at low 1-alcohol activity or enrichment of water at low water activity, especially for shorter alcohols. This behavior is just the opposite of that found for the *n*-nonane/1-alcohol systems, for which the results were shown in Figure 5.16 as well. Also distinct from *n*-nonane/1-alcohol are the mutual nucleation enhancement characteristics exhibited by the onset activity plots (see Figure 5.17), with a concave-down curvature versus concave-up (signaling reluctant conucleation) for *n*-nonane/1-alcohol. This feature gradually diminishes toward longer alcohols. Actually, for both 1-hexanol and 1-octanol, the simulation data show the presence of a region (at low alcohol activity conditions) with the combined activities higher than the unit value expected for an ideal mixture, resembling to some extent the reluctant conucleation feature of the *n*-nonane/1-alcohol system,

which is also consistent with the depletion of the alcohol over that range of conditions (see Figure 5.17). It should be mentioned that for mixtures approaching or already showing macroscopic miscibility, the average composition alone cannot completely rule out the possibility of external phase separation for these cluster systems or the coexistence of multiple critical nuclei, each having a unique composition that can be significantly different from the average composition.[26, 28, 31, 38, 40, 52-54] To further examine the miscibility information, the nucleation free energy contours detailing the probabilities of observing clusters of all compositions were displayed in Figure 5.18 (for a condition when the average composition of the critical nuclei indicates equal amounts of both components). Only the data obtained for the water/1-hexanol mixture were shown as they are quite representative of the rest of the systems (including the fully miscible water/ethanol).

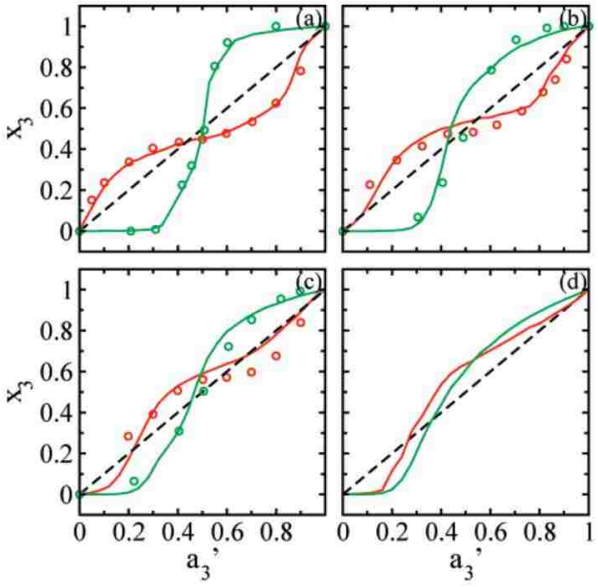

Figure 5.16. Average mole fraction of 1-alcohol in the critical nuclei as a function of its activity fraction obtained for binary (a) water/ethanol, (b) water/1-butanol, (c) water/1-hexanol, and (d) water/1-octanol. For comparison, the data obtained for the binary *n*-nonane/1-alcohol series are also shown (in green). The symbols and lines denote the experimental data[47, 116, 128] and simulation results, respectively. The dashed straight line corresponds to the ideal case.

Despite the fact that water/1-hexanol has a macroscopic miscibility gap (and the models used here have been shown to be able to predict such bulk-phase separation behavior for the water/1-alcohol mixture),[118, 130] only one major type of critical nuclei (and correspondingly a single nucleation pathway) can be identified from the NFE map shown in Figure 5.17, with the most probable composition close to 15 molecules of each type. This provides direct support for the notion that small clusters can have different miscibility behavior from the bulk systems.

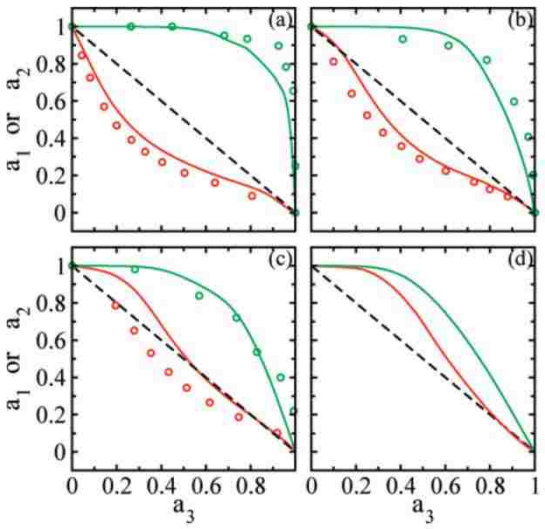

Figure 5.17. Plots of the reduced onset activities for the binary water/1-alcohol and *n*-nonane/1-alcohol series. Symbols and panels are the same as Figure 5.16.

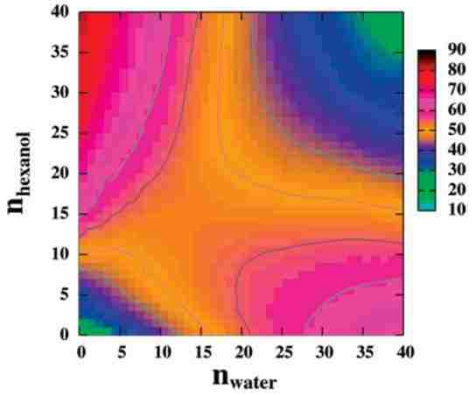

Figure 5.18. Contour plot of the two-dimensional NFE (in units of k_BT) as a function of the number of water and 1-hexanol molecules calculated from the simulation at a_1 = 0.68 and a_3 = 0.40. The contour levels with NFE values of 45, 50, 55, and 60 k_BT were depicted as lines for a clear view of the NFE profiles near the saddle point.

It was speculated by Strey and co-workers[128] that the enrichment of 1-alcohol at the cluster surface, i.e., in a structural motif of the core-shell (water-alcohol) type, may be the source of the deviation for these microscopic miscibility data compared to their bulk counterparts. This structure has been confirmed previously on systems involving shorter alcohols (e.g., ethanol and 1-butanol) by molecular dynamics[133] and Monte Carlo[38, 44, 51, 52] simulations and lately by experiments[119] as well on clusters that are several orders of magnitude larger than the critical clusters found here. Here clusters containing longer alcohols also adopt a dominantly core-shell motif (see Figure 5.19). This result is expected considering that all alcohol molecules are capable of developing Langmuir monolayers at the water surface. In fact, through the formation of such monolayer structures, both water and alcohol can benefit from the additional hydrogen bonds formed between the excess free hydrogens of surface water and the excess hydrogen bond acceptor sites of alcohol.[38, 130] For example, for single-component clusters of size 40, the average number of hydrogen bonds is 3.27 per water (or 2.00 per 1-hexanol) molecule, whereas this number increases to 3.80 per water (or 2.18 per 1-hexanol) for mixed clusters, using the criteria: $r_{OH} < 2.5$Å and $-1 < \cos\theta_{OH\cdots O} < -0.4$.[38] This surface monolayer is also the reason for the mutual nucleation enhancement observed especially for shorter alcohols as it greatly lowers the surface tension and correspondingly the surface free energy of the cluster formation.[130] However, for these cluster systems the formation of the curved monolayer structures comes at a price of losing some of the attractive interactions between the alcohol alkyl tails. This factor becomes more important with increasing alcohol chain length and is part of the reason for the gradual disappearance of the mutual nucleation enhancement feature (see Figure 5.17c,d) and for the depletion of the alcohol at low alcohol activity fraction as the chain length increases (see Figure 5.16c,d). In particular, depositing an individual alcohol molecule on the water surface would be

unfavorable due to the absence of alkyl tail interactions. Correspondingly, the alcohol monolayer is formed through a more collective process (triggered also by a further increase of the alcohol activity for longer chains), which explains the sudden jump in the 1-alcohol content of clusters at an value of around 0.2 (see Figure 5.16c,d).

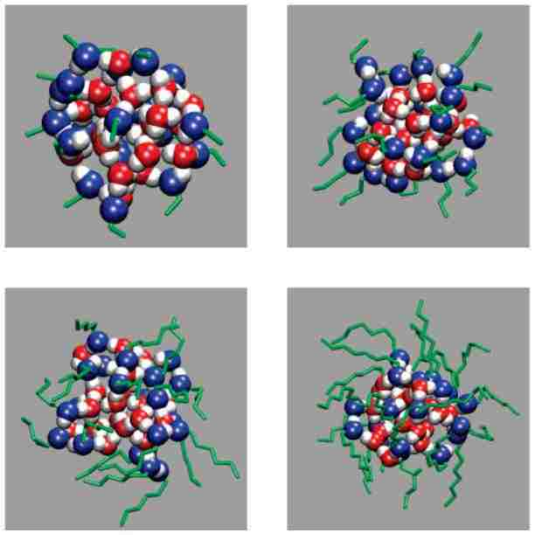

Figure 5.19. Representative snapshots of binary water/1-alcohol clusters (consisting of 20 molecules of each component) obtained from the four systems using alcohols of different chain lengths. Color notation: water oxygen (red); 1-alcohol oxygen (blue); hydrogen (white); and alkyl tails (green stick).

5.3.3.3. Enhanced Miscibility between Water and *n*-Nonane Due to the Presence of Alcohols via the Core-Shell Motif

Being an amphiphile and sharing components that are alike to both polar water and nonpolar alkanes, alcohols are expected to improve the miscibility between these two species. The core-shell motif formed between water and 1-alcohol shown in Figure 5.19 has already provided some structural hints for this enhanced miscibility. In particular, the nonpolar surface (covered by the alkyl tails of the alcohols) becomes more attractive for the adsorption of the purely nonpolar *n*-nonane than the original bare water surface. Indeed, mixed clusters containing

equal amounts of these three components show a dominantly "onion-like"[51] core-shell motif with *n*-nonane deposited outside forming an additional layer (see Figure 5.20). This enhanced miscibility mechanism is also evident when comparing these structures to those formed solely between water and *n*-nonane (see Figure 5.20a), where these two incompatible components display a consistent preference to segregate from each other forming two individual droplets. This type of phase separation remains prominent even in the presence of short alcohols (such as ethanol and 1-butanol, see Figure 5.20b-d) or a limited number of longer 1-alcohol molecules (see Figure 5.20e,g). In the latter case, the clusters are shaped more like a "dumbbell" and the addition of a few alcohol molecules simply introduces a surfactant handle to link the water and oil droplets together.[51] However, with the addition of more alcohol molecules into the clusters, the dumbbell structure quickly evolves into the onion due to the tendency for the alcohols to be distributed around the water surface to form the core-shell motif.

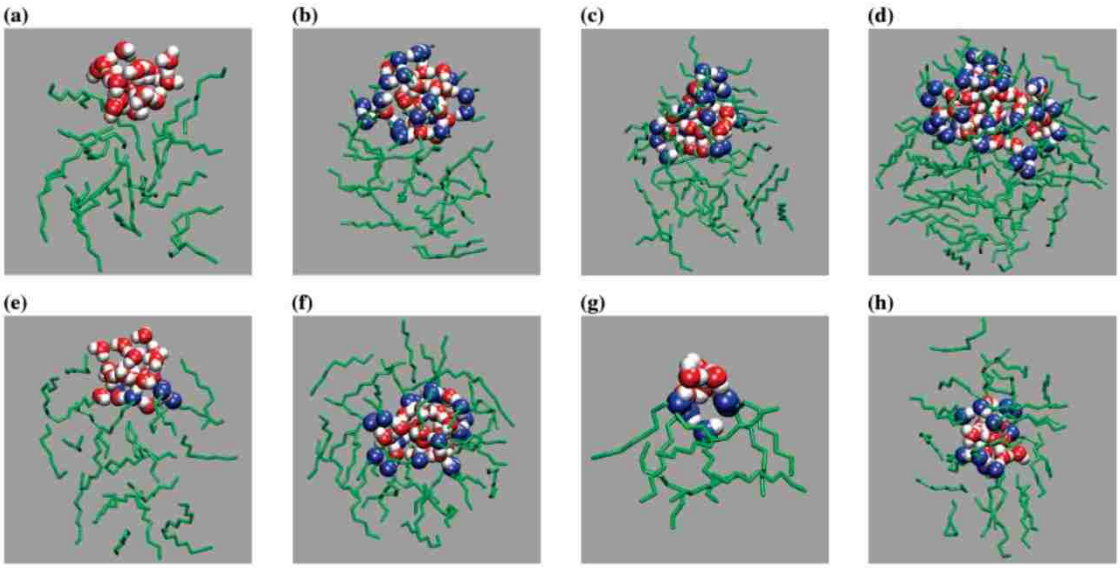

Figure 5.20. Representative snapshots for mixed clusters consisting of (a) 20 water and 20 *n*-nonane; (b) 20 water, 20 *n*-nonane, and 20 ethanol; (c) 20 water, 20 *n*-nonane, and 20 1-butanol; (d) 40 water, 40 *n*-nonane, and 40 1-butanol; (e) 20 water, 20 *n*-nonane, and 5 1-hexanol; (f) 20 water, 20 *n*-nonane, and 20 1-hexanol; (g) 5 water, 5 *n*-nonane, and 5 1-octanol; and (h) 12 water, 12 *n*-nonane, and 12 1-octanol. Color notation as in Figure 5.19.

For longer alcohols, this structural transformation also induces a more uniform dispersion of *n*-nonane molecules around this core-shell structure (see Figure 5.20f,h), forming an additional "onion-like" layer on the outside, in contrast to the one-sided deposition of *n*-nonane (which remained as an oil droplet) found for clusters containing shorter alcohols (see Figure 5.20b-d). Clearly, for the latter cases *n*-nonane molecules still prefer to interact with themselves rather than with the short nonpolar tails of either ethanol or 1-butanol. On the contrary, longer alcohols appear to act more effectively as an amphiphile, bringing water and *n*-nonane together to form a more symmetrical spherical structure. Thus, from the structural evolution depicted in Figure 5.20 it is tempting to suggest that the miscibility between water and *n*-nonane can be further improved by increasing the alcohol chain length.

Evidence of the enhanced miscibility between water and *n*-nonane in the presence of the longer alcohols comes from the composition analysis. It has been shown that the ternary nucleation of water/*n*-nonane/1-butanol behaves pretty much like a binary water/1-butanol system when a_2' is low, with *n*-nonane almost completely excluded from the critical clusters.[44] This was reflected by the average composition plots (see Figure 5.21), where the mole fraction of *n*-nonane was found to be very close to zero by both the simulation and the experiment[46] but the contributions of the other two components to the critical clusters stay nearly the same up to an a_2' value of 0.4 for the ternary water/*n*-nonane/1-butanol mixture. Similar results were also obtained for water/*n*-nonane/ethanol. In contrast, for longer alcohols continuous changes were observed in the average content of the critical nuclei over the same range of a_2'. In particular, with an increase of a_2' from 0 to 0.4, *n*-nonane emerges as a component that is no longer negligible in the nucleation process. In addition, its contribution to the critical nuclei improves steadily with the alcohol chain length (and could be even more significant if longer alcohols

were used). Such an enhanced *n*-nonane content is also accompanied by a slightly higher 1-butanol mole fraction and a lower water contribution to the critical cluster. From the composition results obtained at low a_2' conditions, one may speculate that the miscibility between water and *n*-nonane would continue to improve with a further increase of a_2'. However, an immediate complication is the appearance of another group of clusters, dominantly composed of *n*-nonane, which are already observed at a_2' = 0.5. In particular, for all cases shown in Figure 5.21, the composition plots revealed a revolutionary change at a_2' = 0.5 with *n*-nonane starting to replace

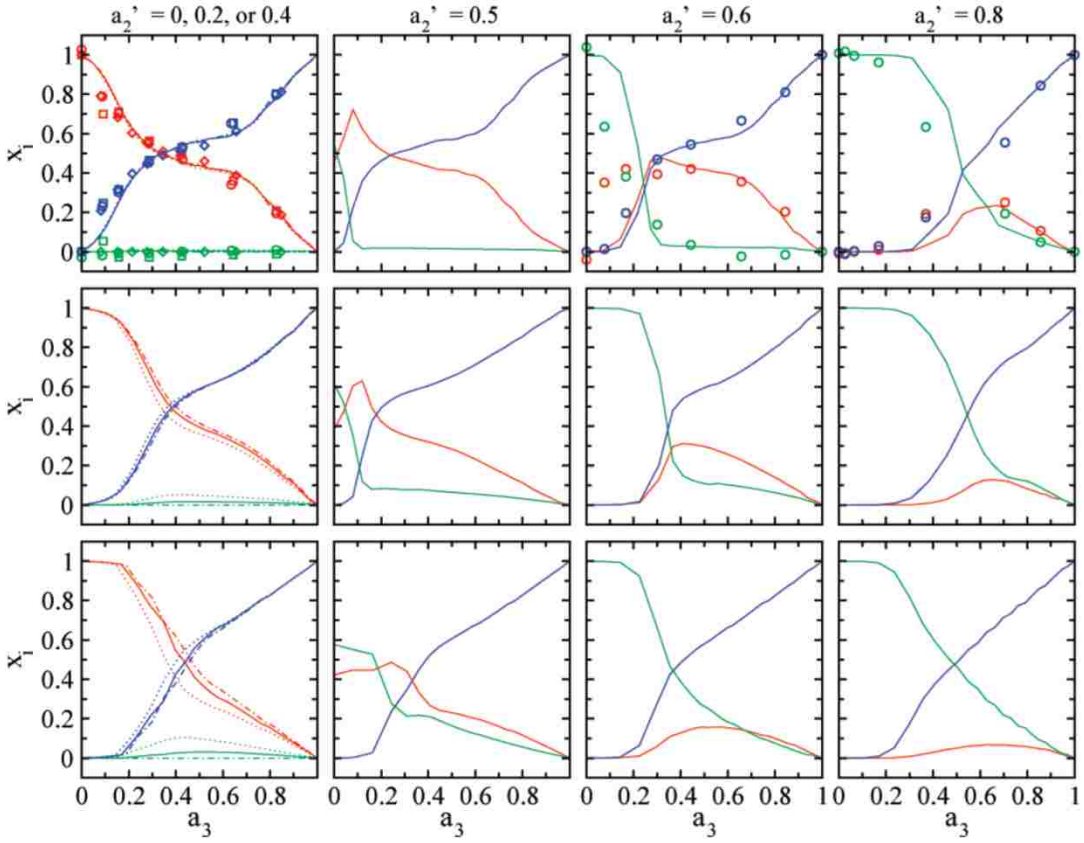

Figure 5.21. Average mole fraction of water (red), *n*-nonane (green), and 1-alcohol (blue) as a function of the normalized activity of 1-alcohol obtained at an value of 0 (diamonds and dashed-dotted lines), 0.2 (circles and solids lines), 0.4 (squares and dotted lines), and others as specified at the top of each column. The top, middle, and bottom panels represent the results obtained for the ternary systems involving 1-butanol, 1-hexanol, and 1-octanol, respectively. The experimental data[46] obtained for water/*n*-nonane/1-butanol are also included as symbols.

water as a major component in the critical nuclei (especially toward low a_3 conditions), whereas at the transition point roughly equal amounts of *n*-nonane and water could be found in the critical nuclei even when 1-alcohol is absent. As mentioned previously,[38, 52] a mole fraction close to 0.5 for both water and *n*-nonane observed at those conditions should not be used as a sign of miscibility between these two components. Rather, it is due to the formation of two major critical nuclei, one water-enriched and the other *n*-nonane-enriched. Intuitively, one can also rule out the possibility of forming fully mixed critical nuclei given that the mole fraction of *n*-nonane even decreases with the addition of alcohol to the critical nuclei (see Figure 5.21). This decrease is initially compensated by the increase of both water and 1-alcohol content. Eventually, the mole fraction of water goes down after reaching a maximum at a certain a_3 value. This feature stays qualitatively the same for higher conditions in the different systems examined here except that the water mole fraction decreases with increasing or with alcohol chain length. Therefore, it is generally expected that both water- and *n*-nonane-enriched critical clusters could coexist with each other at those conditions. As a result, the composition data plotted in Figure 5.21 may not be directly reflective of the miscibility for these cluster systems.

For those conditions where the average composition plots show the largest miscibility between the three components, the NFE contour maps were taken out specifically around the critical cluster size for a detailed view of the miscibility information between these three components. As shown in Figure 5.22, for conditions with below 0.4, only water-enriched critical clusters are present on these maps with the most probable compositions (colored in blue) centered around those average values shown in Figure 5.21. Thus, consistent with the average composition data, the increase of either the alcohol chain length or a_2' leads to a steady shift of this blue domain from the water/1-alcohol binary line to the inner region of this triangular

"nanophase diagram". Further increasing a_2' leads to the appearance of *n*-nonane-enriched critical clusters coexisting with water-enriched critical clusters (in accord with our expectation). Such external phase separation is already quite pronounced at a_2' = 0.5 with these diagrams displaying at least two separate blue domains (to represent these two types of most probable critical clusters). For water/*n*-nonane/1-butanol, the coexistence of these two cluster phases is also revealed at higher a_2' and appears to be a universal feature for those conditions as long as the average content of the critical nuclei suggests the substantial presence of all components. On the contrary, when the longer alcohols are used as the surfactant, a merging of these multiple phases into a fully mixed one, which still contains appreciable amount of all components, could occur at higher conditions (see the three diagrams located at the lower-right corner of Figure 5.22, each displaying essentially one major blue domain, although it is widely spread out and located close to the *n*-nonane/1-alcohol line). This provides direct support for the further improved miscibility between water and *n*-nonane in the presence of the longer alcohols. But among all the maps displayed in Figure 5.22, the most striking evidence for such enhanced miscibility is actually provided by the water/*n*-nonane/1-octanol system at an intermediate vapor-phase composition condition (i.e., at an a_2' value of 0.5), in which a blue domain emerged right around the center of the triangular "nanophase diagram". A more surprising feature of this NFE map is the coexistence of these fully mixed critical clusters with the other two major critical nuclei, enriched by either water or *n*-nonane (see the other two blue regions located at either the water or the *n*-nonane end). This is in sharp contrast to the rest, which show at most two major cluster phases in coexistence, with each phase typically enriched by one or two but rarely all three components, and thus implying an even more complex nucleation mechanism than previously described for multiple-component nucleation of this type.

To resolve the mechanistic details for this particular case, the NFEs were analyzed for both pre- and post critical clusters and these results are shown in Figure 5.23. It becomes apparent from these additional NFE maps that nucleation for this mixture originally proceeds through externally phase-separated clusters, especially those enriched almost exclusively by water (see the left NFE map obtained at a cluster size of 15 with the blue region located toward

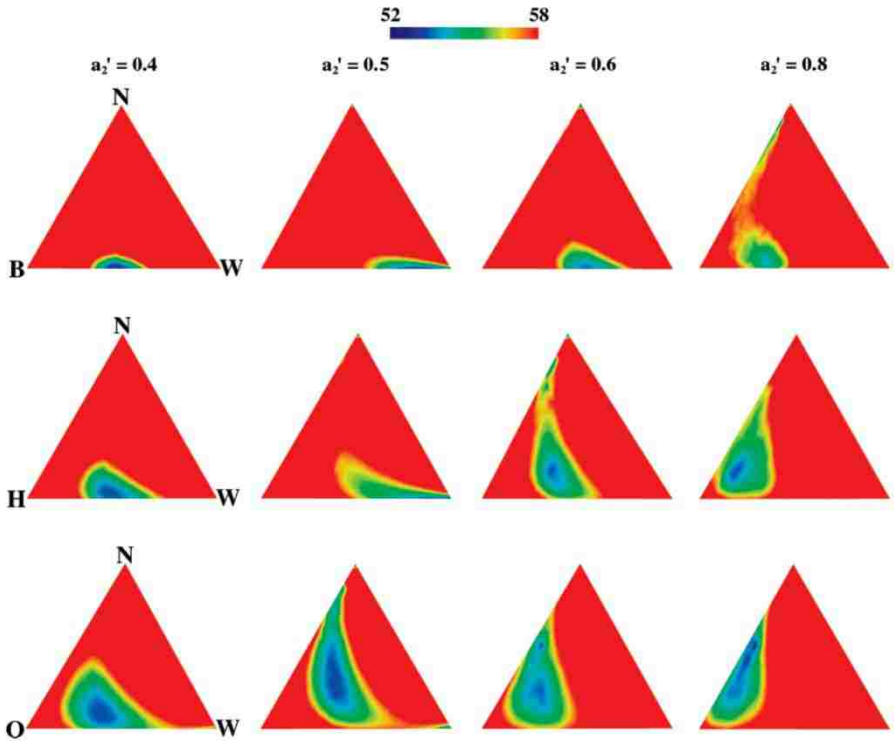

Figure 5.22. NFEs (in units of k_BT) as a function of cluster composition. The top four panels represent the results obtained for water/*n*-nonane/1-butanol (W/N/B), from left to right, at (a) a_1 = 0.41, a_2 = 0.27, a_3 = 0.40, and a cluster size of 42; (b) a_1 = 0.87, a_2 = 0.87, a_3 = 0.12, and a cluster size of 33; (c) a_1 = 0.61, a_2 = 0.91, a_3 = 0.25, and a cluster size of 30; and (d) a_1 = 0.19, a_2 = 0.78, a_3 = 0.62, and a cluster size of 42. The middle four panels represent the results obtained for water/*n*-nonane/1-hexanol (W/N/H), from left to right, at (a) a_1 = 0.62, a_2 = 0.42, a_3 = 0.40, and a cluster size of 27; (b) a_1 = 0.90, a_2 = 0.90, a_3 = 0.22, and a cluster size of 30; (c) a_1 = 0.60, a_2 = 0.90, a_3 = 0.36, and a cluster size of 24; and (d) a_1 = 0.17, a_2 = 0.68, a_3 = 0.65, and a cluster size of 27. The bottom four panels represent the results obtained for water/*n*-nonane/1-octanol (W/N/O), from left to right, at (a) a_1 = 0.74, a_2 = 0.49, a_3 = 0.40, and a cluster size of 21; (b) a_1 = 0.88, a_2 = 0.88, a_3 = 0.26, and a cluster size of 27; (c) a_1 = 0.42, a_2 = 0.63, a_3 = 0.48, and a cluster size of 21; and (d) a_1 = 0.15, a_2 = 0.58, a_3 = 0.60, and a cluster size of 21.

the water end in Figure 5.23). Although this map also indicates the presence of *n*-nonane-enriched clusters, their population is expected to be much smaller than the water-enriched ones given the exponential dependence of the population on the NFE value. The probability to observe fully mixed clusters at this cluster size is even lower as the center region of this diagram shows significantly higher NFE values than either the water or the *n*-nonane side. However, with increasing cluster size, the relative thermodynamic stability of these fully mixed clusters versus those phase-separated ones improves continuously. As already shown by the NFE map in Figure 5.22, around the critical cluster size the occurrence frequency for these mixed clusters becomes roughly comparable to the phase-separated ones at this condition. Further increasing the cluster size favors this fully mixed clusters even more and eventually makes them the dominant type of clusters on the nucleation landscape (see the right NFE map obtained at a post critical cluster size of 39 in Figure 5.23).

It should be noted that such a steadily improved stability for the fully mixed clusters with increasing size is expected from the structural evolution depicted in Figure 5.20 and the fact that the number of alcohol molecules contained by these clusters is directly proportional to the cluster size. As shown by Figure 5.20g, with the number of alcohol molecules too low to cover the water droplet, small fully mixed clusters (with a size of 15 or below) adopt a “dumbbell” motif. Although this structure allows the alcohol molecules to interact fully with both water and *n*-nonane, the exposure of the water surface to the outside is extremely unfavorable for the overall stability (due to the large surface tension and surface free energy penalties). Clearly the core-shell structure (as shown in Figure 5.20h) is better in this regard (and thus more stable) but is only a viable form for larger clusters when enough alcohol molecules are present. Correspondingly, with increasing cluster size, fully mixed clusters evolve from a “dumbbell-

like" structure to a dominantly core-shell motif. The significantly improved thermodynamic stability from such a structural transition is therefore directly in coherence with the dramatic evolution of those "nanophase diagrams" shown in Figure 5.23.

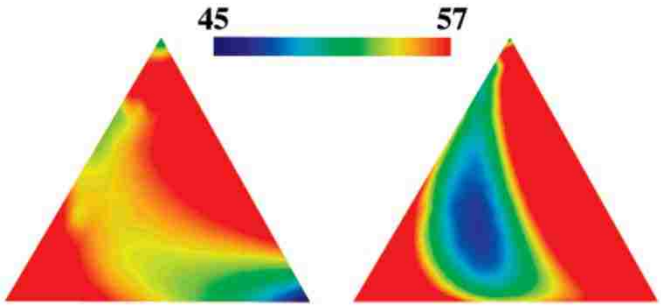

Figure 5.23. NFEs (in units of k_BT) as function of cluster composition obtained for the water/*n*-nonane/1-octanol system at a_1 = 0.88, a_2 = 0.88, and a_3 = 0.26 for precritical clusters consisting of 15 molecules (left) or post critical clusters of 39 molecules (right).

Further support for this structural transformation comes from the density profiles (see Figure 5.24). Inspired by the "dumbbell" motif, these probability density profiles were analyzed using the following procedure. First, the center of mass (COM) was calculated separately for the two droplets formed by either water or *n*-nonane molecules. Then an axis (denoted as the "z"-axis in Figure 5.24) was created by linking these two COMs, with its origin fixed at the COM of the water droplet and its positive side pointing to the COM of the *n*-nonane droplet. Finally, the probability density of each atom type was computed and normalized along this "z"-axis. For each cluster of a given size and composition, about 100 independent configurations were used to obtain the data shown in Figure 5.24. As evident for small clusters the density profiles display the type of separation expected for a dumbbell motif, with the peak moving from left to right for the water oxygen, 1-octanol oxygen, 1-octanol carbon, and *n*-nonane carbon (see Figure 5.24a). In addition, the left-side of the water droplet is almost fully exposed to the outside. Only occasionally would one or two *n*-nonane molecules dangle away from the *n*-nonane droplet to

interact with the water molecules (see Figure 5.24a,e), which causes the long tailing of the *n*-nonane carbon density profile into the negative side of the *z*-axis. Although these density distributions were found to be highly unsymmetrical with respect to the COM of the water droplet at small cluster sizes, they were more or less centered for larger clusters containing 30 molecules or more (see Figure 5.24b), which is a sign of the core-shell motif with a more uniform surrounding of the water droplet by other species (see Figure 5.20h as compared to Figure 5.20g). Additional evidence of this core-shell motif was provided by the radial density profiles. Again in the analysis of these density distributions, the origin was placed at the COM of the water droplet. As evident from Figure 5.24c, the core region is exclusively occupied by the water molecules. Away from this inner core, 1-octanol oxygen is the first heavy atomic species to appear, followed by 1-octanol carbon and then *n*-nonane carbon. Given the amount of overlap in the density profiles, it is clear that water and *n*-nonane are barely in direct contact with each other but rather are connected through the intermediate surfactant layer of 1-octanol, thus ultimately confirming the "onion-like" core-shell structure formed by the larger clusters.

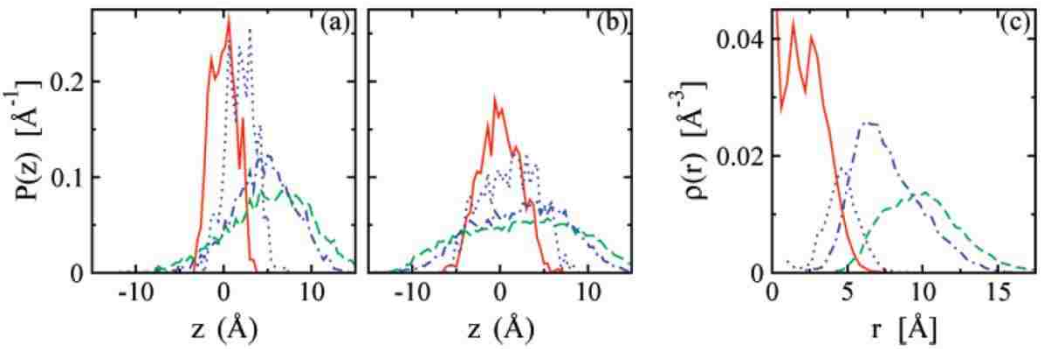

Figure 5.24. Probability density profiles along the *z*-axis obtained for water oxygen (red solid), 1-octanol oxygen (blue dotted), 1-octanol carbon (blue dashed-dotted), and *n*-nonane carbon (green dashed). Panels a and b represent the results obtained for fully mixed clusters containing a total of 15 and 39 molecules, respectively. Shown in panel c are the radial density profiles obtained for the larger clusters of 39 molecules.

5.3.3.4 Implications of the Core-Shell Structure on Atmospheric Organic Aerosols and Beyond

The results obtained here are expected to have important implications for atmospheric organic nanodroplets. Being close models for those atmospheric systems, the core-shell structure and the related results/concepts (such as mutual nucleation enhancement) discovered here for water/*n*-nonane/1-alcohol are likely transferable to the aqueous organic aerosols formed in the atmosphere. In fact, such an "inverted micelle" structure has already been proposed to account for the high organic content found in many types of atmospheric aerosols, which would be otherwise inexplicable based on bulk solubilities.[121] This structure can be further linked to the cloud albedo enhancement through the surface tension reduction mechanism, an effect that would be largely missing in predictions yielded by the classical homogeneous, continuum model.[131] The small angle neutron scattering experiments[119] have recently provided some direct evidence of the formation of the core-shell structure for nanodroplets formed by water and 1-butanol, whereas this current work further suggests that the core-shell structure formed by longer alcohols (such as 1-octanol) or surfactants (which are more typical components for atmospheric aerosols) can lead to the formation of an additional organic layer to wrap around this structure. This interesting finding has added some new meaning to this "inverted micelle" picture. For example, this core-shell structure may serve as a natural condenser for collecting and concentrating those relatively nonpolar organic compounds. As a result, organic aerosols are a potential transport vehicle for these water insoluble compounds in the atmospheric environment.[121] Also the greatly enhanced local concentration of organic materials is expected to improve substantially the rate of chemical transformation for those species that are mutually reactive with each other. On an entirely different topic, this core-shell structure coated by an additional "insulating" layer may be an ideal motif for encapsulation applications, e.g., to gain an

optimal control of particle agglomeration and correspondingly particle size, important in the processing of nanomaterials.[134]

5.3.4 Concluding Remarks

An extensive vapor-liquid nucleation study was carried out on the ternary water/*n*-nonane/1-alcohol ($C_iH_{2i+1}OH$) mixtures with i = 2, 4, 6, and 8. It was found from the onset activity results that all these systems exhibit the type of non-ideal nucleation behavior that was previously discovered by experiments on the water/*n*-nonane/1-butanol mixture. However, there are subtle but important differences in the microscopic details with respect to the miscibility and structures formed by these three components. Specifically, for systems involving shorter alcohols (e.g., ethanol and 1-butanol), the most probable clusters found throughout the entire range of vapor-phase composition conditions are enriched by either water or *n*-nonane but not both. In contrast, for systems involving longer alcohols (1-hexanol and 1-octanol), we were able to locate appropriate conditions under which the nucleation pathways pass through critical nuclei that contain substantial amount of all three components. In fact, for water/*n*-nonane/1-octanol at an intermediate gas-phase activity composition, fully mixed clusters with a roughly equal molar amount of water, *n*-nonane, and 1-octanol appear as a major group of clusters on the nucleation landscape. Structural analysis revealed the microscopic origin for the enhanced miscibility observed between water and *n*-nonane, the formation of the core-shell (water-alcohol) structure. For example, this core-shell structure prepares a nonpolar surface that is more attractive for the adsorption of the purely nonpolar *n*-nonane than the original bare water surface. When 1-hexanol and 1-octanol are used, this core-shell structure induces a rather uniform dispersion of the *n*-nonane molecules at the outside that allows them to fully interact with the alkyl tail of the alcohol molecules. This compares favorably to the one-sided deposition of *n*-nonane found for

clusters containing shorter alcohols, which remain as oil droplets fully segregated from the water molecules, consistent with the calculated miscibility data. This new finding of additional organic layers at the outside of the core-shell structure has important implications to other multicomponent nanodroplets, from encapsulation of nanomaterials to the transport of organic materials via atmospheric organic aerosols. Some of these results are testable experimentally given that the experimental measurements have been previously performed on mixtures containing water, *n*-nonane, and 1-butanol.

Chapter 6. Where Are the Water Molecules on Mars?

For over a century, various investigations have been carried out to search for the evidence of water on Mars because this would suggest that the planet Mars is capable of supporting life. These researches have led to a consensus view that water molecules are present on Mars. The Martian atmosphere is mostly composed of carbon dioxide and hints of water and methane.[135-141] It was recently reported that water molecules were found in the Southern Mid-Latitudes of Mars in large glaciers. As reported recently, water molecules were found in the Southern Mid-Latitudes of Mars as massive water ice.[135] Were all the water molecules on Mars accounted for?

Nucleation plays a vital role in many atmospheric and technological processes. In particular, vapor-liquid nucleation provides understanding of how liquid phases are formed from gaseous components of the atmosphere. It has been suggested that the Martian atmosphere could only support simple atmospheric processes but the difficulty and expense of experiments on Mars makes this difficult to verify.[67] In this work, we employed a combination of aggregation-volume-bias Monte Carlo and umbrella sampling (see Chapter 2) to simulate nucleation in a Martian atmosphere and gain insight into the fate of atmospheric water.

To mimic Martian conditions, simulations were done at extreme temperatures recorded on Mars using known components of Mars' atmosphere such as carbon dioxide, water, and methane. Here we found out that at 300K, at all reasonable cluster sizes, the three component gases nucleate independently, that is, individual components tend to cluster among themselves. In this particular case, self-association interactions (i.e. water-

water) are stronger than cross-association interaction (i.e. water-carbon dioxide). For the 130K case, representing the surface temperature of Mars, the scenario seems extraordinary. As shown in Figure 1a-1d, the molecules belonging to the same component still cling to each other forming different cores. These cores apparently are within one single cluster. This apparent core/shell structure is conserved from small to bigger clusters. The onion type structural motif shown here could only be made as a result of water being trapped during the process of carbon dioxide and methane crystallization. As such, evaporation of carbon dioxide and methane could lead to a phenomenon observed in the Southern Mid-Latitudes of Mars,[135] exposed water ice.

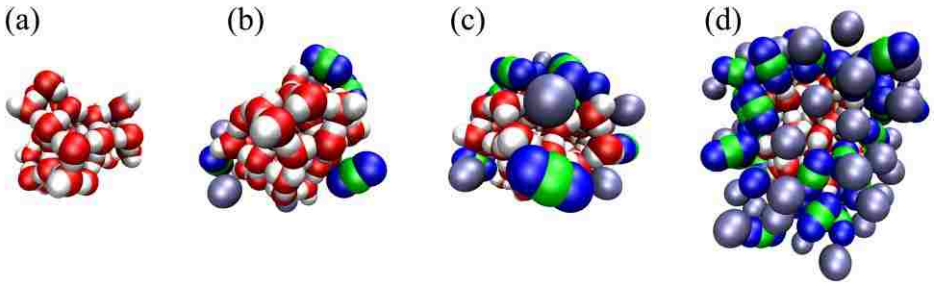

Figure 6.1. Representative configurations of various clusters containing (a) 40 molecules of water, (b) 5 molecules of carbon dioxide, 5 molecules of methane, and 40 molecules of water, (c) 10 molecules of carbon dioxide, 10 molecules of methane, and 40 molecules of water, and (d) 40 each of carbon dioxide, water, and methane molecules. Color notation: water oxygen (red), carbon dioxide oxygen (blue), polar hydrogen (gray), carbon (green), and methane (ice blue).

Based on the radial density profile (see Figure 2), 3 distinct cores are evident. Water, carbon dioxide, and methane molecules are located in the inner core, middle core, and outer core, respectively. Indeed an internal phase separation is apparent.

Interestingly, carbon dioxide and methane has appreciable mixing towards the surface of the cluster. This profile further supports the theory that water on the surface of Mars could be hidden within the carbon dioxide glaciers.

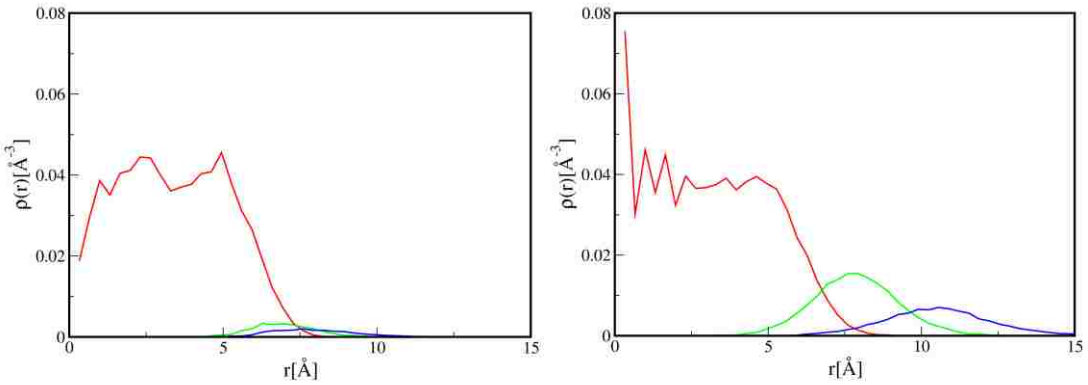

Figure 6.2. Radial density profiles of clusters containing (a) 5 molecules of carbon dioxide, 5 molecules of methane, and 40 molecules of water, and (b) 40 each of carbon dioxide, water, and methane molecules. Color notation: water oxygen (red), carbon dioxide carbon (green), and methane (blue).

In summary, we offer a reasonable structural motif that suggests the possible presence of water on Mars' surface. In a ternary nucleation simulation of carbon dioxide, water, and methane, it was found that these three species can come together, forming a single cluster. Though further analysis must be done, our initial guess points to the homogeneous nucleation of water as initiator for the enhanced mixing of these three components (see Figure 1). Within the cluster size range investigated here, these fully mixed clusters display a common structural motif that is core-shell like. Namely, water molecules form a tightly bounded core, which is embedded inside a carbon dioxide – methane cage.

References

1. Kashchiev, D.; *Nucleation: Basic Theory with Applications*, Butterworth and Heinemann: Oxford, **2000** and references therein.

2. Spracklen, D. V.; Carslaw, K. S.; Kulmala, M.; Kerminen, V-M.; Mann, G. W.; Sihto, S-L.; "The contribution of boundary layer nucleation events to total particle concentrations on regional and global scales" *Atmospheric Chemistry and Physics* **2006**, 6, 5631-5648.

3. Fenelonov, V. B.; Kodenyov, G. C.; Kostrovsky, V. G.; "On the dependence of surface tension of liquids on the curvature of the Liquid-Vapor Interface" *J. Phys. Chem. B* **2001**, 105, 1050-1055.

4. Weber, R. J.; McMurry, P. H.; Mauldin, R. L.; Tanner, D. J.; Eisele, F. L.; Clarke, A. D.; Kapustin, V. N.; "New particle formation in the remote troposphere: a comparison of observations at various sites" *Geophys. Res. Lett.* **1999**, 26, 307-310.

5. Kulmala, M.; "Atmospheric science: How particles nucleate and grow" *Science* **2003**, 302, 1000-1001.

6. Schmelzer, J. W. P. (Editor); *Nucleation Theory and Applications*, Wiley-VCH Verlag GmbH & Co.: Weinheim, **2005**.

7. Volmer, M.; Weber, A.; "Nucleus formation in supersaturated systems" *Z. Physik. Chem.* **1926**, 119, 277-301.

8. Becker, R.; Döring, W; "Kinetische Behandlung der Keimbildung in ű̈bersättigten Dämpfen" *Ann. Phys.* (Leipzig), **1935**, 24, 719-752.

9. Hruby, J.; Viisanen, Y.; Strey, R.; "Homogeneous nucleation rates for *n*-pentanol in argon: Determination of the critical cluster size" *J. Chem. Phys.* **1996**, 104, 5181-5187.

10. Luijten, C. C. M.; Baas, O. D. E.; van Dongen, M. E. H.; "Homogeneous nucleation rates for *n*-pentanol from expansion wave tube experiments" *J. Chem. Phys.* **1997**, 106, 4152-4156.

11. Bertelsmann, A.; Heist, R. H.; "Nucleation of 1-Pentanol Using a Thermal Diffusion Cloud Chamber" *Aerosol Sci. Technol.* **1998**, 28, 259-268.

12. Zdimal, V.; Smolik, J.; "Homogeneous nucleation rate measurements in 1-pentanol vapor with helium as a buffer gas" *Atmos. Res.* **1998**, 46, 391-400.

13. Rudek, M. M.; Katz, J. L.; Vidensky, I. V.; Zdimal, V.; Smolik, J.; "Homogeneous nucleation rates of *n*-pentanol measured in an upward thermal diffusion cloud chamber" *J. Chem. Phys.* **1999**, 111, 3623-3629.

14. Anisimov, M. P.; Hopke, P. H.; Shandakov, S. D.; Shvets, I. I.; "*n*-Pentanol-helium homogeneous nucleation rates" *J. Chem. Phys.* **2000**, 113, 1971-1975.

15. Graβmann, A.; Peters, F.; "Homogeneous nucleation rates of *n*-pentanol in nitrogen measured in a piston-expansion tube" *J. Chem. Phys.* **2000**, 113, 6774-6781.

16. Ferguson, F. T.; Heist, R. H.; Nuth III, J. A.; "The effect of carrier gas pressure and wall heating on the operation of the thermal diffusion cloud chamber" *J. Chem. Phys.* **2001**, 115, 10829-10836.

17. Lihavainen, H.; Viisanen, Y.; Kulmala, M.; "Homogeneous nucleation of *n*-pentanol in a laminar flow diffusion chamber" *J. Chem. Phys.* **2001**, 114, 10031-10038.

18. Schmitt, J. L.; Doster, J. G.; "Homogeneous nucleation of *n*-pentanol measured in an expansion cloud chamber" J. Chem. Phys. **2002**, 116, 1976-1978.

19. Iland, K.; Wedekind, J.; Wolk, J.; Wagner, P. E.; Strey, R.; "Homogeneous nucleation rates of 1-pentanol" *J. Chem. Phys.* **2004**, 121, 12259-12264.

20. Gharibeh, M.; Kim, Y.; Dieregsweiler, U.; Wyslouzil, B.; Ghosh, D.; Strey, R.; "Homogeneous nucleation of *n*-propanol, *n*-butanol, and *n*-pentanol in a supersonic nozzle" *J. Chem. Phys.* **2005**, 122, 094512-(1-9).

21. Stauffer, D.; "Kinetic theory of two-component ("hetero-molecular") nucleation and condensation" *J. Aerosol Sci.* **1976**, 7, 319-333.

22. Wilemski, G.; "Revised classical binary nucleation theory for aqueous alcohol and acetone vapors" *J. Phys. Chem.* **1987**, 91, 2492-2498.

23. Jaecker-Voirol, A.; Mirabel, P.; Reiss, H.; "Hydrates in supersaturated binary sulfuric acid-water vapor: A reexamination" *J. Chem. Phys.* **1987**, 87, 4849-4852.

24. Noppel M.; "Binary nucleation of water–sulfuric acid system: A reexamination of the classical hydrates interaction model" *J. Chem. Phys.* **1998**, 109, 9052-9056.

25. Zeng, X. C.; Oxtoby, D. W.; "Gas-liquid nucleation in Lennard-Jones fluids" *J. Chem. Phys.* **1991**, 94, 4472-4478.

26. Talanquer, V.; Oxtoby, D. W.; "Critical clusters in binary mixtures: A density functional approach" *J. Chem. Phys.* **1996**, 104, 1993-1999.

27. Oxtoby, D. W.; "Nucleation of First-Order Phase Transitions" *Acc. Chem. Res.* **1998**, 31, 91-97.

28. Napari, I.; Laaksonen, A.; "Gas–liquid nucleation in partially miscible systems: Free-energy surfaces and structures of nuclei from density functional calculations" *J. Chem. Phys.* **1999**, 111, 5485-5490.

29. Wyslouzil, B. E.; Heath, C. H.; Cheung, J. L.; Wilemski, G.; "Binary condensation in a supersonic nozzle" *J. Chem. Phys.* **2000**, 113, 7317-7329.

30. ten Wolde, P. R.; Frenkel, D.; "Computer simulation study of gas-liquid nucleation in a Lennard-Jones system" *J. Chem. Phys.* **1998**, 109, 9901-9918.

31. ten Wolde, P. R.; Frenkel, D.; "Numerical study of gas–liquid nucleation in partially miscible binary mixtures" *J. Chem. Phys.* **1998**, 109, 9919-9927.

32. Oh, K. J.; Zeng, X. C.; "A small-system ensemble Monte Carlo simulation of supersaturated vapor: Evaluation of barrier to nucleation" *J. Chem. Phys.* **2000**, 112, 294-300.

33. Yoo, S.; Oh, K. J.; Zeng, X. C.; "Monte Carlo simulation of homogeneous binary vapor–liquid nucleation: Mutual enhancement of nucleation in a partially miscible system" *J. Chem. Phys.* **2001**, 115, 8518-8524.

34. Kusaka, I.; Wang, Z. -G.; Seinfeld, J. H.; "Direct evaluation of the equilibrium distribution of physical clusters by a grand canonical Monte Carlo simulation" *J. Chem. Phys.* **1998**, 108, 3416-3423.

35. Kusaka, I.; Oxtoby, D. W.; "Identifying physical clusters in vapor phase nucleation" *J. Chem. Phys.* **1999**, 110, 5249-5261.

36. Chen, B.; Siepmann, J. I.; Oh, K. J.; Klein, M. L.; "Aggregation-volume-bias Monte Carlo simulations of vapor-liquid nucleation barriers for Lennard-Jonesium" *J. Chem. Phys.* **2001**, 115, 10903-10913.

37. Chen, B.; Siepmann, J. I.; Oh, K. J.; Klein, M. L.; "Simulating vapor-liquid nucleation of *n*-alkanes" *J. Chem. Phys.* **2002**, 116, 4317-4329.

38. Chen, B.; Siepmann, J. I.; Klein, M. L.; "Simulating the nucleation of water/ethanol and water/*n*-nonane mixtures: Mutual enhancement and two-pathway nucleation" *J. Am. Chem. Soc.* **2003**, 125, 3113-3118.

39. Chen, B.; Siepmann, J. I.; Klein, M. L.; "Simulating Vapor-Liquid Nucleation of water: A Combined Histogram-Reweighting and Aggregation-Volume-Bias Monte Carlo Investigation for Fixed-Charged and Polarizable Models" *J. Phys. Chem. A* **2005**, 109, 1137-1145.

40. Nellas, R. B.; McKenzie, M. E.; Chen, B.; "Probing the Nucleation Mechanism for the Binary *n*-Nonane/1-Alcohol Series with Atomistic Simulations" *J. Phys. Chem. B* **2006**, 110, 18619-18628.

41. Chen, B.; Kim, H.; Keasler, S. J.; Nellas, R. B.; "An aggregation-volume-bias Monte Carlo investigation on the condensation of a Lennard-Jones vapor and crystal nucleation in cluster systems: An in-depth evaluation of the classical nucleation theory" *J. Phys. Chem. B* **2008**, 112, 4067-4078.

42. Chen, B.; Nellas, R. B.; Keasler, S. J.; "Fractal aggregates in protein crystal nucleation" *J. Phys. Chem. B* **2008**, 112, 4725-4730.

43. Kathmann, S. M.; Schenter, G. K.; Garrett, B. C.; Chen, B.; Siepmann, J. I.; "Thermodynamics and Kinetics of Nanoclusters Controlling Gas-to-particle Nucleation" *J. Phys. Chem. C* **2009**, 113, 10354–10370.

44. Nellas, R. B.; Chen, B.; "Towards understanding the nucleation mechanism for multi-component systems: An atomistic simulation of the ternary nucleation of water/*n*-nonane/1-butanol" *Phys. Chem. Chem. Phys*. **2008**, 10, 506-514.

45. Nellas, R. B.; Keasler, S. J.; Chen, B.; "Molecular content and structure of aqueous organic nanodroplets from the vapor-liquid nucleation study of the water/*n*-nonane/1-alcohol series" *J. Phys. Chem. A* **2008**, 112, 2930-2939.

46. Viisanen, Y.; Strey, R.; "Composition of critical clusters in ternary nucleation of water–*n*-nonane–*n*-butanol" *J. Chem. Phys.* **1996**, 105, 8293-8299.

47. Viisanen, Y.; Strey, R.; Laaksonen, A.; Kulmala, M.; "Measurement of the molecular content of binary nuclei. II. Use of the nucleation rate surface for water-ethanol" *J. Chem. Phys.* **1994**, 100, 6062-6072.

48. Strey, R.; Viisanen, Y.; "Measurement of the molecular content of binary nuclei. Use of the nucleation rate surface for ethanol-hexanol" *J. Chem. Phys.* **1993**, 99, 4693-4704.

49. Oxtoby, D. W.; Kashchiev, D.; "A general relation between the nucleation work and the size of the nucleus in multicomponent nucleation" *J. Chem. Phys.* **1994**, 100, 7665-7671.

50. Ford, I. J.; "Thermodynamical properties of critical clusters from measurements of vapour-liquid homogeneous nucleation rates" *J. Chem. Phys.* **1996**, 105, 8324-8332.

51. Nellas, R. B.; Chen, B.; Siepmann, J. I.; "Dumbbells and Onions in Ternary Nucleation" *Phys. Chem. Chem. Phys*. **2007**, 9, 2779-2781.

52. McKenzie, M. E.; Chen, B.; "Unravelling the peculiar nucleation mechanisms for non-ideal binary mixtures with atomistic simulations" *J. Phys. Chem. B* **2006**, 110, 3511-3516.

53. Oxtoby, D. W.; Laaksonen, A.; "Some consequences of the nucleation theorem for binary fluids" J. *Chem. Phys.* **1995**, 102, 6846-6850.

54. Talanquer, V.; Oxtoby, D. W.; "Nucleation in the presence of an amphiphile: A density functional approach" *J. Chem. Phys.* **1997**, 106, 3673-3680.

55. Chen, B.; Siepmann, J. I.; "A novel Monte Carlo algorithm for simulating strongly associating fluids: Applications to water, hydrogen fluoride, and acetic acid" *J. Phys. Chem. B* **2000**, 104, 8725-8734.

56. Chen, B.; Siepmann, J. I.; "Improving the efficiency of the aggregation-volume-bias Monte Carlo algorithm" *J. Phys. Chem. B* **2001**, 105, 11275-11282.

57. Chen, B.; *Phase Equilibria of Hydrocarbons, Alcohols, Water, and Their Mixtures*, Ph.D. Thesis, University of Minnesota, **2001**.

58. Torrie, G. M.; Valleau, J. P.; "Monte Carlo Free Energy Estimates using Non-Boltzmann Sampling: Application to the Sub-Critical Lennard-Jones Fluid" *Chem. Phys. Lett.* **1974**, 28, 578-581.

59. Wilding, N. B.; "Critical-point and coexistence-curve properties of the Lennard-Jones fluid: A finite-size scaling study" *Phys. Rev. E* **1995**, 52, 602-611.

60. Potoff, J. J.; Panagiotopoulos, A. Z.; "Critical point and phase behavior of the pure fluid and a Lennard-Jones Mixture" *J. Chem. Phys.* **1998**, 109, 10914-10920.

61. Ferrenberg, A. M.; Swendsen, R. H.; "New Monte-Carlo Technique for Studying Phase-Transitions" *Phys. Rev. Lett.* **1998**, 61, 2635-2638.

62. Ferrenberg, A. M.; Swendsen, R. H.; "Optimized Monte-Carlo Data-Analysis" *Phys. Rev. Lett.* **1989**, 63, 1195-1198.

63. Swendsen, R. H.; "Modern Methods of Analyzing Monte-Carlo Computer-Simulations" *Physica A* **1993**, 194, 53-62.

64. Allen, M. P.; Tildesley, D. J.; *Computer Simulation of Liquids*, Oxford University Press: Oxford, **1987**.

65. Frenkel, D; Smit, B.; *Understanding Molecular Simulations: From Algorithms to Applications* 2nd Edition, Academic Press: San Diego, **2002**.

66. Smolik, J.; Wagner, P. E.; *Nucleation and Atmospheric Aerosols*, edited by M. Kulmala and P.E. Wagner (Pergamon, Helsinki, Finland, **1996**), p.58.

67. Määttänen, A.; Vehkamäki, H.; Lauri, A.; Merikallio, S.; Kauhanen, J.; Savijärvi, H.; Kulmala, M.; "Nucleation studies in the Martian atmosphere" *J. Geophys. Res.* **2005**, 110, E02002-(1-12).

68. Vehkamäki, H.; *Classical Nucleation Theory in Multicomponent Systems*, Springer, Berlin Heidelberg, **2006**.

69. Volmer, M.; Kinetic der Phasenbildung; Steinkopff: Dresden, **1939**.

70. Reiss, H.; "The Kinetics of Phase Transitions in Binary Systems" *J. Chem. Phys.* **1950**, 18, 840-848.

71. Laaksonen, A.; Talanquer, V.; Oxtoby, D. W.; "NUCLEATION: Measurements, Theory, and Atmospheric Applications" *Annu. Rev. Phys. Chem.* **1995**, 46, 489-524.

72. Girschik, S. L.; Chiu, C.-P.; "Kinetic nucleation theory: A new expression for the rate of homogeneous nucleation from an ideal saturated vapor" *J. Chem. Phys.* **1990**, 93, 1273-1277.

73. Dillman, A.; Meier, G. E. A.; "A refined droplet approach to the problem of homogeneous nucleation from vapor phase" *J. Chem. Phys.* **1991**, 94, 3872-3884.

74. Reiss, H.; Kegel, W. K.; Katz, J. I.; "Resolution of the problems of replacement free energy, 1/S, and internal consistency in nucleation theory by consideration of the length scale for mixing entropy" *Phys. Rev. Lett.* **1997**, 78, 4506-4509.

75. Reguera, D.; Ruby, J. M.; "Nonequilibrium translational-rotational effects in nucleation" *J. Phys. Chem.* **2001**, 115, 7100-7106.

76. Kashchiev, D.; "On the relation between nucleation work, nucleus size, and nucleation rate" *J. Chem. Phys.* **1982**, 76, 5098-5102.

77. Ford, I. J.; "Nucleation theorems, the statistical mechanics of molecular clusters, and a revision of classical nucleation theory" *Phys. Rev. E* **1997**, 56, 5615-5629.

78. Bowles, R. K.; McGraw, R.; Schaaf, P.; Senger, B.; Voegel, J.; Reiss, H; "A molecular based derivation of the nucleation theorem" J. Chem. Phys. 2000, 113, 4524-4532.

79. Siepmann, J. I.; Frenkel, D.; "Configurational-bias Monte Carlo – A new sampling scheme for flexible chains" *Mol. Phys.* **1992**, 75, 59-70.

80. Frenkel, D.; Mooij, G. C. A. M.; Smit, B.; "Novel scheme to study structural and thermal properties of continuously deformable molecules" *J. Phys.: Cond. Matt.* **1992**, 4, 3053-3076.

81. Martin, M. G.; Siepmann, J. I.; "Transferable potentials for phase equilibria. 1. United-atom description of *n*-alkanes" *J. Phys. Chem. B* **1998**, 102, 2569-2577.

82. Senger, B.; Schaaf, P.; Corti, D. S.; Bowles, R.; Voegel, J. -C.; Reiss, H.; "A molecular theory of the homogeneous nucleation rate. I. Formulation and fundamental issues" *J. Chem. Phys.* **1999**, 110, 6421-6437.

83. Hill, T. L.; Statistical Mechanics: Principles and Selected Applications, McGraw-Hill, New York, **1956**.

84. Stillinger, F. H.; "Rigorous Basis of the Frenkel-Band Theory of Association Equilibrium" *J. Chem. Phys.* **1963**, 38, 1486-1494.

85. Abraham, F. F.; "Monte Carlo simulation of physical clusters of water molecules" *J. Chem. Phys.* **1974**, 61, 1221-1225.

86. Schaaf, P.; Senger, B.; Voegel, J. -C.; Reiss, H; "Extended (*n*/*v*)-Stillinger cluster for use in the theory of homogeneous nucleation" *Phys. Rev. E* **1999**, 60, 771-778.

87. Schenter, G. K.; Kathmann, S. M.; Garrett, B. C.; "Dynamical Nucleation Theory: A New Molecular Approach to Vapor-Liquid Nucleation" *Phys. Rev. Lett.* **1999**, 82, 3484-3487.

88. Harris, S. A.; Ford, I. J.; "A dynamical definition of quasibound molecular clusters" *J. Chem. Phys.* **2003**, 118, 9216-9223.

89. Metropolis, N.; Rosenbluth, A. W.; Rosenbluth, M. N.; Teller, A. H.; Teller, E.; "Equation of state calculations by fast computing machines" *J. Chem. Phys.* **1953**, 21, 1087-1092.

90. Busch, N. A.; Wertheim, M. S.; Chiew, Y. C.; Yarmush, M. L.; "A Monte Carlo method for simulating associating fluids" *J. Chem. Phys.* **1994**, 101, 3147-3156.

91. Busch, N. A.; Wertheim, M. S.; Yarmush, M. L.; "Monte Carlo simulation of n-member associating fluids: application to antigen-antibody systems" *J. Chem. Phys.* **1996**, 104, 3962-3975.

92. Tsangaris, D. M.; de Pablo, J. J.; "Bond-bias simulation of phase equilibria for strongly associating fluids" *J. Chem. Phys.* **1994**, 101, 1477-1489.

93. Visco, D. P.; Kofke, D. A.; "Vapor-liquid equilibria and heat effects of hydrogen fluoride from molecular simulation" *J. Chem. Phys.* **1998**, 109, 4015-4027.

94. Visco, D. P.; Kofke, D. A.; "Modeling the Monte Carlo simulation of associating fluids" *J. Chem. Phys.* **1999**, 110, 5493-5502.

95. Merikanto, J.; Zapadinsky, E.; Lauri, A.; Vehkamaki, H.; "Origin of the failure of classical nucleation theory: Incorrect description of the smallest clusters" *Phys. Rev. Lett.* **2007**, 98, 145702.

96. Hale, B. N.; "The Scaling of Nucleation Rates" *Metall. Trans. A – Physical Metallurgy and Materials Science* **1992**, 23, 1863-1868.

97. Hale, B. N.; DiMattio, D. J.; "Scaling of the nucleation rate and a Monte Carlo discrete sum approach to water cluster free energies of formation" *J. Phys. Chem. B* **2004**, 108, 19780-19785.

98. Kathmann, S. M.; Schenter, G. K.; Garrett, B. C.; "Understanding the sensitivity of nucleation kinetics: A case study on water" *J. Chem. Phys.* **2002**, 116, 5046-5057.

99. Kathmann, S. M.; "Understanding the chemical physics of nucleation" *Theor. Chem. Acc.* **2006**, 116, 169-182.

100. McGraw, R.; Laaksonen, A.; "Scaling properties of the critical nucleus in classical and molecular-based theories of vapor-liquid nucleation" *Phys. Rev. Lett.* **1996**, 76, 2754-2757.

101. Anisimov, M. P.; Koropchak, J. A.; Nasibulin, A. G.; Timoshina, L. V.; "Critical embryo phase transitions in the nucleated binary glycerin–carbon dioxide system" *J. Chem. Phys.* **1998**, 109, 10004-10010.

102. McGraw, R.; Laaksonen, A.; "Interfacial curvature free energy, the Kelvin relation, and vapor-liquid nucleation rate" *J. Chem. Phys.* **1997**, 106, 5284-5287.

103. van Meel, J. A.; Page, A. J.; Sear, R. P.; Frenkel, D.; "Two-step vapor-crystal nucleation close below triple point" *J. Chem. Phys.* **2008**, 129, 204505.

104. Stubbs, J. M.; Siepmann, J. I.; "Aggregation in Dilute Solutions of 1-Hexanol in *n*-Hexane: A Monte Carlo Simulation Study" *J. Phys. Chem. B* **2002**, 106, 3968-3978.

105. Stubbs, J. M.; Siepmann, J. I.; "Elucidating the Vibrational Spectra of Hydrogen-Bonded Aggregates in Solution: Electronic Structure Calculations with Implicit Solvent and First-Principles Molecular Dynamics Simulations with Explicit Solvent for 1-Hexanol in *n*-Hexane" *J. Am. Chem. Soc.* **2005**, 127, 4722-4729.

106. Chen, B.; Potoff, J. J.; Siepmann, J. I.; "Monte Carlo calculations for alcohols and their mixtures with alkanes. Transferable potentials for phase equilibria. 5. United-atom description of primary, secondary and tertiary alcohols" *J. Phys. Chem. B* **2001**, 105, 3093-3104.

107. Wertz, D. L.; Kruh, R. K.; "Reinvestigation of Structures of Ethanol and Methanol at Room Temperature" *J. Chem. Phys.* **1967**, 47, 388.

108. Mikusinska-Planner, A.; "X-ray diffraction study of the structure of 1-propanol at -25^0C" *Acta Crystallogr. A* **1977**, 33, 433-437.

109. Swendsen R. H.; Wang, J. -S.; "Replica Monte-Carlo Simulation of Spin-Glasses" *Phys. Rev. Lett.* **1986**, 57, 2607-2609.

110. Hansmann, U. H. E.; "Parallel tempering algorithm for conformational studies of biological molecules" *Chem. Phys. Lett.* **1997**, 281, 140-150.

111. Calvo, F.; Neirotti, J. P.; Freeman, D. L.; Doll, J. D.; "Phase changes in 38-atom Lennard-Jones clusters. II. A parallel tempering study of equilibrium and dynamic properties in the molecular dynamics and microcanonical ensembles" *J. Chem. Phys.* **2000**, 112, 10350-10357.

112. Earl, D. J.; Deem, M. W.; "Parallel tempering: Theory, applications, and new perspectives" *Phys. Chem. Chem. Phys.* **2005**, 7, 3910-3916.

113. Martin, M. G.; Siepmann, J. I.; "Novel Configurational-Bias Monte Carlo Method for Branched Molecules. Transferable Potentials for Phase Equilibria. 2. United-Atom Description of Branched Alkanes" *J. Phys. Chem. B* **1999**, 103, 4508-4517.

114. Martin, M. G.; Siepmann, J. I.; Schure, M. R.; "Simulating Retention in Gas−Liquid Chromatography" *J. Phys. Chem. B* **1999**, 103, 11191-11195.

115. Seok, C.; Oxtoby, D. W.; "Nucleation in *n*-alkanes: A density-functional approach" *J. Chem. Phys.* **1998**, 109, 7982-7990.

116. Viisanen, Y.; Wagner, P. E.; Strey, R.; "Measurement of the molecular content of binary nuclei. IV. Use of the nucleation rate surfaces for the *n*-nonane-*n*-alcohol series" *J. Chem. Phys.* **1998**, 108, 4257-4266.

117. Wagner, P. E.; Strey, R.; "Two-Pathway Homogeneous Nucleation in Supersaturated Water-*n*-Nonane Vapor Mixtures" *J. Phys. Chem. B* **2001**, 105, 11656-11661.

118. Chen, B.; Siepmann, J. I.; "Microscopic structure and solvation in dry and wet octanol" *J. Phys. Chem. B* **2006**, 110, 3555-3563.

119. Wyslouzil, B. E.; Wilemski, G.; Strey, R.; Heath, C. H.; Dieregsweiler, U.; "Experimental evidence for internal structure in aqueous-organic nanodroplets" *Phys. Chem. Chem. Phys.* **2006**, 8, 54-57.

120. Li, J. -S.; Wilemski, G.; "A structural phase diagram for model aqueous organic nanodroplets" *Phys. Chem. Chem. Phys.* **2006**, 8, 1266-1270.

121. Ellison, G. B.; Tuck, A. F.; Vaida, V.; "Atmospheric processing of organic aerosols" *J. Geophys. Res. [Atmos.]* **1999**, 104, 11633-11641.

122. Dobson, C. M.; Ellison, G. B.; Tuck, A. F.; Vaida, V.; "Atmospheric aerosols as prebiotic chemical reactors" *Proc. Natl. Acad. Sci. U. S. A.* **2000**, 97, 11864-11868.

123. Donaldson, D. J.; Tuck, A. F.; Vaida, V.; "The Asymmetry of Organic Aerosol Fission and Prebiotic Chemistry" *Origins of Life and Evolution of Biospheres* **2002**, 32, 237-245.

124. Jorgensen, W. L., Chandrasekhar, J.; Madura, J. D.; Impey, R. W.; Klein, M. L.; "Comparison of simple potential functions for simulating liquid water" *J. Chem. Phys.*, **1983**, 79, 926-935.

125. Gaman, A. I.; Napari, I.; Winkler, P. M.; Vehkamaki, H.; Wagner, P. E.; Strey, R.; Viisanen, Y.; Kulmala, M.; "Homogeneous nucleation of *n*-nonane and *n*-propanol mixtures: A comparison of classical nucleation theory and experiments" *J. Chem. Phys.* **2005**, 123, 244502-(1-12).

126. Zahoransky, R. A.; Peters, F.; "Binary nucleation at low temperatures" *J. Chem. Phys.* **1985**, 83, 6425-6431.

127. Schmitt, J. L.; Whitten, J.; Adams, G. W.; Zalabsky, R. A.; "Binary nucleation of ethanol and water" *J. Chem. Phys.* **1990**, 92, 3693-3697.

128. Strey, R.; Viisanen, Y.; Wagner, P. E.; "Measurement of the molecular content of binary nuclei. III. Use of the nucleation rate surfaces for the water-*n*-alcohol series" *J. Chem. Phys.* **1995**, 103, 4333-4345.

129. Peeters, P.; Hruby´, J.; van Dongen, M. E. H.; "High Pressure Nucleation Experiments in Binary and Ternary Mixtures" *J. Phys. Chem. B* **2001**, 105, 11763-11771.

130. Chen, B.; Siepmann, J. I.; Klein, M. L.; "Vapor-liquid interfacial properties of mutually saturated water/1-butanol solutions" *J. Am. Chem. Soc.* **2002**, 124, 12232-12237.

131. Facchini, M. C.; Mircea, M.; Fuzzi, S.; Charlson, R. J.; "Cloud albedo enhancement by surface-active organic solutes in growing droplets" *Nature* **1999**, 401, 257-259.

132. Charlson, R. J.; Seinfeld, J. H.; Nenes, A.; Kulmala, M.; Laaksonen, A.; Facchini, M. C.; "Perspectives: Atmospheric science: Reshaping the theory of cloud formation" *Science* **2001**, 292, 2025-2026.

133. Tarek, M.; Klein, M. L.; "Molecular Dynamics Study of Two-Component Systems: The Shape and Surface Structure of Water/Ethanol Droplets" *J. Phys. Chem. A* **1997**, 101, 8639-8642.

134. Shah, P. S.; Hanrath, T.; Johnston, K. P.; Korgel, B. A.; "Nanocrystal and Nanowire Synthesis and Dispersibility in Supercritical Fluids" *J. Phys. Chem. B* **2004**, 108, 9574-9587.

135. Holt, J. W.; Safaeinili, A.; Plaut, J. J.; Head, J. W.; Phillips, R. J.; Seu, R.; Kempf, S. D.; Choudhary, P.; Young, D. A.; Putzig, N. E.; Biccari, D.; Gim, Y.; "Radar Sounding Evidence for Buried Glaciers in the Southern Mid-Latitudes of Mars" *Science* **2008**, 322, 1235-1238.

136. Paige, D. A.; "Ancient Mars: Wet in many Places" *Science* **2005**, 307, 1575.

137. Bibring, J. –P.; Langevin, Y.; Gendrin, A.; Gondet, B.; Poulet, F.; Berthe, M.; Soufflot, A.; Arvidson, R.; Mangold, N.; Mustard, J.; Drossart, P.; the OMEGA team; "Mars Surface Diversity as Revealed by the OMEGA/Mars Express Observations" *Science* **2005**, 307, 1576-1581.

138. Langevin,Y.; Poulet, F.; Bibring, J. –P.; Schmitt, B.; Doute, S.; Gondet, B.; "Summer Evolution of the North Polar Cap of Mars as Observed by OMEGA/Mars Express" *Science* **2005**, 307, 1581-1584.

139. Paige. D.A.; Herkenhoff, K. E.; Murray, B. C.; "Mariner 9 Observations of the South Polar Cap of Mars: Evidence for Residual CO2 Frost" *J. Geophys. Res.* **1990**, 95, 1319-1335.

140. Forget, F.; Pierrehumbert, R. T.; "Warming Early Mars with Carbon Dioxide Clouds That Scatter Infrared Radiation" *Science* **1997**, 278, 1273-1275.

141. Forget, F.; Haberle, R. M.; Montmessin, F.; Levrard B.; head, J. W.; "Formation of Glaciers on Mars by Atmospheric Precipitation at High Obliquity" *Science* **2006**, 311, 368-371.

Appendix A: Permission Request / Correspondence to the American Chemical Society

from	Ricky Nellas <rnella1@tigers.lsu.edu>
to	copyright@acs.org
date	Fri, Jul 10, 2009 at 2:55 PM hide details 7/10/09
subject	request for permission
mailed-by	tigers.lsu.edu

Dear Sir/Madam;

Good day!

I am Ricky B Nellas, a graduate student in the Chemistry Department of LSU. Since I will be using articles published by ACS, I would like to request permission to include the following articles in my dissertation.

Nellas, R. B.; McKenzie, M. E.; Chen, B.; "Probing the Nucleation Mechanism for the Binary *n*-Nonane/1-Alcohol Series with Atomistic Simulations" *J. Phys. Chem. B* **2006**, 110, 18619-18628.

Nellas, R.B.; Keasler, S.J.; Chen, B.; "Molecular content and structure of aqueous organic nanodroplets from the vapor-liquid nucleation study of the water/n-nonane/1-alcohol series" *J. Phys. Chem. A* **2008**, 112, 2930-2939.

Hope you could also send me the signed copy of the permission letter.

Thank you and have a wonderful day.

Ricky Nellas

from Karen Buehler <K_Buehler@acs.org>

to Ricky Nellas <rnella1@tigers.lsu.edu>

date Fri, Jul 10, 2009 at 2:55 PM hide details 7/10/09

subject Out of Office AutoReply: request for permission

mailed-by acs.org

ANNOUNCEMENT - CHANGES TO PERMISSION PROCEDURE
Effective immediately, requests to use material from ACS journals are being handled through the Rightslink online permission system. You must now process requests yourself through Rightslink by following the instructions can be found at http://pubs.acs.org/page/copyright/rightslink.html. Please note the Rightslink system is NOT copyright.com.

Requests for material from C&EN or ACS series books are still handled by the ACS Copyright Office directly. Be sure your request includes your name, complete address, phone and 24-hour fax numbers and a specific deadline date. See <http://pubs.acs.org/page/copyright/permissions.html> for information.

Thank you for your cooperation.

from Arleen Courtney <A_Courtney@acs.org>

to	Ricky Nellas <rnella1@tigers.lsu.edu>	
date	Fri, Jul 10, 2009 at 2:55 PM	hide details 7/10/09
subject	Out of Office AutoReply: request for permission	
mailed-by	acs.org	

ANNOUNCEMENT - CHANGES TO PERMISSION PRECEDURE
Effective immediately, requests to use material from ACS JOURNALS are being handled through the Rightslink online permission system. You must now process requests yourself through Rightslink by following the instructions that can be found at <http://pubs.acs.org/page/copyright/rightslink.html>. Requesters cannot order single copies of ACS journal articles via Rightlink and our office does not provide single copies of articles. On the LEFT side of the ACS article is wording regarding single copies that you can click on. If you do not see that wording, ask your librarian to order a copy of the article via Interlibrary Loan. If you want to make your own multiple photocopies of an article, contact us at <copyright@acs.org> and let us know how many photocopies you want to make and to whom they will be distributed. Please note the Rightslink System is NOT copyright.com.

Requests for material from C&EN or ACS series books are still handled by the ACS Copyright Office directly. Be sure your request includes your name, complete address, phone and 24-hour fax number and a specific deadline date. See <http://pubs.acs.org/page/copyright/permissions.html> for information.

Thank you for your cooperation.

from donotreply@copyright.com

to rnella1@lsu.edu

hide details 7/10/09

date Fri, Jul 10, 2009 at 3:11 PM

subject Thank you for your Rightslink / American Chemical Society order

Thank you for placing your order through Copyright Clearance Center's Rightslink service. American Chemical Society has partnered with Rightslink to license its content online. Note: Payee for this order is Copyright Clearance Center.

Your order details and publisher terms and conditions (including any credit line requirements) are available by clicking the link below:

http://s100.copyright.com/CustomerAdmin/PLF.jsp?lID=2009070_1247260318592

Order Details
Licensee: Ricky B Nellas
License Date: Jul 10, 2009
License Number: 2225550358592
Publication: The Journal of Physical Chemistry A
Title: Molecular Content and Structure of Aqueous Organic Nanodroplets from the Vapor?Liquid Nucleation Study of the Water/n-Nonane/1-Alcohol Series
Type Of Use: Thesis/Dissertation
Total: 0.00 USD

To access your account, please visit https://myaccount.copyright.com. Please note: Credit cards payments are charged immediately after order confirmation. Invoice payments are billed twice monthly.
Please take a moment to complete our customer satisfaction survey.
http://www.surveymonkey.com/s.asp?u=500021004336
If you have any comments or questions, please contact Rightslink:
Copyright Clearance Center
Rightslink
Tel (toll free): +1-877-622-5543
Tel: +1-978-646-2777
E-mail: mailto:customercare@copyright.com
Web: http://www.copyright.com
B.1:v4.2

from donotreply@copyright.com

to rnella1@lsu.edu

hide details 7/10/09

date Fri, Jul 10, 2009 at 3:16 PM

subject Thank you for your Rightslink / American Chemical Society order

Thank you for placing your order through Copyright Clearance Center's Rightslink service. American Chemical Society has partnered with Rightslink to license its content online. Note: Payee for this order is Copyright Clearance Center.

Your order details and publisher terms and conditions (including any credit line requirements) are available by clicking the link below:

http://s100.copyright.com/CustomerAdmin/PLF.jsp?lID=2009070_1247260580012

Order Details
Licensee: Ricky B Nellas
License Date: Jul 10, 2009

License Number: 2225550620012
Publication: The Journal of Physical Chemistry B
Title: Probing the Nucleation Mechanism for the Binary n-Nonane/1-Alcohol Series with Atomistic Simulations

Type Of Use: Thesis/Dissertation
Total: 0.00 USD

To access your account, please visit https://myaccount.copyright.com. Please note: Credit cards payments are charged immediately after order confirmation. Invoice payments are billed twice monthly.
Please take a moment to complete our customer satisfaction survey.
http://www.surveymonkey.com/s.asp?u=500021004336
If you have any comments or questions, please contact Rightslink:
Copyright Clearance Center
Rightslink
Tel (toll free): +1-877-622-5543
Tel: +1-978-646-2777
E-mail: mailto:customercare@copyright.comWeb: http://www.copyright.com
B.1:v4.2

Appendix B: License Agreement from the Journal of Physical Chemistry A

AMERICAN CHEMICAL SOCIETY LICENSE TERMS AND CONDITIONS

Oct 20, 2009

This is a License Agreement between Ricky B Nellas ("You") and American Chemical Society ("American Chemical Society") provided by Copyright Clearance Center ("CCC"). The license consists of your order details, the terms and conditions provided by American Chemical Society, and the payment terms and conditions.

All payments must be made in full to CCC. For payment instructions, please see information listed at the bottom of this form.

License Number	2225550358592
License Date	Jul 10, 2009
Licensed content publisher	American Chemical Society
Licensed content publication	The Journal of Physical Chemistry A
Licensed content title	Molecular Content and Structure of Aqueous Organic Nanodroplets from the Vapor-Liquid Nucleation Study of the Water/n-Nonane/1-Alcohol Series
Licensed content author	Ricky B. Nellas et al.
Licensed content date	Apr 1, 2008
Volume number	112
Issue number	13
Type of Use	Thesis/Dissertation
Requestor type	Not specified
Format	Print
Portion	Full article
Author of this ACS article	Yes
Order reference number	
Title of the thesis / dissertation	Multicomponent Nucleation: From Mechanisms to Applications
Expected completion date	Dec 2009
Estimated size(pages)	150
Billing Type	Invoice
Billing Address	3650 Nicholson Drive Apt 1162 Baton Rouge, LA 70802 United States
Customer reference info	
Total	0.00 USD

Thesis/Dissertation

ACS / RIGHTSLINK TERMS & CONDITIONS
THESIS/DISSERTATION

INTRODUCTION
The publisher for this copyrighted material is the American Chemical Society. By clicking "accept" in connection with completing this licensing transaction, you agree that the following terms and conditions apply to this transaction (along with the Billing and Payment terms and conditions established by Copyright Clearance Center, Inc. ("CCC"), at the time that you opened your Rightslink account and that are available at any time at <http://myaccount.copyright.com>).

LIMITED LICENSE
Publisher hereby grants to you a non-exclusive license to use this material. Licenses are for one-time use only with a maximum distribution equal to the number that you identified in the licensing process; any form of republication must be completed within 60 days from the date hereof (although copies prepared before then may be distributed thereafter).

GEOGRAPHIC RIGHTS: SCOPE
Licenses may be exercised anywhere in the world.

RESERVATION OF RIGHTS
Publisher reserves all rights not specifically granted in the combination of (i) the license details provided by you and accepted in the course of this licensing transaction, (ii) these terms and conditions and (iii) CCC's Billing and Payment terms and conditions.

PORTION RIGHTS STATEMENT: DISCLAIMER
If you seek to reuse a portion from an ACS publication, it is your responsibility to examine each portion as published to determine whether a credit to, or copyright notice of, a third party owner was published adjacent to the item. You may only obtain permission via Rightslink to use material owned by ACS. Permission to use any material published in an ACS publication, journal, or article which is reprinted with permission of a third party must be obtained from the third party owner. ACS disclaims any responsibility for any use you make of items owned by third parties without their permission.

REVOCATION
The American Chemical Society reserves the right to revoke a license for any reason, including but not limited to advertising and promotional uses of ACS content, third party usage, and incorrect figure source attribution.

LICENSE CONTINGENT ON PAYMENT
While you may exercise the rights licensed immediately upon issuance of the license at the end of the licensing process for the transaction, provided that you have disclosed complete and accurate details of your proposed use, no license is finally effective unless and until full payment is received from you (by CCC) as provided in CCC's Billing and Payment terms and conditions. If full payment is not received on a timely basis, then any license preliminarily granted shall be deemed automatically revoked and shall be void as if never granted. Further, in the event that you breach any of these terms and conditions or any of CCC's Billing and Payment terms and conditions, the license is automatically revoked and shall be void as if never granted. Use of materials as described in a revoked license, as well as any use of the

materials beyond the scope of an unrevoked license, may constitute copyright infringement and publisher reserves the right to take any and all action to protect its copyright in the materials.

COPYRIGHT NOTICE: DISCLAIMER
You must include the following copyright and permission notice in connection with any reproduction of the licensed material: "Reprinted ("Adapted" or "in part") with permission from REFERENCE CITATION. Copyright YEAR American Chemical Society."

WARRANTIES: NONE
Publisher makes no representations or warranties with respect to the licensed material.

INDEMNITY
You hereby indemnify and agree to hold harmless publisher and CCC, and their respective officers, directors, employees and agents, from and against any and all claims arising out of your use of the licensed material other than as specifically authorized pursuant to this license.

NO TRANSFER OF LICENSE
This license is personal to you or your publisher and may not be sublicensed, assigned, or transferred by you to any other person without publisher's written permission.

NO AMENDMENT EXCEPT IN WRITING
This license may not be amended except in a writing signed by both parties (or, in the case of publisher, by CCC on publisher's behalf).

OBJECTION TO CONTRARY TERMS
Publisher hereby objects to any terms contained in any purchase order, acknowledgment, check endorsement or other writing prepared by you, which terms are inconsistent with these terms and conditions or CCC's Billing and Payment terms and conditions. These terms and conditions, together with CCC's Billing and Payment terms and conditions (which are incorporated herein), comprise the entire agreement between you and publisher (and CCC) concerning this licensing transaction. In the event of any conflict between your obligations established by these terms and conditions and those established by CCC's Billing and Payment terms and conditions, these terms and conditions shall control.

JURISDICTION
This license transaction shall be governed by and construed in accordance with the laws of the District of Columbia. You hereby agree to submit to the jurisdiction of the courts located in the District of Columbia for purposes of resolving any disputes that may arise in connection with this licensing transaction.

THESES/DISSERTATION TERMS
Publishing implications of electronic publication of theses and dissertation material
Students and their mentors should be aware that posting of theses and dissertation material on the Web prior to submission of material from that thesis or dissertation to an ACS journal may affect publication in that journal. Whether Web posting is considered prior publication may be evaluated on a case-by-case basis by the journal's editor. If an ACS journal editor considers Web posting to be "prior publication", the paper will not be accepted for publication in that journal. If you intend to submit your unpublished paper to ACS for publication, check with the appropriate editor prior to posting your manuscript electronically.

If your paper has already been published by ACS and you want to include the text or portions of the text in your thesis/dissertation in **print or microfilm formats**, please print the ACS copyright credit line on the first page of your article: "Reproduced (or 'Reproduced in part') with permission from [FULL REFERENCE CITATION.] Copyright [YEAR] American

Chemical Society." Include appropriate information.

Submission to a Dissertation Distributor: If you plan to submit your thesis to UMI or to another dissertation distributor, you should not include the unpublished ACS paper in your thesis if the thesis will be disseminated electronically, until ACS has published your paper. After publication of the paper by ACS, you may release the entire thesis (**not the individual ACS article by itself**) for electronic dissemination through the distributor; ACS's copyright credit line should be printed on the first page of the ACS paper.

Use on an Intranet: The inclusion of your ACS unpublished or published manuscript is permitted in your thesis in print and microfilm formats. If ACS has published your paper you may include the manuscript in your thesis on an intranet that is not publicly available. Your ACS article cannot be posted electronically on a publicly available medium (i.e. one that is not password protected), such as but not limited to, electronic archives, Internet, library server, etc. The only material from your paper that can be posted on a public electronic medium is the article abstract, figures, and tables, and you may link to the article's DOI or post the article's author-directed URL link provided by ACS. This paragraph does not pertain to the dissertation distributor paragraph above.

Other conditions:

v1.1

Gratis licenses (referencing $0 in the Total field) are free. Please retain this printable license for your reference. No payment is required.

If you would like to pay for this license now, please remit this license along with your payment made payable to "COPYRIGHT CLEARANCE CENTER" otherwise you will be invoiced within 30 days of the license date. Payment should be in the form of a check or money order referencing your account number and this license number 2225550358592. If you would prefer to pay for this license by credit card, please go to http://www.copyright.com/creditcard to download our credit card payment authorization form.

Make Payment To:
Copyright Clearance Center
Dept 001
P.O. Box 843006
Boston, MA 02284-3006

If you find copyrighted material related to this license will not be used and wish to cancel, please contact us referencing this license number 2225550358592 and noting the reason for cancellation.

Questions? customercare@copyright.com or +1-877-622-5543 (toll free in the US) or +1-978-646-2777.

Appendix C: License Agreement from the Journal of Physical Chemistry B

AMERICAN CHEMICAL SOCIETY LICENSE TERMS AND CONDITIONS

Oct 20, 2009

This is a License Agreement between Ricky B Nellas ("You") and American Chemical Society ("American Chemical Society") provided by Copyright Clearance Center ("CCC"). The license consists of your order details, the terms and conditions provided by American Chemical Society, and the payment terms and conditions.

All payments must be made in full to CCC. For payment instructions, please see information listed at the bottom of this form.

License Number	2225550620012
License Date	Jul 10, 2009
Licensed content publisher	American Chemical Society
Licensed content publication	The Journal of Physical Chemistry B
Licensed content title	Probing the Nucleation Mechanism for the Binary n-Nonane/1-Alcohol Series with Atomistic Simulations
Licensed content author	Ricky B. Nellas et al.
Licensed content date	Sep 1, 2006
Volume number	110
Issue number	37
Type of Use	Thesis/Dissertation
Requestor type	Not specified
Format	Print
Portion	Full article
Author of this ACS article	Yes
Order reference number	
Title of the thesis / dissertation	Multicomponent Nucleation: From Mechanisms to Applications
Expected completion date	Dec 2009
Estimated size(pages)	150
Billing Type	Invoice
Billing Address	3650 Nicholson Drive Apt 1162 Baton Rouge, LA 70802 United States
Customer reference info	
Total	0.00 USD

Thesis/Dissertation

ACS / RIGHTSLINK TERMS & CONDITIONS
THESIS/DISSERTATION

INTRODUCTION
The publisher for this copyrighted material is the American Chemical Society. By clicking "accept" in connection with completing this licensing transaction, you agree that the following terms and conditions apply to this transaction (along with the Billing and Payment terms and conditions established by Copyright Clearance Center, Inc. ("CCC"), at the time that you opened your Rightslink account and that are available at any time at <http://myaccount.copyright.com>).

LIMITED LICENSE
Publisher hereby grants to you a non-exclusive license to use this material. Licenses are for one-time use only with a maximum distribution equal to the number that you identified in the licensing process; any form of republication must be completed within 60 days from the date hereof (although copies prepared before then may be distributed thereafter).

GEOGRAPHIC RIGHTS: SCOPE
Licenses may be exercised anywhere in the world.

RESERVATION OF RIGHTS
Publisher reserves all rights not specifically granted in the combination of (i) the license details provided by you and accepted in the course of this licensing transaction, (ii) these terms and conditions and (iii) CCC's Billing and Payment terms and conditions.

PORTION RIGHTS STATEMENT: DISCLAIMER
If you seek to reuse a portion from an ACS publication, it is your responsibility to examine each portion as published to determine whether a credit to, or copyright notice of, a third party owner was published adjacent to the item. You may only obtain permission via Rightslink to use material owned by ACS. Permission to use any material published in an ACS publication, journal, or article which is reprinted with permission of a third party must be obtained from the third party owner. ACS disclaims any responsibility for any use you make of items owned by third parties without their permission.

REVOCATION
The American Chemical Society reserves the right to revoke a license for any reason, including but not limited to advertising and promotional uses of ACS content, third party usage, and incorrect figure source attribution.

LICENSE CONTINGENT ON PAYMENT
While you may exercise the rights licensed immediately upon issuance of the license at the end of the licensing process for the transaction, provided that you have disclosed complete and accurate details of your proposed use, no license is finally effective unless and until full payment is received from you (by CCC) as provided in CCC's Billing and Payment terms and conditions. If full payment is not received on a timely basis, then any license preliminarily granted shall be deemed automatically revoked and shall be void as if never granted. Further, in the event that you breach any of these terms and conditions or any of CCC's Billing and Payment terms and conditions, the license is automatically revoked and shall be void as if never granted. Use of materials as described in a revoked license, as well as any use of the

materials beyond the scope of an unrevoked license, may constitute copyright infringement and publisher reserves the right to take any and all action to protect its copyright in the materials.

COPYRIGHT NOTICE: DISCLAIMER
You must include the following copyright and permission notice in connection with any reproduction of the licensed material: "Reprinted ("Adapted" or "in part") with permission from REFERENCE CITATION. Copyright YEAR American Chemical Society."

WARRANTIES: NONE
Publisher makes no representations or warranties with respect to the licensed material.

INDEMNITY
You hereby indemnify and agree to hold harmless publisher and CCC, and their respective officers, directors, employees and agents, from and against any and all claims arising out of your use of the licensed material other than as specifically authorized pursuant to this license.

NO TRANSFER OF LICENSE
This license is personal to you or your publisher and may not be sublicensed, assigned, or transferred by you to any other person without publisher's written permission.

NO AMENDMENT EXCEPT IN WRITING
This license may not be amended except in a writing signed by both parties (or, in the case of publisher, by CCC on publisher's behalf).

OBJECTION TO CONTRARY TERMS
Publisher hereby objects to any terms contained in any purchase order, acknowledgment, check endorsement or other writing prepared by you, which terms are inconsistent with these terms and conditions or CCC's Billing and Payment terms and conditions. These terms and conditions, together with CCC's Billing and Payment terms and conditions (which are incorporated herein), comprise the entire agreement between you and publisher (and CCC) concerning this licensing transaction. In the event of any conflict between your obligations established by these terms and conditions and those established by CCC's Billing and Payment terms and conditions, these terms and conditions shall control.

JURISDICTION
This license transaction shall be governed by and construed in accordance with the laws of the District of Columbia. You hereby agree to submit to the jurisdiction of the courts located in the District of Columbia for purposes of resolving any disputes that may arise in connection with this licensing transaction.

THESES/DISSERTATION TERMS
Publishing implications of electronic publication of theses and dissertation material
Students and their mentors should be aware that posting of theses and dissertation material on the Web prior to submission of material from that thesis or dissertation to an ACS journal may affect publication in that journal. Whether Web posting is considered prior publication may be evaluated on a case-by-case basis by the journal's editor. If an ACS journal editor considers Web posting to be "prior publication", the paper will not be accepted for publication in that journal. If you intend to submit your unpublished paper to ACS for publication, check with the appropriate editor prior to posting your manuscript electronically.

If your paper has already been published by ACS and you want to include the text or portions of the text in your thesis/dissertation in **print or microfilm formats**, please print the ACS copyright credit line on the first page of your article: "Reproduced (or 'Reproduced in part') with permission from [FULL REFERENCE CITATION.] Copyright [YEAR] American

Chemical Society." Include appropriate information.

Submission to a Dissertation Distributor: If you plan to submit your thesis to UMI or to another dissertation distributor, you should not include the unpublished ACS paper in your thesis if the thesis will be disseminated electronically, until ACS has published your paper. After publication of the paper by ACS, you may release the entire thesis (**not the individual ACS article by itself**) for electronic dissemination through the distributor; ACS's copyright credit line should be printed on the first page of the ACS paper.

Use on an Intranet: The inclusion of your ACS unpublished or published manuscript is permitted in your thesis in print and microfilm formats. If ACS has published your paper you may include the manuscript in your thesis on an intranet that is not publicly available. Your ACS article cannot be posted electronically on a publicly available medium (i.e. one that is not password protected), such as but not limited to, electronic archives, Internet, library server, etc. The only material from your paper that can be posted on a public electronic medium is the article abstract, figures, and tables, and you may link to the article's DOI or post the article's author-directed URL link provided by ACS. This paragraph does not pertain to the dissertation distributor paragraph above.

Other conditions:

v1.1

Gratis licenses (referencing $0 in the Total field) are free. Please retain this printable license for your reference. No payment is required.

If you would like to pay for this license now, please remit this license along with your payment made payable to "COPYRIGHT CLEARANCE CENTER" otherwise you will be invoiced within 30 days of the license date. Payment should be in the form of a check or money order referencing your account number and this license number 2225550620012. If you would prefer to pay for this license by credit card, please go to http://www.copyright.com/creditcard to download our credit card payment authorization form.

Make Payment To:
Copyright Clearance Center
Dept 001
P.O. Box 843006
Boston, MA 02284-3006

If you find copyrighted material related to this license will not be used and wish to cancel, please contact us referencing this license number 2225550620012 and noting the reason for cancellation.

Questions? customercare@copyright.com or +1-877-622-5543 (toll free in the US) or +1-978-646-2777.

Appendix D: Permission Request / Correspondence to the Royal Society of Chemistry

-----Original Message-----
From: rnella1@tigers.lsu.edu [mailto:rnella1@tigers.lsu.edu]
Sent: 10 July 2009 20:19
To: CONTRACTS-COPYRIGHT (shared)
Subject: Permission Request Form: Ricky B Nellas

Name : Ricky B Nellas

Address :

3650 Nicholson Drive Apt 1162
Baton Rouge, LA
70802 USA

Tel : 2252358429
Fax :
Email : rnella1@tigers.lsu.edu

I am preparing the following work for publication:

Article/Chapter Title : Dissertation: Multicomponent Nucleation: From Mechanisms to Applications

Journal/Book Title :

Editor/Author(s) : Ricky B Nellas and Bin Chen

Publisher : Louisiana State University

I would very much appreciate your permission to use the following material:

Journal/Book Title : PCCP

Editor/Author(s) : Nellas, R.B.; Chen, B.; Siepmann, J.I

Volume Number : 9

Year of Publication : 2007

Description of Material : communication (ternary nucleation)

Page(s) : 2779-2781

Journal/Book Title : PCCP

Editor/Author(s) : Nellas, R.B.; Chen, B

Volume Number : 10

Year of Publication : 2008

Description of Material : paper (multicomponent nucleation mechanism)

Page(s) : 506-514

Any Additional Comments :

I will be using the materials for my PhD dissertation. Thanks a lot.

from CONTRACTS-COPYRIGHT (shared) <Contracts-Copyright@rsc.org>

to	"rnella1@tigers.lsu.edu" <rnella1@tigers.lsu.edu>	hide details
date	Mon, Jul 13, 2009 at 2:14 AM	7/13/09
subject	RE: Permission Request Form: Ricky B Nellas	

Dear Mr Nellas

The Royal Society of Chemistry (RSC) hereby grants permission for the use of your paper(s) specified below in the printed and microfilm version of your thesis. You may also make available the PDF version of your paper(s) that the RSC sent to the corresponding author(s) of your paper(s) upon publication of the paper(s) in the following ways: in your thesis via any website that your university may have for the deposition of theses, via your university's Intranet or via your own personal website. We are however unable to grant you permission to include the PDF version of the paper(s) on its own in your institutional repository. The Royal Society of Chemistry is a signatory to the STM Guidelines on Permissions (available on request).

Please note that if the material specified below or any part of it appears with credit or acknowledgement to a third party then you must also secure permission from that third party before reproducing that material.

Please ensure that the thesis states the following:

Reproduced by permission of the PCCP Owner Societies

and include a link to the article on the Royal Society of Chemistry's website.

Please ensure that your co-authors are aware that you are including the paper in your thesis.

Regards

Gill Cockhead
Contracts & Copyright Executive

Gill Cockhead (Mrs), Contracts & Copyright Executive
Royal Society of Chemistry, Thomas Graham House
Science Park, Milton Road, Cambridge CB4 0WF, UK
Tel +44 (0) 1223 432134, Fax +44 (0) 1223 423623
http://www.rsc.org

from	Ricky Nellas <rnella1@tigers.lsu.edu>	
to	"CONTRACTS-COPYRIGHT (shared)" <Contracts-Copyright@rsc.org>	
date	Mon, Jul 13, 2009 at 11:46 AM	hide details 7/13/09
subject	Re: Permission Request Form: Ricky B Nellas	
mailed-by	tigers.lsu.edu	

Dear Mrs Gill Cockhead,

Good day!

Thanks for the immediate reply. Can I possibly get a signed permission letter from your office? I think our university requires that a signed permission letter be attached in the Appendix portion of the dissertation.

I am hoping for a favorable response.

Thanks a lot and have a great week.

Ricky Nellas

CONTRACTS-COPYRIGHT (shared) show details 7/14/09
to me

from CONTRACTS-COPYRIGHT (shared) <Contracts-Copyright@rsc.org>
to Ricky Nellas <rnella1@tigers.lsu.edu>
date Tue, Jul 14, 2009 at 2:53 AM
subject RE: Permission Request Form: Ricky B Nellas

hide details 7/14/09

Dear Mr Nellas

Please find attached a signed letter granting you permission to include the papers in your thesis.

Best wishes

Gill

Gill Cockhead (Mrs), Contracts & Copyright Executive
Royal Society of Chemistry, Thomas Graham House
Science Park, Milton Road, Cambridge CB4 0WF, UK
Tel +44 (0) 1223 432134, Fax +44 (0) 1223 423623
http://www.rsc.org

Appendix E: Permission Letter from the Royal Society of Chemistry

RSC | Advancing the Chemical Sciences

Royal Society of Chemistry
Thomas Graham House
Science Park
Milton Road
Cambridge
CB4 0WF

Tel: +44 (0)1223 420 066
Direct: +44 (0) 1223 432134
Fax: +44 (0)1223 423 623
Email: contracts-copyright@rsc.org

www.rsc.org

CONTRACTS & COPYRIGHT

Ricky B Nellas
3650 Nicholson Drive Apt 1162
Baton Rouge, LA 70802
USA

14 July 2009

Dear Mr Nellas

Permission Request from the Royal Society of Chemistry

The Royal Society of Chemistry (RSC) hereby grants permission for the use of your paper(s) specified below in the printed and microfilm version of your thesis. You may also make available the PDF version of your paper(s) that the RSC sent to the corresponding author(s) of your paper(s) upon publication of the paper(s) in the following ways: in your thesis via any website that your university may have for the deposition of theses, via your university's Intranet or via your own personal website. We are however unable to grant you permission to include the PDF version of the paper(s) on its own in your institutional repository. The Royal Society of Chemistry is a signatory to the STM Guidelines on Permissions (available on request).

The papers are:

- Ricky B. Nellas, Bin Chen, J. Ilja Siepmann, *Phys. Chem. Chem. Phys.*, 2007, (22), 2779-2781, DOI: 10.1039/b705385a
- Ricky B. Nellas, Bin Chen, *Phys. Chem. Chem. Phys.*, 2008, (4), 506-514, DOI: 10.1039/b713189e

Please note that if the material specified below or any part of it appears with credit or acknowledgement to a third party then you must also secure permission from that third party before reproducing that material.

Please ensure that the thesis states the following:

Reproduced by permission of the PCCP Owner Societies

and include a link to the article on the Royal Society of Chemistry's website.

Please ensure that your co-authors are aware that you are including the paper in your thesis.

Yours sincerely

Gill Cockhead
Contracts & Copyright Executive

Vita

The youngest child of Modesto Gutib Nellas and Iluminada Bendanillo Nellas, Ricky Bendanillo Nellas was born in March 1978, in Dumaguete City, Philippines. In the fall of 1995, he went to the University of the Philippines – Los Baños as an Agricultural and Rural Development Scholar and in the spring of 1999, he received a Bachelor of Science degree in chemistry. He moved back to Dumaguete City and served as a science and math mentor at Holy Cross High School for three years. On the fall of 2002, right after his mother's death, he went to Manila, Philippines, and took the Chemistry Licensure Examination. Right after passing the board exam, he taught at the Institute of Chemistry, University of the Philippines – Los Baños, for almost two years prior to his graduate studies at Louisiana State University – Baton Rouge, in the United States of America. He started his graduate program in chemistry in the fall of 2004 and will be receiving his doctoral degree in chemistry in the spring of 2010.